

**Measurement of the Elastic ρ^0 -meson
Photoproduction Cross Section
using the Forward Proton Spectrometer
at the H1 Detector at HERA**

DISSERTATION

zur Erlangung des akademischen Grades
doctor rerum naturalium
(Dr. rer. nat.)

im Fach Physik

eingereicht an der

Mathematisch-Naturwissenschaftlichen Fakultät I
der Humboldt-Universität zu Berlin

von

Anatoli Raffievich Astvatsatourov

geboren am 16. Jan 1970 in Yerevan, UdSSR

Präsident der Humboldt-Universität zu Berlin
Prof. Dr. J. Mlynek

Dekan der Mathematisch-Naturwissenschaftlichen Fakultät I
Prof. Dr. B. Ronacher

Gutachter/innen:

1. Prof. Dr. H. Kolanoski
2. Prof. Dr. P. Söding
3. Prof. Dr. E.-M. Kabuss

Tag der mündlichen Prüfung:

Abstract

A measurement of the elastic ρ^0 -meson photoproduction cross section is presented. The data are collected by the H1 experiment in scattering of electrons off protons at the HERA collider in January–April 1999. In the current analysis the absolute value of the proton momentum transfer at the proton vertex $|t|$ is measured by the horizontal stations of the Forward Proton Spectrometer (FPS) which have started stable operation in January 1999. The FPS horizontal stations cover the kinematic region of low proton momentum transfer t . The cross section of elastic ρ^0 -meson photoproduction is measured in the following kinematic region: 1) proton momentum transfer of $0.08 \leq |t| \leq 0.38 \text{ GeV}^2$, 2) γp centre of mass energy W of $20 < W < 78 \text{ GeV}$ (inelasticity y kinematic range of $0.004 < y < 0.06$), 3) ρ^0 decay pions invariant mass $M_{\pi\pi}$ interval of $0.5 < M_{\pi\pi} < 1.1 \text{ GeV}$. The logarithmical slope parameter of the differential cross section $d\sigma/dt$ is found to be: $b = 10.11 \pm 1.54 \text{ (stat.)} \pm 1.25 \text{ (syst.) GeV}^{-2}$. The observed $\gamma p \rightarrow \rho^0 p$ cross section value extrapolated to the full kinematic region, is found to be: $\sigma_{\gamma p \rightarrow \rho^0 p} = 9.88 \pm 0.93 \text{ (stat.)} \pm 1.30 \text{ (syst.) } \mu\text{b}$.

Kurzfassung

Die vorliegende Arbeit befasst sich mit der Messung des Wirkungsquerschnitts der elastischen Photoerzeugung der ρ^0 -Mesonen mit dem H1-Detektor. Die Daten wurden von Januar bis April 1999 durch das H1-Experiment beim Zerstreuen der Elektronen mit den Protonen in dem HERA-Ringbeschleuniger aufgenommen. In dieser Analyse wird der Absolutwert des Protonübergangsmomentes am Protonvertex $|t|$ in einer direkten Messung des zerstreuten Protons festgestellt. Ein weggestreutes Proton wird durch den horizontalen Teil des Vorwärtsprotonspektrometers (FPS) gemessen. Dieses Spektrometer begann im Januar 1999 mit stabilem Betrieb und umfasst die kinematische Region der kleinen Protonübergangsmomente t . Der Wirkungsquerschnitt der elastischen ρ^0 -Mesonen Photoerzeugung ist im kinematischen Bereich $0.08 < |t| < 0.38 \text{ GeV}^2$ des Protonübergangsmomentes gemessen, mit γp Schwerpunktsenergie W im Bereich $20 < W < 78 \text{ GeV}$ (der kinematische Bereich der Unelastizität y von $0.004 < y < 0.06$) und der invarianten Masse des ρ^0 -Zerfallpions $M_{\pi\pi}$: $0.5 < M_{\pi\pi} < 1.1 \text{ GeV}$. Der Steigungsparameter in logarithmischer Darstellung des differentiellen Wirkungsquerschnitts $d\sigma/dt$ ist: $b = 10.11 \pm 1.54 \text{ (stat.)} \pm 1.25 \text{ (syst.) GeV}^{-2}$. Der gemessene totale Wirkungsquerschnitt des Prozesses $\gamma p \rightarrow \rho^0 p$ ist $\sigma_{\gamma p \rightarrow \rho^0 p} = 9.88 \pm 0.93 \text{ (stat.)} \pm 1.30 \text{ (syst.) } \mu\text{b}$.

Contents

1	Introduction	4
2	Physics Aspects	7
2.1	Kinematics	8
2.2	Photon Flux	10
2.3	Vector Dominance Model	11
2.4	Regge Model	13
2.5	Elastic ρ^0 Photoproduction	17
2.6	Monte Carlo Models	19
3	H1 Experiment at HERA	21
3.1	HERA e-p Collider	21
3.2	H1 Detector	22
3.3	Tracking System	25
3.4	Calorimetry	27
3.5	The Luminosity System	30
3.6	Triggering System and Data Acquisition	32
3.6.1	The z -Vertex Trigger	33
3.6.2	The Drift Chamber r - ϕ Trigger	34
3.7	H1 Software Packages	35

4	Forward Proton Spectrometer	36
4.1	FPS in the Forward Proton Beam Line	36
4.2	Components of the Horizontal Stations	38
4.3	Detector Position Measurement	42
4.4	Proton Track Candidates	46
4.5	Momentum Reconstruction	48
4.6	Calibration	51
4.7	Proton Energy and Polar Angles	54
5	Event Selection	57
5.1	Data Sample	57
5.2	Selection Criteria	59
5.3	Background Treatment	61
5.4	Vertex Analysis	65
5.5	Luminosity	66
5.6	Photon Flux	69
6	Monte Carlo and Data Treatment	70
6.1	Quality of Monte Carlo Reconstruction	70
6.2	Comparison of Data and Monte Carlo	75
6.3	Momentum Balance	77
6.4	Measurement Efficiency	79
6.4.1	Geometrical Acceptance	79
6.4.2	Trigger Efficiency	79
6.4.3	Reconstruction Efficiency	83
6.5	Systematic Errors	86
7	Elastic ρ^0 Cross Section	88
7.1	Distribution by the Invariant Mass	89
7.1.1	Uncorrected Mass Spectrum	89
7.1.2	Differential Cross Section $d\sigma/dM_{\pi\pi}$	90
7.1.3	Cross Section $d\sigma/dM_{\pi\pi}$ in $ t $ and W Intervals	92
7.2	Proton Momentum Transfer Dependence	96
7.2.1	Uncorrected $ t $ Spectrum	96
7.2.2	Differential Cross Section $d\sigma/d t $	96
7.3	Evaluation of Statistical Errors	101
7.4	Comparison with Other Measurements	102
8	Conclusions	105

Chapter 1

Introduction

This work is devoted to the elastic ρ^0 -meson photoproduction in γp interactions, $\gamma p \rightarrow \rho^0 p$. The interest to the vector mesons photoproduction can be stipulated by the following reasons:

- 1) The total photoproduction cross section in γp interaction $\sigma_{\gamma p}$ is related to the cross section of the vector mesons scattering off protons σ_{Vp} , as it was obtained in applications of the additive quark model for hadron-hadron interactions [1, 2, 3].
- 2) The vector mesons (especially light vector mesons) production can not be described by QED or QCD and phenomenological approaches, opened for development, are applied.

The measurement was carried out with the H1 detector at HERA, the high energy ep collider at DESY. The Forward Proton Spectrometer (FPS), a magnetic spectrometer at H1 is used. The FPS is placed downstream the proton beam close to the beam pipe. Since 1997 horizontal detectors of the FPS are installed at the H1 experiment to measure very forward scattered protons in electron-proton interactions. They are located at 80 m and 64 m distance from the ep interaction point. The data presented here were collected in January–April 1999 during the first stable operation period of the FPS horizontal detectors.

Experimental Basis

In 1992 the HERA collider in DESY started data collection colliding electrons of 27.6 GeV with protons of 820 GeV. Since 1999 the HERA proton beam energy was increased from 820 to 920 GeV. The centre of mass energy (CME) of ep scattering was changed from $\sqrt{s} \simeq 301$ GeV to $\sqrt{s} \simeq 319$ GeV. Thus, the HERA collider is a source of virtual photon – proton (γp) interactions in the energy range of $W \sim 30 \div 318$ GeV in the γp CME system. By detecting the forward scattered proton the FPS horizontal detectors measure the proton momentum transfer $|t|$.

The current analysis is carried out in the kinematic range of $20 < W < 78$ GeV and $0.08 < |t| < 0.38$ GeV². In order to investigate the dependence of the measured cross

section on W and $|t|$, three W intervals, at mean values $\langle W \rangle$ of 27.9 GeV, 38.7 GeV and 56.3 GeV, and three $|t|$ intervals, at mean values $\langle |t| \rangle$ of 0.111 GeV², 0.147 GeV² and 0.232 GeV², are considered.

Physical Basis

Scattering of electrons off protons probes the proton structure by virtually exchanged particles – the photon, neutral Z^0 boson or charged W^\pm bosons. Physics at low momentum transfer from the electron to the proton is dominated by photon exchange [4]. It was early observed at HERA [5, 6, 7, 8, 9, 10] that there is a large fraction of scattering events in which the virtual photon “sees” the proton as an entire object. In such events the photon cannot probe the proton structure. In analogy to optics the interaction process when a photon probes only the vicinity of the proton was termed *diffraction process*. The term *diffraction* was introduced in high energy physics by L.D.Landau and I.Ya.Pomeranchuk. Later these events were described as virtual photon – pomeron interactions.

On the contrary, when the virtual γ “sees” the proton as a compound system and the proton structure becomes visible, the reaction is termed Deep Inelastic Scattering (DIS). The DIS processes are not considered in the present work.

The photon is a gauge particle which exhibits certain duality in electromagnetic and hadronic interactions. The dual nature of the photon can be expressed by superposition of a *bare* photon and a *hadronic* photon. The bare photon interacts via electromagnetic forces described in Quantum Electrodynamics (QED). The hadronic photon fluctuates into a $q\bar{q}$ pair (or into a hadronic state of particle and antiparticle) which then leads to hadronic interactions with the target. The process with interaction of the hadronic component of the photon is termed *resolved*. Thus, the hadronic photon behaves like a hadron. Its strong interaction can be interpreted in the Vector Dominance Model (VDM) [11]. The VDM asserts that the quasi-real photon fluctuates into a $q\bar{q}$ state (neutral vector meson) with photon quantum numbers $J^{PC} = 1^{--}$, $Q = B = S = 0$. The diffractive scattering of the $q\bar{q}$ state off the incoming proton may result into a real vector meson and the scattered proton. This interaction of the vector meson state with the proton is described in Regge theory by the Pomeron trajectory exchange.

Photoproduction in $e p$ Scattering

The electron four-momentum transfer squared and the virtual photon momentum are denoted as Q^2 and q respectively ($Q^2 = -q^2$ by definition). In this analysis the scattered electron is lost in most events and the Q^2 is determined in the frame of the outgoing hadrons.

The photoproduction is a process with a very small Q^2 in which the electron is scattered nearly collinear to the electron beam direction. The rate of photoproduction

processes is large because of the amplitude divergence of quasi-real photon emittance from $e \rightarrow e\gamma$. Thus, the HERA ep collider is a rich source of γp interactions where quasi-real photon exchange dynamics and the properties of the photon may be investigated with high precision.

Due to the very low photon virtuality, Q^2 , the scattered electron travels in the beam pipe. It can be tagged by detectors surrounding the electron beam pipe in a limited acceptance range. Most of the photoproduction in the H1 detector is *untagged*, i.e. the scattered electron is not detected but a significant statistics is accumulated.

The present work concentrates on untagged elastic ρ^0 photoproduction with the momentum of the scattered proton measured in the FPS horizontal detectors. Subsequently the resolved $\gamma p \rightarrow \rho^0 p$ process is discussed in the VDM framework as an elastic hadron-hadron interaction $\rho^0 p \rightarrow \rho^0 p$.

Organization of the Contents

Chapter 2 contains a short overview of the physics of elastic vector meson photoproduction in γp interactions including the phenomenology of diffraction, Vector Dominance and the Regge formalism. Then the elastic photoproduction as the subject of the present work is discussed.

In chapter 3 the H1 detector at HERA is briefly described focusing at those detectors which are relevant for elastic ρ^0 -meson production: the central tracking system and its triggering ability, the H1 calorimeters and the luminosity detectors.

Chapter 4 contains a review of the horizontal stations of the Forward Proton Spectrometer (FPS). The subjects of this chapter are: detector components, mechanics and detector positions, track reconstruction, calibration and proton momentum measurement.

Chapter 5 describes the basic data analysis steps: selection criteria, background investigation, vertex analysis, luminosity measurement and photon flux estimation for the kinematic region of selected events.

Chapter 6 presents the Monte Carlo simulation treatment and a comparison of experimental with simulated data the study of acceptance, trigger and reconstruction efficiencies.

The results of the current analysis are presented in chapter 7. The differential cross sections $d\sigma/dM_{\pi\pi}$ and $d\sigma/d|t|$ of elastic ρ^0 -meson photoproduction are obtained and extrapolated to the full kinematic region. The extrapolated total cross section of elastic ρ^0 photoproduction is compared with previous measurements.

A brief summary of this thesis is given in Chapter 8.

Chapter 2

Physics Aspects

In this chapter the main aspects of the elastic photoproduction are discussed. The basic steps to understanding of virtual photon – proton (γp) elastic processes are the Vector Dominance Model [11, 12, 13] and Regge theory [14, 15, 16].

The cross section of particle interactions is proportional to the scattering (transition) amplitude $T(s, t)$ of the process:

$$\frac{d\sigma}{dt} \propto |T(s, t)|^2 \quad . \quad (2.1)$$

Here s and t are the Lorentz invariant variables which are defined for a two-body reaction $A + B \rightarrow C + D$ through their four-momentum vectors p_i , ($i=A, B, C, D$):

$$s = (p_A + p_B)^2 = (p_C + p_D)^2 \quad (2.2)$$

$$t = (p_A - p_C)^2 = (p_B - p_D)^2 \quad . \quad (2.3)$$

There s and t are termed the centre of mass energy (CME) squared and the four-momentum transfer squared, respectively. The behaviour of the total cross section for diffractive hadron interactions at high s is described by the *Optical Theorem* [17]. According to the Optical Theorem the total cross section is proportional to the imaginary part of the transition amplitude:

$$\sigma_{tot} \propto s^{-1} \cdot \Im T(s, t) \quad (2.4)$$

and restricted by the *Froissart bound* [47]:

$$\sigma_{tot} \lesssim C \cdot \ln^2 s \quad , \quad s \rightarrow \infty \quad . \quad (2.5)$$

As discussed later, the transition amplitude in the *Regge model* is $T(s, t) \sim s^{\alpha(t)}$. The Optical Theorem in the Regge frame connects the total cross section with the elastic cross section by a logarithmical rise of the elastic cross section. Hence the differential cross section has exponential behaviour with growing s (see also Eq. 2.30, 2.31):

$$\frac{d\sigma}{dt} = A \cdot e^{-bt} \sim s^{2\alpha(t)-2} \quad . \quad (2.6)$$

The exponent b in equation 2.6, termed *b-slope*, is related to the radius of the proton interaction (see page 97).

2.1 Kinematics

The kinematics of the elastic photoproduction process in ep scattering is illustrated in the diagram 2.1. Particles involved in the ep interaction are subdivided into three groups, which are described in table 2.1.

Group	Particle	four-momentum
1.	Incoming electron e	$k = (E_e, 0, 0, -E_e)$;
	Incoming proton p	$P = (E_p, 0, 0, E_p)$;
2.	Quasi-real exchange γ	$q = k - k'$;
	Pomeron \mathbb{P} – virtual exchange object	$p_{\mathbb{P}} = P - P'$;
3.	Scattered electron $e'(k')$	$k' = (E'_e, p_{x,e}, p_{y,e}, p_{z,e})$;
	All outgoing hadrons h	$p_h = (E_h, p_{x,h}, p_{y,h}, p_{z,h})$.

Table 2.1: Four-momenta of particles, participating in the photoproduction process of the ep interaction. These are subdivided into the groups: 1) *incoming*, 2) *intermediate*, 3) *outgoing* particles.

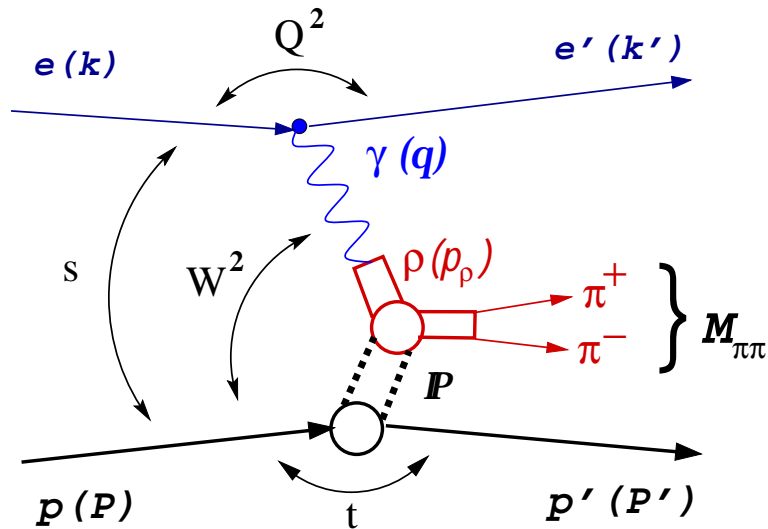


Figure 2.1: The diagram of the ρ^0 photoproduction process. $M_{\pi\pi}$ is the invariant mass reconstructed from the ρ -meson decay pions momenta. The proton momentum fraction IP , termed *Pomeron*, denotes the Reggeon-like virtual object (see Sec. 2.4) which is emitted by the proton and has the quantum numbers of vacuum.

In case of untagged photoproduction the scattered electron is not detected and the only possibility to define the process kinematics is to use variables of incoming particles and outgoing hadrons (see [18, 19]).

The CME squared in ep scattering at the HERA collider is 101 200 GeV² for the electron and proton beam energies of 27.6 GeV and 920 GeV, respectively. The CME squared of ep scattering is expressed as:

$$s = (k + P)^2 \approx 4E_e E_p \quad . \quad (2.7)$$

The scaling variable y , called *inelasticity*, and the electron four-momentum transfer squared from the incoming to the outgoing electron are defined as:

$$y \equiv \frac{P \cdot q}{P \cdot k} \quad ; \quad Q_e^2 \equiv -(k - k')^2 \quad . \quad (2.8)$$

The ratio

$$x = \frac{Q^2}{sy}$$

defines the Bjorken scaling variable. According to momentum conservation, y and Q^2 may be expressed in terms of the outgoing hadrons with a hadronic four-vector $p_h = (E_h, p_{x,h}, p_{y,h}, p_{z,h})$ as done by F.Jacquet and A.Blondel [20]:

$$\begin{aligned} y &= \frac{P \cdot (p_h - P)}{P \cdot k} = \frac{P \cdot p_h}{2E_e E_p} = \\ &= \frac{E_p E_h - E_p p_{z,h}}{2E_e E_p} = \frac{E_h - p_{z,h}}{2E_e} \quad ; \end{aligned} \quad (2.9)$$

$$Q_h^2 \simeq \frac{p_{x,h}^2 + p_{y,h}^2}{1 - y} \quad . \quad (2.10)$$

In the current analysis the electron is not tagged and thus, Q_e^2 not measured, but Q_h^2 is reconstructed and denoted as Q^2 .

The CME squared of the γp system $W^2 = (P + q)^2$ is equivalent to the invariant mass of the hadronic final state. For large momenta and $Q^2 \rightarrow 0$ it can be written as:

$$W^2 \approx 4E_\gamma E_p = 2E_p \cdot (E_h - p_{z,h}) = ys \quad . \quad (2.11)$$

The fractional momentum of the scattered proton, called *elasticity* z is defined as:

$$z = \frac{P \cdot p_\rho}{P \cdot q} \approx \frac{E'_p}{E_p} \quad . \quad (2.12)$$

The four-momentum transfer at the proton vertex is:

$$t = (P - P')^2 = (p_h - q)^2 \approx -p_{t,p}^2 \quad . \quad (2.13)$$

The fractional proton momentum z and the proton four-momentum transfer t are reconstructed in the current analysis by the scattered proton measurement in the horizontal stations of the H1 Forward Proton Spectrometer those are discussed in chapter 4.

2.2 Photon Flux

The original idea of photon flux belongs to E. Fermi [21] who noticed that one can consider the field of an electron at high energies as photons emitted by this electron in a certain frequency ν range. According to that, the cross section of diffractive interaction of an electron off a proton, σ_{ep} , can be parametrized by the spectrometric factor $f_\gamma(\nu)$ which can be interpreted as *photon density*.

$$\frac{d\sigma}{d\nu} = f_\gamma(\nu) \cdot \sigma \quad .$$

Ten years later this idea was introduced by E.J. Williams [22] and C.F. von Weizsäcker [23] for charged particle interactions from matter and it was improved later in [24, 25, 26, 27, 28]. This parametrization method became known as *Equivalent Photon Approximation*.

The photon flux depends on the γ polarization. The transversely and longitudinally polarized photons are described by Φ_T and Φ_L flux factors, respectively:

$$\Phi_T(y, Q^2) = \frac{\alpha}{2\pi Q^2} \cdot \left[\frac{1 + (1-y)^2}{y} - \frac{2(1-y)}{y} \cdot \frac{Q_{min}^2}{Q^2} \right] \quad , \quad (2.14)$$

$$\Phi_L(y, Q^2) = \frac{\alpha}{2\pi Q^2} \cdot \frac{2(1-y)}{y} \quad (2.15)$$

and

$$Q_{min}^2 = \frac{m_e^2 \cdot y^2}{(1-y)} \quad , \quad (2.16)$$

where Q_{min}^2 is the minimum kinematically allowed photon virtuality value, α is the fine structure constant and m_e is the electron mass.

In this work the photon is supposed to be transversely polarized. The agreement of the photon polarization generated in Monte Carlo with data one can see in the azimuthal angle distribution in the ρ^0 decay system shown in figure 6.6c.

If the longitudinal contribution of the photon polarization is neglected the photon flux is calculated as [29, 30]:

$$\mathcal{F}_{\gamma/e} = \int_{y_{min}}^{y_{max}} \int_{Q_{min}^2}^{Q_{max}^2} \Phi_T(y, Q^2) dy dQ^2 \quad . \quad (2.17)$$

The photon flux $\mathcal{F}_{\gamma/e}$ of formula 2.17 is integrated by numerical calculation.

2.3 Vector Dominance Model

The uncertainty principle allows that for a short time photons can fluctuate into a particle-antiparticle pair. Fluctuations into virtual lepton pairs were understood and described by QED. The idea that the photon fluctuates into quark-antiquark ($q\bar{q}$) pairs was realized in the Vector Dominance Model (VDM) [11, 31]. The VDM attempts to model strong interactions as a gauge theory where the vector mesons ρ^0 , ω and ϕ play the rôle of the gauge bosons. VDM asserts that the virtual photon converts first into a vector meson and then couples to the hadron.

Both space-like ($e p$) and time-like ($e^+ e^-$) photons are discussed in the VDM. The corresponding s - and t - channel diagrams are shown in figure 2.2. These diagrams illustrate the process of ρ^0 production which can be subdivided in the VDM frame into the following three stages: 1) photon emittance by the electron; 2) photon fluctuation into the ρ -meson; 3) ρ -meson decay.

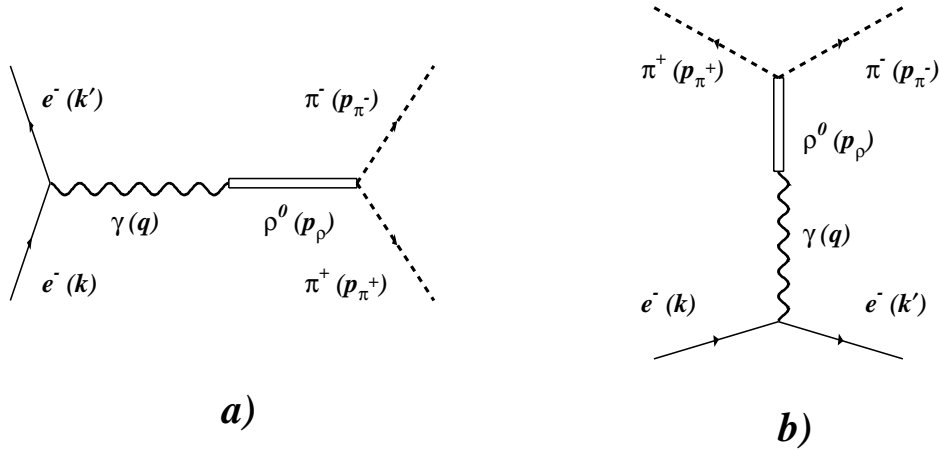


Figure 2.2: *Virtual γ fluctuation into a hadronic state. a) Space-like channel ($q^2 < 0$) reveals at the mass shell by interaction with hadron. b) Time-like channel ($q^2 > 0$): e^+e^- annihilation to $\pi^+\pi^-$.*

The VDM accommodates the photon duality conception where the photon $|\gamma\rangle$ is represented as a superposition of a *bare* photon $|\gamma_b\rangle$ and *hadronic* photon $|h\rangle$ and only the hadronic component (which has the same quantum numbers as the photon) interacts with hadrons:

$$|\gamma\rangle = \sqrt{Z_3}|\gamma_b\rangle + \sqrt{\alpha_{el}}|h\rangle \quad . \quad (2.18)$$

Here Z_3 is the normalization constant and α_{el} is the electromagnetic coupling constant. In the VDM the hadronic component of the photon is represented as a superposition of vector mesons:

$$\sqrt{\alpha_{el}}|h\rangle = \sum_{V=\rho,\omega,\phi} \frac{e}{f_V}|V\rangle \quad . \quad (2.19)$$

In the VDM scheme a vector field V_μ , and conserved vector current τ_μ ¹ are introduced in analogy to the electromagnetic field A_μ and conserved electromagnetic current j_m of QED.

The VDM phenomenology asserts that a vector meson state couples to the photon and V_μ in the VDM (like A_μ in QED) satisfies the transversality condition $\partial_\mu V_\mu = 0$. The effective Lagrangian of photon fluctuation to the ρ -meson \mathcal{L}_ρ is not gauge invariant and therefore the VDM assumes the *field current identity* [32] expressed as:

$$e j_\mu = \aleph_\rho \tau_\mu \quad , \quad (2.20)$$

where \aleph_ρ is the amplitude of the photon conversion into a ρ^0 -meson. The amplitude \aleph_ρ is proportional to the ρ^0 -meson mass squared:

$$\aleph_\rho = \frac{e}{f_\rho} \cdot m_\rho^2 \quad (2.21)$$

and the normalization constant e/f_ρ is chosen as described in [33]. Thus, the VDM asserts that a virtual photon fluctuates into a vector meson state independently of its interactions.

Taking into account the assumption of equation 2.20 the interaction Lagrangian is:

$$\mathcal{L}_\rho = \aleph_\rho V_\mu A^\mu \quad . \quad (2.22)$$

Due to the assumption of formula 2.20 the scattering amplitude of $\gamma p \rightarrow \rho^0 p$ ($T_{\gamma p \rightarrow \rho^0 p}$) can be factorized into the amplitude of elastic $\rho^0 p \rightarrow \rho^0 p$ process ($T_{\rho^0 p \rightarrow \rho^0 p}$) by the pionic form-factor $F_\pi(q^2)$:

$$T_{\gamma p \rightarrow \rho^0 p}(s, t, q^2) = F_\pi(q^2) \cdot T_{\rho^0 p \rightarrow \rho^0 p}(s, t, q^2) \quad . \quad (2.23)$$

The pionic electromagnetic form-factor is calculated as:

$$F_\pi(q^2) = \left(\frac{f_{\rho\pi\pi}}{f_\rho} \right) \cdot \frac{m_\rho^2}{(m_\rho^2 - q^2 - im_\rho\Gamma_\rho)} \quad , \quad (2.24)$$

where the ρ -meson with the mass of $m_\rho = 2\sqrt{m_\pi^2 + |\mathbf{p}_\pi|^2}$ couples directly to the pionic current. The Γ_ρ is the width of the ρ^0 -meson resonant state which depends on the decay pion momentum:

$$\Gamma_\rho(\rho^0 \rightarrow \pi^+\pi^-) = \frac{2}{3} \cdot \frac{f_{\rho\pi\pi}^2}{4\pi} \cdot \frac{|\mathbf{p}_\pi|^3}{m_\rho^2} \quad . \quad (2.25)$$

The formula 2.23 explains the term *elastic* of the ρ^0 -meson photoproduction process in $\gamma p \rightarrow \rho^0 p$ scattering. Concentrating on ρ^0 photoproduction one has to take into account the coupling of the photon to non-resonant $\pi^+\pi^-$ pair production which can be also described by field current identity [34]. Thus, in addition to the scattering amplitude $T_{\rho^0 p \rightarrow \rho^0 p}(s, t, q^2)$ of the resonant ρ^0 production the amplitude $T_{\gamma p \rightarrow \pi^+\pi^- p}(s, t, q^2)$ has to be considered [35, 36]. The experimental results of the non-resonant interfering contribution are discussed in chapter 7.

¹The vector current τ_μ can be coupled then to the hadronic current J_μ , introduced for the hadronic interaction of a ρ^0 -meson with a proton.

2.4 Regge Model

T.Regge considers the particle orbital momentum as a generalized complex value in the radial Schrödinger wave equations and discusses the behavior of scattering amplitudes in relation to potential scattering [14, 15, 16, 37]. In Regge theory the partial wave expansion of the scattering amplitude $T(s, t, \cos \theta)$:

$$T(s, t, \cos \theta) = \sum_{l=0}^{\infty} (2l+1) \cdot \frac{g(s, t)}{l - \alpha(s, t)} \cdot P_l(\cos \theta) \quad (2.26)$$

can be expressed by introducing the contour integral over a path C in the complex l plane [38]:

$$\begin{aligned} T(s, t, \cos \theta) \simeq & -\pi \sum_k \frac{(2\alpha_k(s, t) + 1)}{\sin \pi \alpha_k(s, t)} \cdot P_{\alpha_k}(\cos \theta) + \\ & + \frac{i}{2} \oint_C \frac{(2l+1)}{\sin \pi l} \cdot \frac{g(s, t)}{l - \alpha(s, t)} \cdot P_l(\cos \theta) dl \end{aligned} \quad (2.27)$$

Here $P_l(\cos \theta)$ are the Legendre polynomials, $\alpha_k(s, t)$ is the *Regge pole* (shadow state [15]) defined in the complex α -plane of the angular momentum at certain values of s and t , l takes the integer values $l = 0, 1, 2, \dots$ of angular momentum and $g(s, t)$ is the coupling factor of a Regge pole to interacting particle.

The contribution from the contour integral in formula 2.27 is termed “background integral” to the sum which represents the contribution from k Regge poles. This complex angular momentum method is used in the phenomenological description of hadronic processes at high energies [28, 39, 40].

Regge Trajectories

The sequence of Regge poles is interpreted as a moving pole with $l = \alpha(s, t)$. The function $\alpha(s, t)$ is determined in the α -plane at certain values of Mandelstam variables s and t . By changing s and t the Regge pole transforms to a *Regge trajectory* such that $\alpha(s_1, t_1) = l_1, \dots$ and each state of $\alpha(s_k, t_k)$ corresponds to a bound state or resonance with $l = l_k$, mass M_k and width Γ_k such that $t_k = M_k^2 - i M_k \Gamma$. In our case of fixed s the Regge trajectory is denoted as $\alpha(t) = \alpha(s, t)|_{s=const}$ and defined as spin of the mesons with the same quantum numbers:

$$J = \alpha(t) = \Re \alpha(t) + i \cdot \Im \alpha(t) \quad . \quad (2.28)$$

As was observed by Chew and Frautschi [41] the spin values of resonances with the same quantum numbers versus their mass squared lie on straight lines. Thus, the observed resonances may be compiled to the trajectories as shown for mesons at the Chew-Frautschi plot of figure 2.3 .

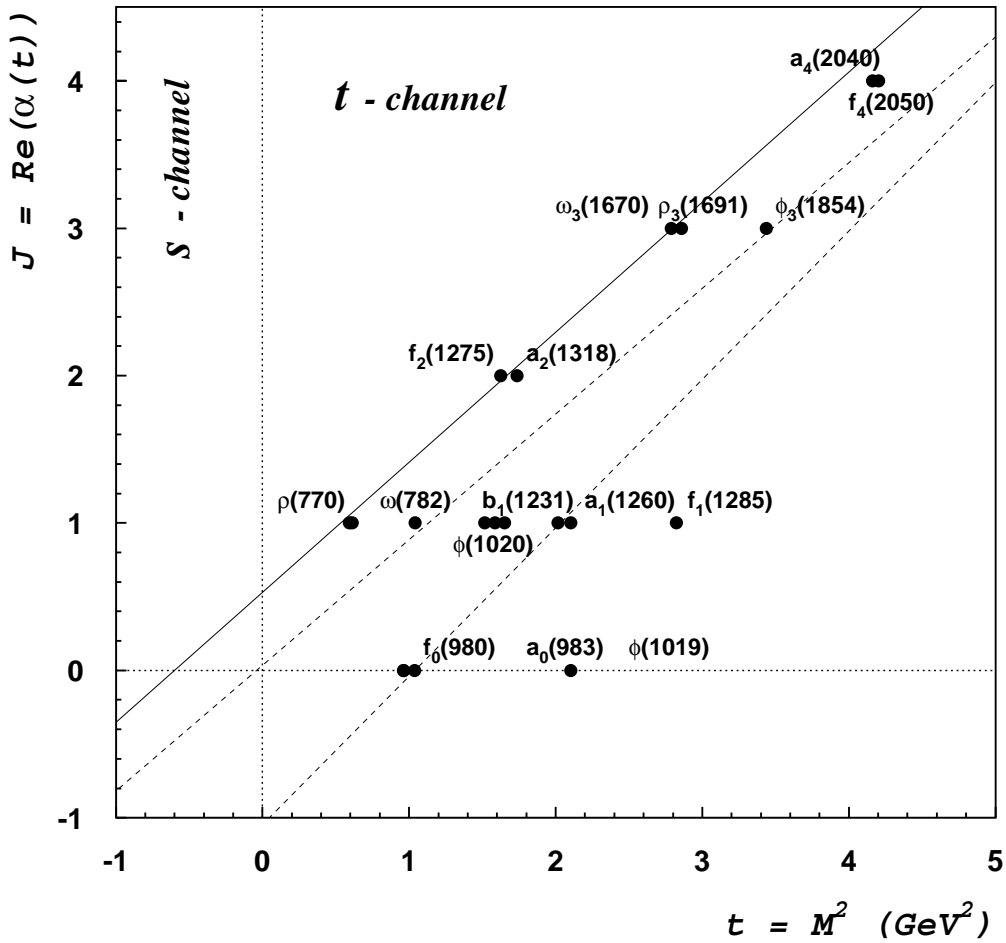


Figure 2.3: *Regge trajectories: the case of $t < 0$ (s -channel process) corresponds to hadron scattering, while the case of $t > 0$ (t -channel process) corresponds to resonance production.*

The Regge model assumes that all processes with mesons which belong to the same trajectory should have a similar behavior. Hence it considers the exchange of trajectories instead of individual particles. Such a superposition of Regge states which belong to the same trajectory is termed *Reggeon* (\mathbb{R}).

Thus, the exchange of a Reggeon is equivalent to the exchange of several particles with spin states $J = 0, 1, 2, \dots$. The spin representation by a trajectory of figure 2.3 is expressed from equation 2.28 by the following linear form:

$$\alpha(t) = \alpha(0) + \alpha' \cdot t \quad . \quad (2.29)$$

Here $\alpha(0)$, the value of $\alpha(t)$ at $t = 0$, is called the *intercept* of the Regge trajectory. The trajectories of existing particles have $\alpha(0) < 1$. According to the optical theorem

the total cross section is related to the imaginary part of the transition amplitude (see Eq. 2.27). For the elastic processes the real part of the transition amplitude at high energies is in the vicinity of zero, and the differential cross section of elastic process is proportional the total photoproduction cross section squared:

$$\left. \frac{d\sigma}{d|t|} \right|_{t \rightarrow 0} \propto \sigma_{tot}^2 \quad . \quad (2.30)$$

Thus, the conclusion from equations 2.6 and 2.30 is that the total cross section for $\alpha(0) < 1$ should decrease with CME:

$$\sigma_{tot} \sim \left(\frac{s}{s_0} \right)^{\alpha(0)-1} \quad . \quad (2.31)$$

The experimental results show that at high energies the total cross section increase with rising CME. Therefore, to satisfy the experimental results a trajectory with $\alpha(0) \gtrsim 1$ has to be introduced in the Regge model. Though this idea was originally suggested by V.N.Gribov, the trajectory with $\alpha(0) \gtrsim 1$ was called by M.Gell-Mann as Pomeron after the theory of I.Ya.Pomeranchuk [27]. Later the Pomeron was shortened to *Pomeron*. The Pomeron trajectory may be represented as a compound system of several trajectories. The trajectory which may contain the Reggeons, mesons and Pomerons is called *multiple Pomeron* [42, 43, 44].

The Pomeron trajectory [45, 46] has to be consistent with the Froissart bound expressed in formula 2.5. This boundary condition [47, 48] has been derived from the unitarity of the S-matrix (see for example Ref. [49]). The form of the unitarity solution for diffractive processes with Pomeron exchange can be found in [50, 51, 52]. It has been shown in [53, 54, 55] that the multiple Pomeron obeys the Froissart asymptotics and unitarity. The slope and intercept values of the π -meson, Reggeon and Pomeron trajectories are:

$$\begin{array}{ll} \pi \quad (\text{pion}) & \alpha_{\pi}(t) \approx 0.00 + 1.00 \cdot t \\ \mathcal{R} \quad (\text{Reggeon}) & \alpha_{\mathcal{R}}(t) \approx 0.5475 + 0.90 \cdot t \\ \mathcal{P} \quad (\text{Pomeron}) & \alpha_{\mathcal{P}}(t) \approx 1.0808 + 0.25 \cdot t \end{array} \quad (2.32)$$

The Monte Carlo simulation used in the current analysis is based on single and multiple Pomeron exchange models (see Sec. 2.6).

Shrinkage

The asymptotic behavior of the scattering amplitude $T(s, t) \sim (\cos \theta)^{\alpha(t)}$ of a Regge trajectory [14] obtained from expression 2.27 was predicted in phenomenological description when $s \rightarrow \infty$ and $t < 0$. The transition amplitude of the $2 \rightarrow 2$ hadronic process in the Regge approach is represented in Mandelstam form [56]:

$$T(s, t) \xrightarrow{s \rightarrow \infty} g(t) \cdot \left(\frac{s}{s_0} \right)^{\alpha(t)} \quad , \quad (2.33)$$

where $\alpha(t)$ is a spin factor of the Regge trajectory with a linear t dependence of equation 2.29, s_0 is a scale factor and $g(t)$ is the coupling factor.

In case of the Pomeron trajectory the function $g(t)$ factorizes in the proton-Pomeron state and Pomeron-meson state coupling constants $g_{p,\mathbb{P}}$ and $g_{\mathbb{P},V}$, respectively. These coupling constants are marked in diagram 2.1 as open balls. Thus, taking into account equations 2.29 and 2.33, the transition amplitude of the process illustrated in diagram 2.1 is given by:

$$T(s, t) = s_0 g_{p,\mathbb{P}}(0) g_{\mathbb{P},V}(0) \left(\frac{s}{s_0} \right)^{\alpha_{\mathbb{P}}(0)} \cdot e^{\beta_{\mathbb{P}}(s) \cdot t} \quad , \quad (2.34)$$

where the slope of the exponent is described by a term with a logarithmic dependence on s :

$$\beta_{\mathbb{P}}(s) = \beta_{\mathbb{P}}(0) + \alpha'(0) \cdot \ln \left(\frac{s}{s_0} \right) \quad ; \quad \beta_{\mathbb{P}}(0) = \frac{\beta_{p,\mathbb{P}}(0)}{2} + \frac{\beta_{\mathbb{P},V}(0)}{2} \quad . \quad (2.35)$$

The $g_{p,\mathbb{P}}(0)$ and $g_{\mathbb{P},V}(0)$ are the momentum transfer independent parts of the coupling constants related to the proton-Pomeron and Pomeron-meson vertices, respectively:

$$g_{p,\mathbb{P}}(t) = g_{p,\mathbb{P}}(0) \cdot e^{\frac{1}{2}\beta_{p,\mathbb{P}}(0) \cdot t} \quad ; \quad g_{\mathbb{P},V}(t) = g_{\mathbb{P},V}(0) \cdot e^{\frac{1}{2}\beta_{\mathbb{P},V}(0) \cdot t} \quad . \quad (2.36)$$

At high energies the single Pomeron amplitude of equation 2.34 is transformed by inelastic absorptive corrections [57]. The absorptive corrections are expressed by multiple Pomeron exchange within Gribov's Reggeon field theory [45, 46, 52]. The main contribution of these corrections results from diffractive intermediate states with masses less than ~ 5 GeV.

The phenomenological description of the differential cross section in dependence on the proton momentum transfer t is:

$$\frac{d\sigma}{dt} \propto \left(\frac{s}{s_0} \right)^{2[\alpha(0)t-1]} \cdot e^{b(s)t} \quad , \quad (2.37)$$

where the transition amplitude resembles equation 2.34 and $b(s) = 2 \cdot \beta(s)$. The formula 2.37 determines the s and t dependence of the cross section. Due to negative values of t in hadron scattering, the exponential tilt of the t dependence becomes sharper at increasing s . The fact that the cross section shrinks with increasing s and the peak of $d\sigma/dt$ becomes sharper at small t is called *shrinkage*.

2.5 Elastic ρ^0 Photoproduction

Elastic γp Cross Section in ep Interactions

The inclusive cross section of ep collisions proceeding via photon exchange consists of the partial γp cross sections $\sigma_{\gamma p}^T$ and $\sigma_{\gamma p}^L$ which correspond to the scattering of transversally and longitudinally polarized photons. The relation of σ_{ep} and $\sigma_{\gamma p}$ is provided by the transversal and longitudinal photon flux factors Φ_T and Φ_L :

$$\frac{d^2\sigma_{ep}^{tot}}{dy dQ^2} = \Phi_T(y, Q^2) \cdot \sigma_{\gamma p}^T(W) + \Phi_L(y, Q^2) \cdot \sigma_{\gamma p}^L(W) \quad . \quad (2.38)$$

The flux factors Φ_T and Φ_L are expressed by equations 2.14 and 2.15. At low photon virtuality Q^2 , the total cross section of γp scattering, $\sigma_{\gamma p}^{tot} = \sigma_{\gamma p}^T + \epsilon \cdot \sigma_{\gamma p}^L$, is dominated by the transverse part, i.e. $\sigma_{\gamma p}^T \rightarrow \sigma_{\gamma p}^{tot}$ and $\sigma_{\gamma p}^L \rightarrow 0$ at $Q^2 \rightarrow 0$.

Within the VDM, discussed in section 2.3, the elastic vector meson (V) photoproduction in γp scattering is equivalent to the photon fluctuating in a vector meson state (see equation 2.23) with its subsequent elastic scattering off the proton, $Vp \rightarrow Vp$, as sketched in figure 2.1. Thus, the total $\gamma p \rightarrow Vp$ cross section is proportional to the incoherent sum of the elastic vector mesons cross sections:

$$\sigma_{\gamma p \rightarrow Vp} \propto \sum_V \lambda_V \sigma_{Vp} \quad . \quad (2.39)$$

The photon fluctuates into these vector mesons V which have the same quantum numbers as the photon. The coupling coefficients λ_V for $V = \rho^0, \omega$ and ϕ are determined experimentally [58]:

$$\lambda_\rho \approx 2.2, \quad \lambda_\omega \approx 23.6, \quad \lambda_\phi \approx 18.4.$$

The quark-flavor structure of the vector mesons and the assumption of the flavor-independent production mechanism results with production rates which depend on the vector meson wave functions. The wave functions of ρ^0, ω and ϕ are described in SU(3) by the following superposition of quark-antiquark pairs:

$$|\rho\rangle \sim \frac{1}{\sqrt{2}}(|u\bar{u}\rangle - |d\bar{d}\rangle) \quad ; \quad |\omega\rangle \sim \frac{1}{\sqrt{2}}(|u\bar{u}\rangle + |d\bar{d}\rangle) \quad ; \quad |\phi\rangle \sim |s\bar{s}\rangle \quad . \quad (2.40)$$

Thus, the predicted ratios of the vector meson decay widths are:

$$\rho^0 : \omega : \phi = \left(\frac{1}{\sqrt{2}}\frac{3}{3}\right)^2 : \left(\frac{1}{\sqrt{2}}\frac{1}{3}\right)^2 : \left(\frac{1}{3}\right)^2 = 9 : 1 : 2, \quad (2.41)$$

i.e. ρ^0 -meson production is expected to be dominant over ω and ϕ production.

The total elastic ρ^0 -meson cross section calculated for $\gamma p \rightarrow \rho^0 p$ process is expressed by the following relation:

$$\sigma(\gamma p \rightarrow \rho^0 p) = \frac{N_\rho}{\mathcal{F}_{\gamma/e} \cdot \mathcal{L} \cdot \epsilon \cdot \mathcal{A}} \quad , \quad (2.42)$$

where N_ρ is the number of selected elastic ρ events, $\mathcal{F}_{\gamma/e}$ is the photon flux of formula 2.17, \mathcal{L} is the luminosity, ϵ is the measurement efficiency and \mathcal{A} is the acceptance of the experimental apparatus.

Angular Distribution of ρ^0 Photoproduction

The production and decay angular distribution of elastically produced ρ^0 -meson defines three scattering planes which are sketched in figure 2.4.

The ρ^0 -meson production is defined in the Jackson coordinate system [59], with the orthogonal unit vectors: $\mathbf{z} = \frac{\mathbf{q}}{|\mathbf{q}|}$, $\mathbf{y} = \frac{\mathbf{q} \times \mathbf{P}}{|\mathbf{q} \times \mathbf{P}|}$, $\mathbf{x} = \mathbf{y} \times \mathbf{z}$, where the \mathbf{z} -axis direction extends along the incoming proton beam direction.

The ρ^0 -meson decay is defined in the *helicity coordinate system* with orthogonal unit vectors: $\mathbf{z} = \frac{\mathbf{p}_\rho}{|\mathbf{p}_\rho|}$, $\mathbf{y} = \frac{\mathbf{q} \times \mathbf{p}_\rho}{|\mathbf{q} \times \mathbf{p}_\rho|}$, $\mathbf{x} = \mathbf{y} \times \mathbf{z}$, where the \mathbf{z} -axis direction is given by the ρ^0 -meson direction. The helicity coordinate system is turned along the momentum of π^+ from the ρ^0 decay: $\mathbf{x} \equiv \pi$. The polar helicity angle θ^* shown in figure 2.4 is defined in CMS of ρ^0 .

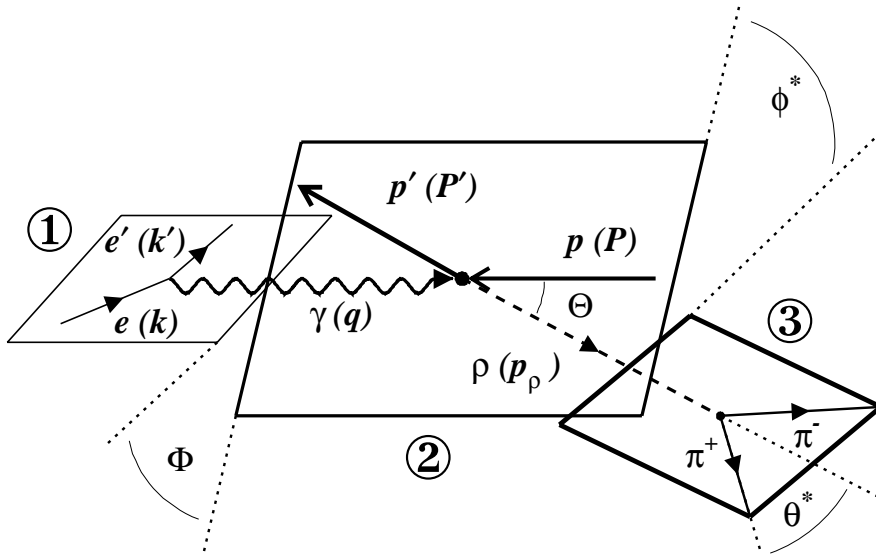


Figure 2.4: Elastic ρ^0 -meson photoproduction angular planes in ep scattering: (1) – the plane of the electron scattering, (2) – the plane of ρ^0 -meson production, (3) – the plane of ρ^0 -meson decay.

In case of untagged photoproduction there is no information about the electron scattering plane because the electron is lost in the beam pipe. The usage of the Forward Proton Spectrometer (described in detail in chapter 4) allows to determine the plane of ρ^0 production by measurement of the scattered proton momentum \mathbf{P}' .

The polarization of the ρ -meson is identified in the plane of its decay products by the angular distribution of the $\pi^+\pi^-$ measured in the H1 central tracker. The angular distribution of $\pi^+\pi^-$ is defined in the CMS of ρ^0 by the polar helicity angle θ^* and azimuthal, Toller [60], angle ϕ^* :

$$\cos \theta^* = \frac{\mathbf{p}_\rho \cdot \mathbf{p}_\pi}{|\mathbf{p}_\rho| \cdot |\mathbf{p}_\pi|} = \pi \cdot \mathbf{z} \quad ; \quad \cos \phi^* = \mathbf{y} \cdot \frac{\mathbf{z} \times \pi}{|\mathbf{z} \times \pi|} \quad . \quad (2.43)$$

The measured values of θ^* and ϕ^* are presented in figure 6.6.

2.6 Monte Carlo Models

In the current analysis two Monte Carlo (MC) generators, DIFFVM [61] and PHOJET [62] are used. Both generators are adapted to the H1 analysis software.

DIFFVM

The DIFFVM [61] generator simulates photoproduction processes in the framework of the Vector Dominance and Regge models. The exchange trajectory is taken as single Pomeron defined by: $\alpha(t) = 1.0808 + 0.25 \cdot t$. The simulation of the elastic vector meson scattering consists of the following three steps:

1) The virtual photon is simulated in the kinematic range of $Q_{min}^2 < Q^2 < Q_{max}^2$ and $y_{min} < y < y_{max}$ according to:

$$Q^2 = Q_{min}^2 \cdot e^{R_1 \ln \frac{Q_{max}^2}{Q_{min}^2}}, \quad y = y_{min} \cdot e^{R_2 \ln \frac{y_{max}}{y_{min}}}, \quad (2.44)$$

where R_1 and R_2 are uniformly distributed random numbers between 0 and 1, and the values of Q_{min}^2 , Q_{max}^2 and y_{min} , y_{max} are defined by the user.

2) The transversal and longitudinal γp cross sections $\sigma_{\gamma p}^T$ and $\sigma_{\gamma p}^L$ are simulated using the following expressions:

$$\sigma_{\gamma^* p}^T = \sigma_{\gamma p} \cdot \left(\frac{1}{1 + \frac{Q^2}{m_V^2}} \right)^2, \quad \frac{\sigma_{\gamma^* p}^L}{\sigma_{\gamma^* p}^T} = \xi \cdot \frac{Q^2}{m_V^2}, \quad (2.45)$$

where $\sigma_{\gamma p}$ is the total photon-proton cross section, ξ is a constant factor of order 1 and m_V is the mass of the vector meson (here $m_V = m_\rho$).

The elastic vector meson generation assumes Pomeron exchange with a differential cross section (see Eq. 2.33):

$$\frac{d\sigma}{dt} = \frac{g_{p,P}^2(t) g_{P,V}^2(t)}{16\pi} \cdot s^{2(\alpha_P(t)-1)} \quad (2.46)$$

at fixed centre of mass energy \sqrt{s} and proton momentum transfer t , where $g_{p,P}(t)$ and $g_{P,V}(t)$ are the coupling constants defined in expressions 2.36. The cross section is simulated using the probability function of the input variables $f(\zeta)$. An event is accepted if a random number R is $R < \frac{f(\zeta)}{f(\zeta)_{max}}$, with the ratio of the current to the maximum cross section. Therefore, the number of generated events with ζ is proportional to the cross section which is integrated according to ζ .

3) The vector meson decay is simulated according to the pion form-factor of equation 2.24 assuming that the resonance width is independent of the pion momentum (non-relativistic Breit-Wigner approach). The polar angle θ^* of the decay pion in the rest frame of the ρ^0 (see Fig. 2.4) is generated assuming s -channel helicity conservation. The azimuthal angle ϕ^* between the ρ^0 production and decay planes is generated according to a flat distribution.

PHOJET

A wide spectrum of high energy processes may be generated by PHOJET [62]. The PHOJET generator is based on the two-component Dual Parton Model [63] combined with perturbative QCD. The Dual Parton Model use the phenomenology of duality and Gribov's Reggeon field theory where the hadronic interactions are described by multiple Pomeron exchange. The vector meson production is modeled inside the Regge frame. The unitarization scheme in Gribov's Reggeon field theory connects diffractive and inelastic processes. In case of photoproduction processes the unitarization is used for the calculation of the absorptive corrections.

In γp collisions at HERA, the cross section of photon diffraction dominates even over elastic ρ^o production. Hence the total cross section described by single Pomeron exchange exceeds the Froissart bound. That means that at HERA energies a single Pomeron exchange model becomes invalid.

In PHOJET the dominant unitarity corrections (absorptive corrections) within Gribov's Reggeon theory are performed [64]. The inelastic absorptive corrections due to the diffractive intermediate states dominate at low masses [65, 66]. The unitarization is performed by the unitarity cut on multiple Pomeron exchange amplitudes [57], which are expressed by the unitarity sum over the possible elastic, low-mass and high-mass states.

The transition amplitude of triple-pomeron exchange is characterized by three coupling constants: $g_{p,P}(t)$, $g_{PPP}(t)$, $g_{P,V}(t)$. The vector mesons and the non-resonant $\pi^+\pi^-$ production generated in PHOJET by *triple-pomeron* exchange are sampled according to the ratios:

$$\rho^o : \omega^0 : \phi^0 : \pi^+\pi^- = 75\% : 8\% : 9\% : 8\% \quad (2.47)$$

The mass distributions of the vector mesons generated by PHOJET are approximated by the relativistic Breit-Wigner distribution of equation 2.24.

Chapter 3

H1 Experiment at HERA

In this chapter the H1 experiment situated in the North colliding area of the HERA¹ accelerator is presented. The description emphasizes those components of the H1 detector which are used in the current analysis to reconstruct the ρ^0 -meson and the forward scattered proton. A brief review of the luminosity detectors and the triggering system is also given. The H1 components described here are the central tracking system of drift and proportional chambers and the calorimeters – the main Liquid Argon calorimeter (LAr) and the backward Spaghetti Calorimeter (SpaCal). The subsequent chapter is devoted to the FPS horizontal stations.

3.1 HERA e-p Collider

The electron-proton collider HERA [67] was built in Hamburg. Electrons of 27.6 GeV interact with protons of 920 GeV. Since 1999 HERA increased the proton beam energy from 820 to 920 GeV. A view of the HERA storage rings is presented in figure 3.1. The storage rings are 6336 m long and have four interaction zones called North, West, East and South. The North zone is occupied by the H1 [68] experiment. The South, East and West zones are occupied by the ZEUS [69], HERMES [70], and HERA-B [71], experiments, respectively.

The H1 and ZEUS experiments have been taking electron-proton scattering data since 1992. The physics emphasis of H1 and ZEUS is the study of deep inelastic scattering and of diffractive processes. HERMES carries out investigations of polarized electron beam collisions with polarized gas targets. The HERMES detector operates since 1995. The HERA-B utilizes fixed targets by inserting tungsten wires into the proton beam halo. The HERA-B experiment operated since 1999.

For the injection of electrons and protons into HERA the previous acceleration facilities of DESY are used. On the left side of figure 3.1 one can see the locations

¹Hadron-Electron-Ring-Anlage

of the HERA experiments along the HERA ring. On the right side of figure 3.1, the injection system is sketched.

The storage of electrons pass the following steps: 1) electrons are boosted to 450 MeV by a linear accelerator (e -linac); 2) the electrons are transferred from e -linac to DESY II which accelerates electrons to 7 GeV and injects them into the PETRA ring; 3) in PETRA the electrons are accelerated to 12 GeV; 4) the electrons then are injected into the HERA electron ring where the final ramping up to 27.6 GeV is performed.

The storage of protons has the following steps: 1) protons are produced in a 20 keV source and via a 50 MeV linac transferred to DESY III; 2) in DESY III the protons are accelerated to 8 GeV and transferred to PETRA. 3) PETRA accelerates the protons to 40 GeV; 4) the protons of 40 GeV are injected to the HERA proton ring where the final ramping up to 920 GeV is performed.

The bunch crossing interval at HERA is 96 nsec and the design luminosity is $1.4 \times 10^{31} \text{cm}^{-2} \text{s}^{-1}$. The data of the current analysis are collected from photoproduction events with a measured proton in the Forward Proton Spectrometer with an *operation luminosity* of 2pb^{-1} . (The term “operation luminosity” is introduced in Sec. 5.5). The collected operation luminosity accounts for about 11% of the total integrated luminosity at H1 in spring 1999. Important HERA parameters are listed in table 3.1.

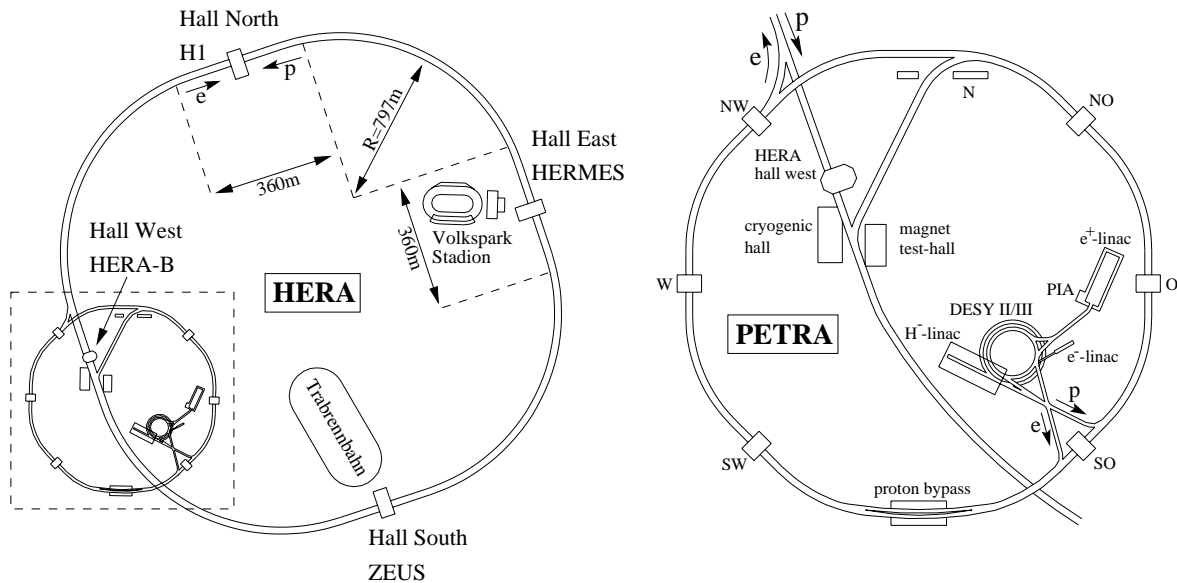


Figure 3.1: Schematic view of the HERA accelerator and its injection system.

3.2 H1 Detector

The design of H1 detector [68] has been developed to study physics of electron-proton scattering. The weight of the H1 detector is around 2800 tons and it has spatial

Characteristic	p	e	units
Nominal energy	920	26.7	GeV
Magnetic field	4.68	0.274	T
Beam current	~ 90	~ 30	mA
Particles per bunch	2.1	0.8	10^{13}
Bunches per ring	180	189	
Filling time	120	40	min
Beam radius	$265^{(H)}, 50^{(V)}$	$280^{(H)}, 50^{(V)}$	10^{-3} mm
Bunch length	85	8.3	mm
Luminosity	1.4×10^{31}		$\text{cm}^{-2} \text{s}^{-1}$

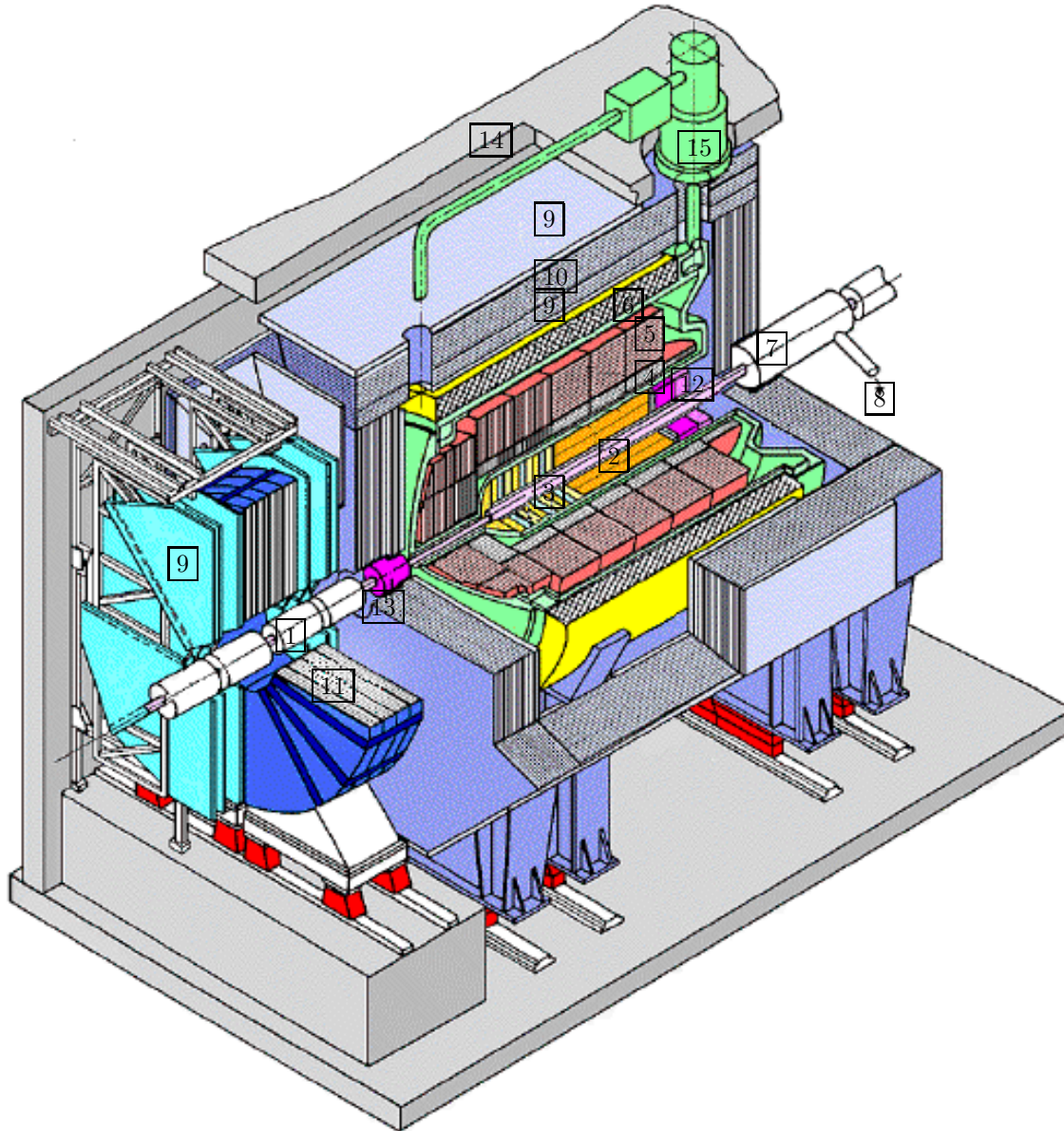
Table 3.1: Nominal HERA parameters (from [72]).

dimensions of $x \times y \times z \approx 12 \times 10 \times 15 \text{ m}^3$. The laboratory frame of H1 is defined as a right-handed coordinate system with the positive z -axis along the proton beam direction. The x -axis points inwards from the beam pipe to the collider ring center. The y -axis points upwards to define a right-handed coordinate system. The azimuthal angle ϕ and the polar angle Θ start along the $+x$ - and $+z$ -axis, respectively, and increase clockwise towards the $+y$ -axis.

The layout of the main H1 detector is shown in figure 3.2. The H1 apparatus has an approximate cylindrical symmetry in the $r - \phi$ plane around the z axis. H1 is layed out differently in forward and backward directions due to the asymmetric beam energies in the collision of electrons and protons. The proton beam direction is termed *forward* region and the electron direction *backward* region. The region around the interaction point is called the *central* part of the H1 detector.

Detectors are twisted around the interaction point as shown in figure 3.2 in the following order from inside outwards:

1. The central, forward and backward tracking devices are the detectors closest to the interaction point. They contain silicon trackers, drift and proportional chambers.
2. The calorimeters surround the tracking system and the beam pipe. The central and forward calorimeter of the H1 apparatus is a segmented Liquid Argon calorimeter (LAr), while the backward region is covered by a Pb-fibre Spaghetti Calorimeter (SpaCal).
3. Around the LAr calorimeter a superconducting coil is placed which provides a uniform solenoidal field of 1.1 T near the interaction region.
4. An instrumented iron return yoke of the magnet covers the whole detector. It is instrumented with 16 layers of limited streamer tubes and serves to register muons and hadronic showers leakage.



- | | | | |
|---|---------------------------------|----|---------------------------------------|
| 1 | Beam pipe and beam magnets | 9 | Muon chambers |
| 2 | Central Tracking Detector | 10 | Instrumented iron yoke |
| 3 | Forward Tracking Detector | 11 | Forward muon toroid |
| 4 | Electromagnetic LAr calorimeter | 12 | Backw. spaghetti calorimeter (SpaCal) |
| 5 | Hadronic LAr calorimeter | 13 | PLUG calorimeter |
| 6 | Superconducting coil | 14 | Concrete shielding |
| 7 | Compensating magnet | 15 | Liquid argon cryostat |
| 8 | Helium supply for 7 | | |

Figure 3.2: A three-dimensional view of the H1 detector. Electrons come from the left front and hit protons which come from the right front into the interaction vertex region (where "2" is written in the picture).

3.3 Tracking System

The H1 tracking system consists of three major detector groups:

1. Central Tracker. The Central Track Detector (CTD) contains concentric drift chambers CJC1 and CJC2, the multi-wire proportional chambers CIP, COP, the z-drift chambers CIZ, COZ, and the Central Silicon Tracker (CST).
2. Forward Tracker. The Forward Track Detector (FTD) consists of *radial* and *planar* drift chambers which are staggered with planar Forward Proportional Chambers (FPC) and transition radiators.
3. Backward Tracker. It contains the Backward Drift Chamber (BDC) and the Backward Silicon Tracker (BST).

The central detectors provide track reconstruction, triggering, particle identification and momentum measurement in a solenoidal magnetic field. Each detector has an independent gas volume, shielding and mounting procedure. All detectors have been tested separately and then combined to one tracking device. A schematic view of the central tracking system is shown in figure 3.3.

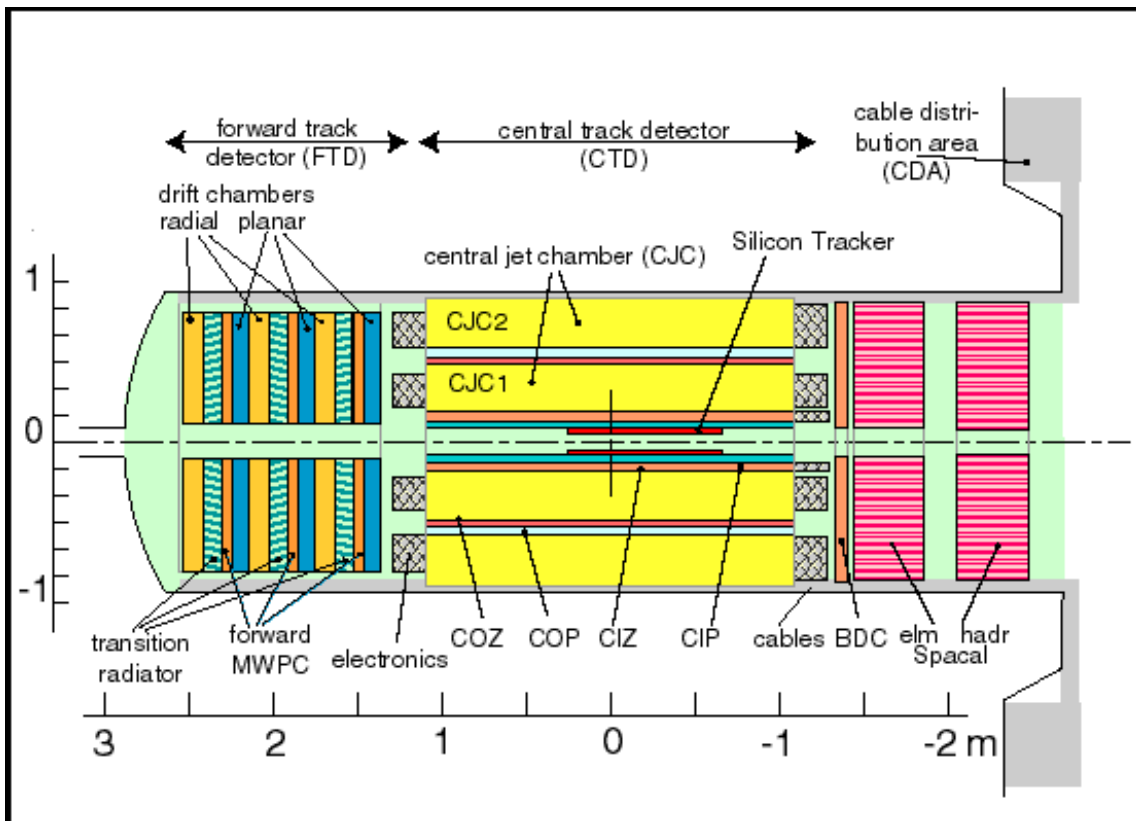


Figure 3.3: Side view of the H1 tracking system. The coordinate system at the plot is scaled in meters for x and y projections.

Central Jet Chambers (CJC)

The basis of the track measurement in the H1 central region are two cylindrical drift chambers: the **C**entral **J**et Chambers CJC1 and CJC2. The wires are strung along 220 cm active length in z direction and cover the polar angle range $15^\circ < \Theta < 165^\circ$. The wires of CJC1 and CJC2 are grouped in cells which are tilted to the radial direction by a Lorentz angle of about 30° . This angle (see Fig. 3.4) is optimized according to the drift of ionization electrons in the magnetic field. Each drift cell is limited by two cathode wire planes in azimuth and by inner and outer carbon fiber cylinders. Some geometrical parameters and measurement characteristics of the CJC are presented in table 3.2. The central track quality conditions are listed in table 3.3.

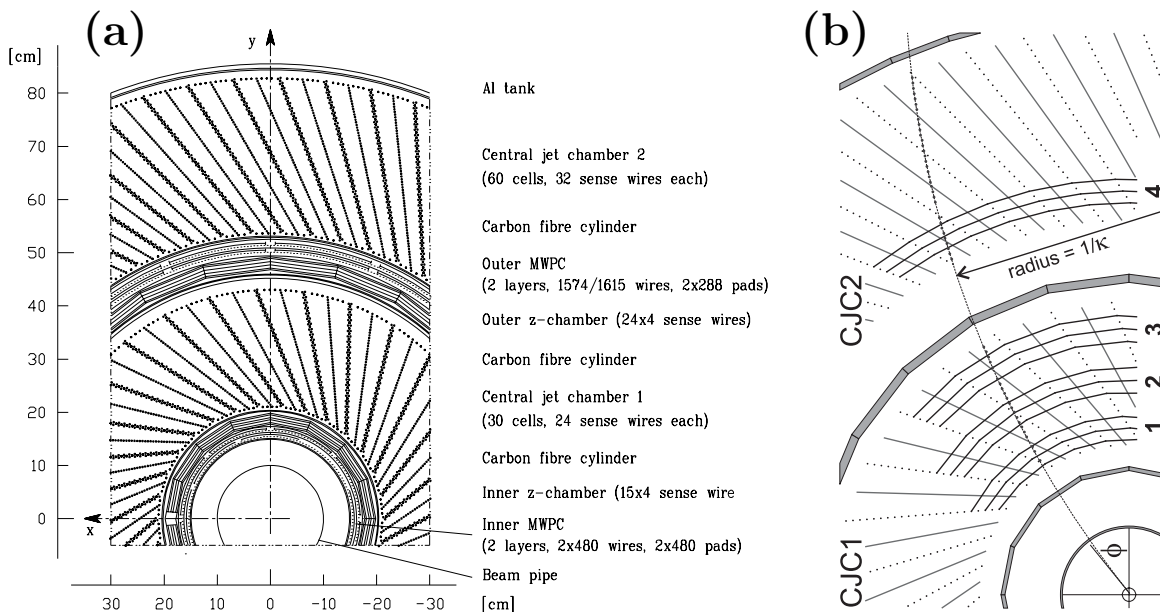


Figure 3.4: **a)** A schematic view of the H1 central tracker in the radial plane. **b)** Illustration of the track reconstruction in the central tracker.

Chamber	Inner radius (mm)	Outer radius (mm)	Number of cells	Sense wires per cell	Spatial resolution (μm)	Momentum resolution (GeV^{-1})
CJC1	203	451	30	24	~ 200	~ 0.01
CJC2	530	844	60	32	~ 200	~ 0.01

Table 3.2: CJC1 and CJC2 hardware and resolution parameters.

Central z -Chambers (CIZ,COZ)

The **C**entral **I**nter (CIZ) and **C**entral **O**uter (COZ) drift z -chambers measure the z coordinate of tracks in the central region. The CIZ is mounted inside CJC1 and the COZ between CJC1 and CJC2 (see Fig. 3.3, 3.4a). The polar angle coverage of the CIZ and COZ are $9^\circ < \Theta < 171^\circ$ and $25^\circ < \Theta < 155^\circ$, respectively. Each chamber

Condition	Value	Unit
Minimum transverse momentum p_t	0.1	GeV
Minimum, maximum polar angles $\Theta_{min}, \Theta_{max}$	20, 160	deg
Maximum distance of closest approach to vertex	2.0	cm
Maximum track starting distance from z axis	50.0	cm
Angle ϑ_{cut} for track length cut	150	deg
Minimum track length at $\Theta < \vartheta_{cut}, \Theta > \vartheta_{cut}$	10.0, 5.0	cm

Table 3.3: Track quality conditions in the CJC.

has four layers of sense wires which are strung in perpendicular direction to the beam axis. The reconstructed z coordinates in CIZ and COZ have spatial resolution about $300 \mu m$. The reconstruction of the interaction vertex is done by a combined fit of the hits in CJC1 and CJC2 with the measured z -coordinate from CIZ and COZ.

Central Proportional Chambers

The inner and outer cylindrical proportional chambers CIP and COP are mounted next to CIZ and COZ, respectively. They provide a fast z -vertex trigger in the central region with time resolution less than the bunch crossing time. Each chamber contains two layers of wires. There are 480 wires in each layer which are strung parallel to the beam axis. The CIP and COP cover the same polar angular range as CIZ and COZ.

3.4 Calorimetry

There are four calorimeters in the H1 apparatus:

- The Liquid Argon Calorimeter (LAR) is the major and biggest calorimeter of H1. It covers the whole central and forward region. It is used for registration of electromagnetic and hadronic showers to measure the deposited energy of charged particles and jets.
- The Spaghetti Calorimeter (SpaCal) surrounds the beam pipe in the backward region. It is mainly used for electron identification.
- The PLUG is a silicon sampling calorimeter placed in the forward region covering an approximate polar angle range of $0.3^\circ \lesssim \Theta \lesssim 3^\circ$. The PLUG fills the gap between the LAR forward segments and the beam pipe.
- The Forward Neutron Calorimeter (FNC) consists of scintillating fibers embedded in a lead matrix "spaghetti" to measure energy and angle of forward neutrons scattered in $e p \rightarrow e n X$.
- The Very Low Q^2 spectrometer (VLQ) was installed in the very backward region inside the iron yoke of the H1 detector to cover the transition region between the photoproduction and DIS decay modes in the range of $0.02 < Q^2 < 1 \text{ GeV}^2$.

Plug, FNC and VLQ are out of interest of this work because the scattered proton is measured in the FPS and scattered electron is not detected. The SpaCal and LAr calorimeters are used in the analysis in order to *VETO* non-photoproduction electrons.

LAr Calorimeter

The LAr Calorimeter consists of eight wheels as shown in figure 3.5c . The wheels consist of electromagnetic (EM) and hadronic (HA) sections but the most backward wheel (BBE) contains only an electromagnetic section. All “wheels” are placed in one cryogenic system. The integrated polar angle range of the LAr is $4^\circ \lesssim \Theta \lesssim 154^\circ$.

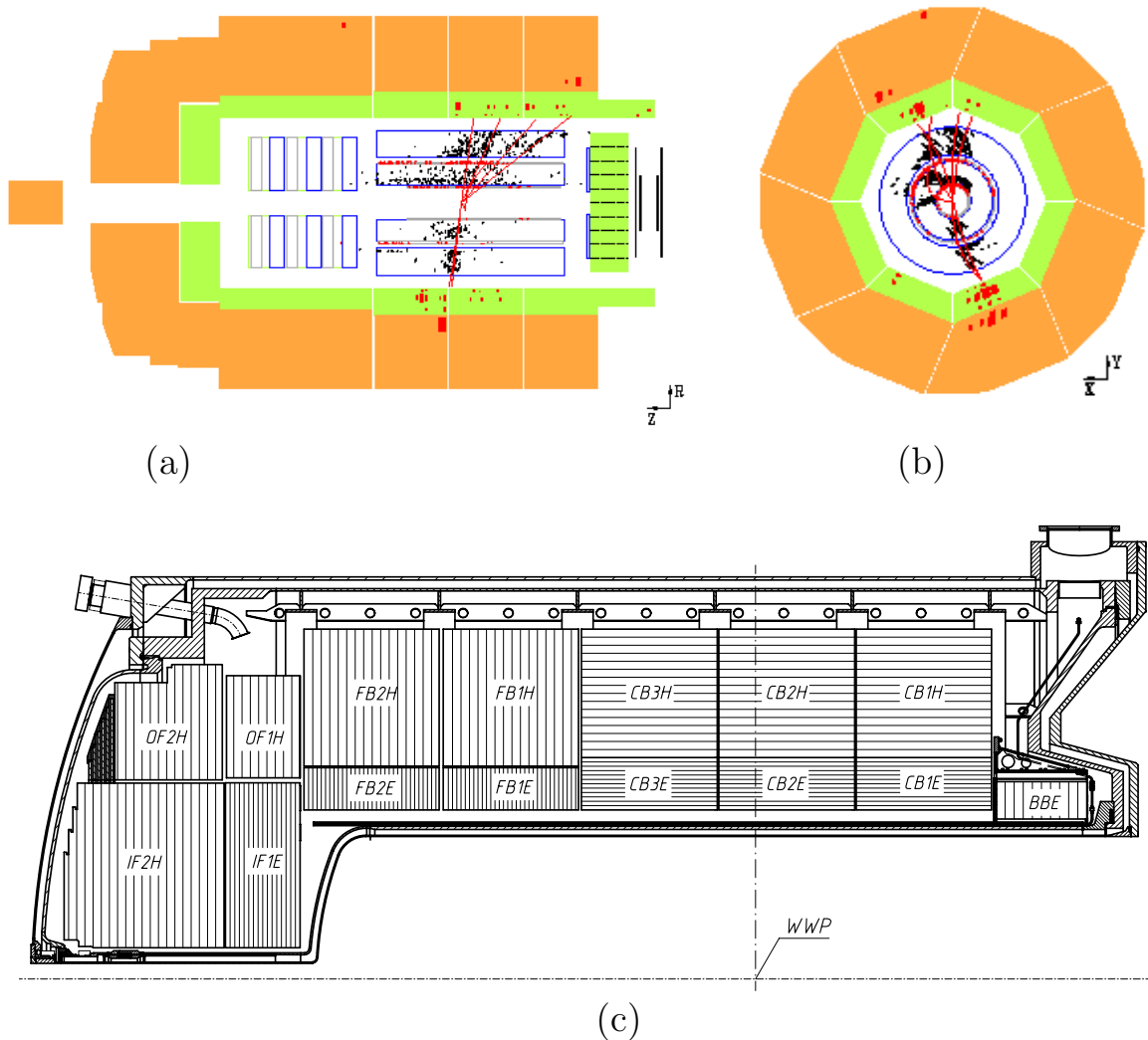


Figure 3.5: **a)** Schematic layout of the LAr big towers in the $r - z$ plane, together with the H1 tracking system, forward and backward calorimeters. **b)** Schematic layout of the LAr and central track chambers in the $r - \phi$ plane. Figures (a,b) show a high Q^2 event. **c)** Side view of LAr segments. WWP denotes the nominal interaction point.

Due to the asymmetry of the beam energies the calorimeter radiation thickness varies from the forward to the backward region. For the electromagnetic sections it decreases from 30 to 20 X_0 and for the hadronic sections from 7 to 5 λ_I , where X_0 is the radiation length and λ_I is the hadronic interaction length.

The energy resolution of measurement of the electrons in the electromagnetic sections is around $\sigma(E)/E \sim 0.12/\sqrt{E} \oplus 0.01$. The energy resolution of hadrons measured in the hadronic sections is $\sigma(E)/E \sim 0.55/\sqrt{E} \oplus 0.03$.

SpaCal

The SpaCal calorimeter uses scintillating fibers as active material. The absorption material is lead. The fibers are embedded into grooves of lead plates and placed in staggered order. The scintillating light from fibers is read out by photomultiplier tubes. The SpaCal, as one can see from figure 3.6a, consists of electromagnetic (EM) and hadronic (HA) calorimeters. The EM calorimeter is instrumented with 0.5 mm and the HA calorimeter with 1 mm diameter fibers.

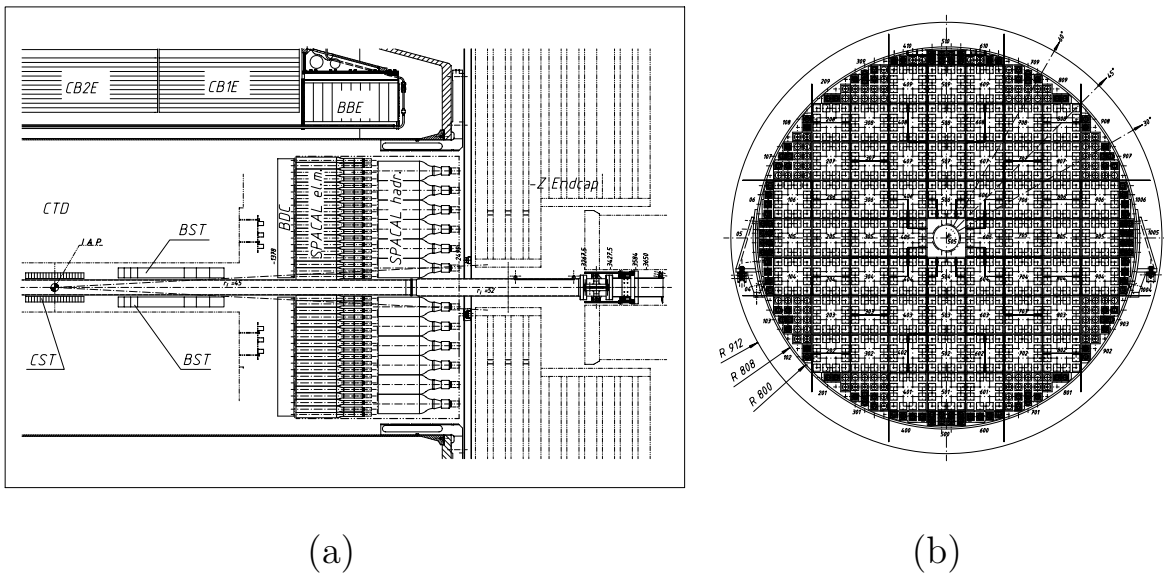


Figure 3.6: **a)** Side view of a part of the H1 backward region. The SpaCal electromagnetic and hadronic sections are placed in the center of the scheme. **b)** $r - \phi$ view of the SpaCal electromagnetic part.

The EM calorimeter contains 1192 cells of $40.5 \times 40.5 \text{ mm}^2$ square in the $r - \phi$ plane. The electromagnetic shower Molière radius in the SpaCal is $\sim 26 \text{ mm}$. The energy resolution of an EM block is $\sigma(E)/E = 0.07/\sqrt{E} \oplus 0.01$. The EM cells, surrounding the beam pipe have a specially adapted geometry as one can see in figure 3.6b. These cells contain an 8 mm VETO layer to estimate energy leakage into the beam pipe.

The HA calorimeter contains 136 cells of $119.3 \times 119.3 \text{ mm}^2$ size in the $r - \phi$ plane. It measures the electromagnetic shower leakage and the hadronic flow in backward region. The polar angle coverage of the SpaCal is $151.5^\circ < \Theta < 178.7^\circ$.

3.5 The Luminosity System

The H1 luminosity system serves for 1) luminosity measurement, 2) electron beam monitoring for HERA, 3) tagging of photoproduction events, 4) scattered electron energy measurement under small electron angles, 5) measurement of photons from initial state radiation.

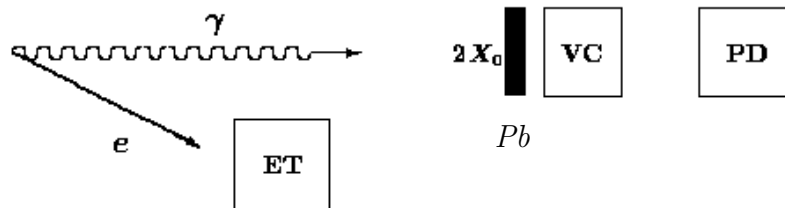


Figure 3.7: Scheme of the H1 luminosity measurement procedure.

The luminosity in H1 is measured by counting rates of the Bethe-Heitler bremsstrahlung process $ep \rightarrow e\gamma p$ [73] which has a well known cross section. The main background source to $ep \rightarrow e\gamma p$ is bremsstrahlung from the beam pipe residual gas: $eA \rightarrow e\gamma A$. To exclude background processes from the total rate of registered bremsstrahlung events (R_{tot}), the rates from electron pilot² bunches (R_{e0}) are used. The rate from the electron pilot bunch is weighted to the ratio of total and pilot electron beam currents and subtracted from the total rate of bremsstrahlung events:

$$\mathcal{L} = \frac{R_{BH}}{\sigma_{BH}} = \frac{R_{tot} - (I_{tot}/I_{e0})R_{e0}}{\sigma_{BH}} . \quad (3.1)$$

Here \mathcal{L} – is the luminosity; R_{BH} – the bremsstrahlung rate from $ep \rightarrow e\gamma p$; σ_{BH} – the cross section of the Bethe-Heitler process $ep \rightarrow e\gamma p$; R_{tot} – the total rate of bremsstrahlung from all sources in the ep interaction bunch; R_{e0} – the rate of bremsstrahlung from pilot electron bunch; I_{tot} – the electron beam current in ep interaction; I_{e0} – the pilot electron beam current.

The scattered electron and outgoing photons are measured in coincidence as shown schematically in figure 3.7. The H1 luminosity system consists of the following detectors:

- The electron calorimeters ET33 and ET44 are designed to tag scattered electrons with low Q^2 which are out of SpaCal acceptance. Two lead glass Čerenkov

²e-bunches without colliding p-bunches.

calorimeters are placed at $z = -33 \text{ m}$ and $z = -44 \text{ m}$ nearby the electron pipe (see Fig. 3.8 a,d). Each electron tagger contains 49 crystal cells covering $22 X_0$ in z direction. The acceptance of ET33 and ET44 is respectively $0.25 < y < 0.7$ and $0.04 < y < 0.24$, where y is the inelasticity defined in formulae 2.8, 2.9.

- The Photon Detector (PD) has the same design as ET33 and ET44 but contains only 25 cells as shown in figure 3.8b,c . The photons leave the proton beam pipe through a window at $z = -92.3 \text{ m}$ and hit the PD at $z = -103 \text{ m}$. A Pb filter and Čerenkov veto counter (VC) protects the PD from the high synchrotron radiation (see Fig. 3.8 b,d).
- A new spaghetti calorimeter (ET8) is installed as an electron tagging detector at $z = -8 \text{ m}$ nearby the electron pipe to extend the inelasticity range of the measured scattered electron.

The current luminosity is recorded every 10 sec during data taking. Then the luminosity is integrated run by run in the off-line procedure. The HV slow control and BBL3 alarm words allow to check the working abilities of interesting detectors for every 10 sec and correct the luminosity integration according to their status.

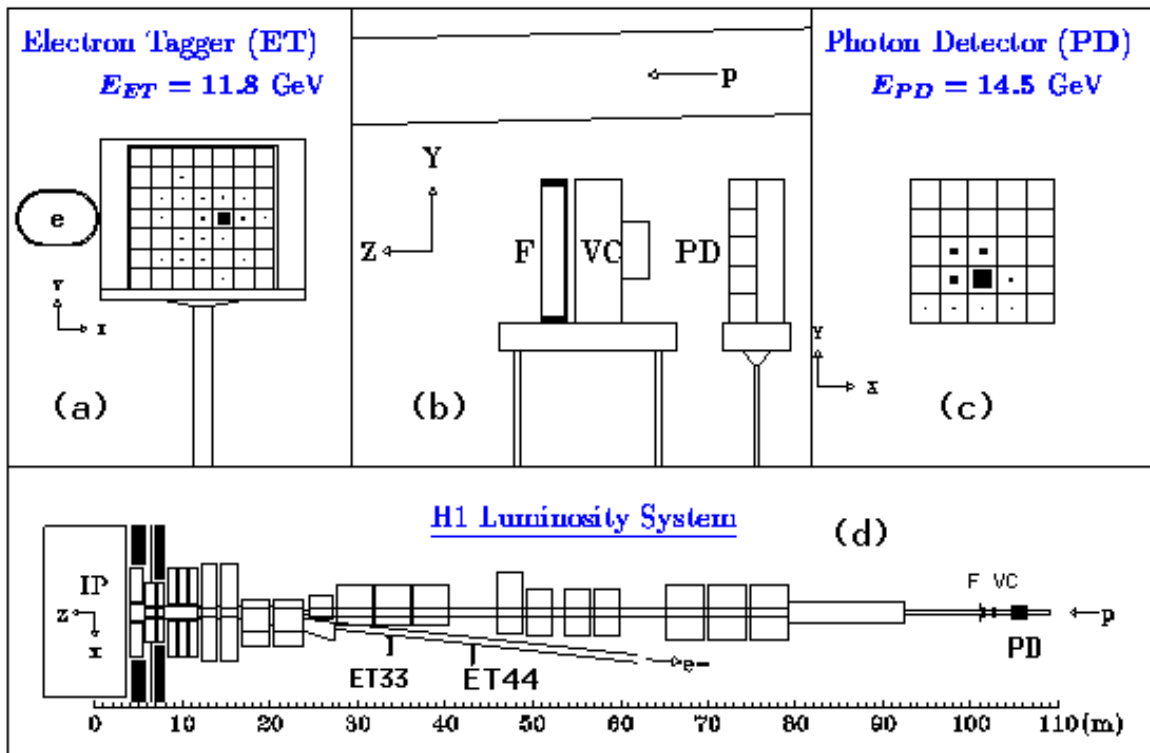


Figure 3.8: Schematic Event Display view of the H1 luminosity system.

3.6 Triggering System and Data Acquisition

The H1 triggering system is divided into four levels. The schematics of the trigger hierarchy as shown in figure 3.9 a is as follows:

1. The first level trigger (L1). The L1 trigger is synchronized to the HERA clock frequency of 10.4 MHz and provides a decision for each bunch crossing within $2.3 \mu\text{sec}$. The discriminated and synchronized signals from different detectors are stored during this time in a pipeline. For a coming positive trigger decision the *L1keep* signal stops the pipeline accumulation and the event and trigger information is read out into a next trigger level. Trigger bits named *Trigger Elements* are formed concerning the general properties of the event. Trigger Elements (TE) have an 8 bits array in memory, so that only 256 trigger units are available. All 256 units are used in trigger logic. In what follows trigger elements will be referred to their array index and termed as TE i , $i=0,\dots,255$. The data analyzed in the current work are collected with a trigger signal from the Forward Proton Spectrometer horizontal stations. The trigger bits occupied by the FPS horizontal stations and used in the current analysis correspond to the following Trigger Elements:

- 1) **TE 164** – the signal from 64 m horizontal station – FPS_64H ;
- 2) **TE 165** – the signal from 80 m horizontal station – FPS_80H .

Besides trigger elements the H1 triggering system contains 128 subtriggers – different combinations of trigger elements. To form a subtrigger signal the trigger elements are compared with a “*look-up table*” which contains subtrigger combinations. Every subtrigger serves for a certain experimental task. The L1 trigger sends all subtrigger hits in the pipeline.

To order data by their physical importance, some subtriggers get priority in comparison with others. That means the other subtriggers are suppressed at the electronic level by *subtrigger pre-scale factors*. The subtrigger pre-scale factors are fixed for a set of runs and can be changed for special purposes. Hence pre-scale factors for different subtriggers are run dependent and one has to apply pre-scale factors in the analysis to correct the event rate of subtriggers run by run. The L1 decision is then validated by the second level trigger.

2. The second level trigger (L2) is based on two independent techniques: neural network and topological algorithms. L2 requires $20 \mu\text{sec}$ leading to typical input rates of 1 kHz. L2 is not used in the current analysis.
3. The third level trigger (L3) is not being used. Events with a positive L2 signal are directly transferred to the *level four* trigger.
4. The level four (L4) is realized at the event readout stage by software filters using a computer farm. L4 is the last trigger stage of H1. It applies L1 subtriggers and L2 information for background rejection from beam gas, beam-wall and cosmic events. L4 performs event classification. In the current work the **CLASS 14** – which contains the events with leading protons is used.

The offline reconstruction stage can be announced as L5 level. At this stage reprocessing of raw data is done and selected events are written to Data Summary Tapes (DST).

The data acquisition system (DAQ) receives the signals from subdetectors and records them to one unit – Central Event Buffer (see Fig. 3.9 b). In order to decrease dead-time caused by the readout of data the DAQ tasks are divided to several classes.

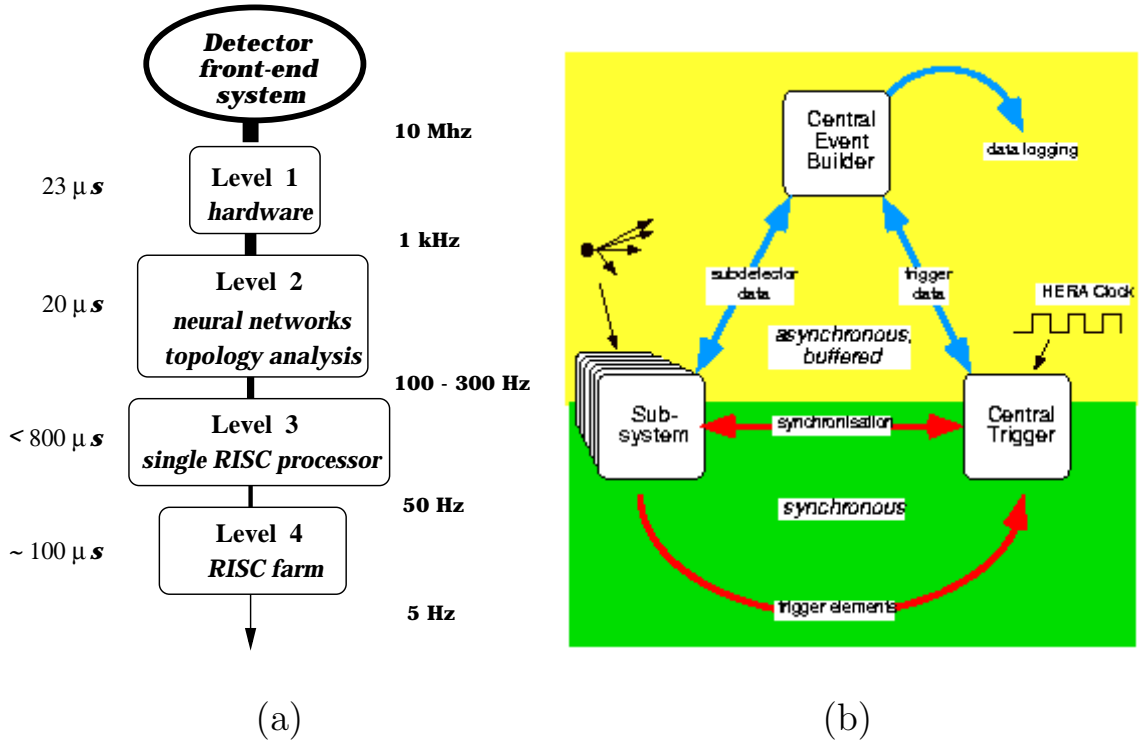


Figure 3.9: **a)** The H1 hierarchy of trigger levels. **b)** The DAQ flows.

3.6.1 The z -Vertex Trigger

The aim of the z -vertex trigger is the on-line identification of primary ep interactions around the nominal interaction point along the beam axis. The z coordinate of the interaction point is defined by signals of the CIP and COP in the central region. In addition signals from the FPC are included in the z -vertex trigger because of the high particle multiplicity in the forward direction.

The central tracker is subdivided into 16 segments each of which corresponds to the bit implemented into the z -vertex trigger logic. The track candidates in the central region are defined in each segment if there is a coincidence of hits in CIP and COP chambers. The hits are connected by a straight lines in the r - z plane for all possible combinations. Then all these track candidates are extrapolated to the z -axis ($r = 0$).

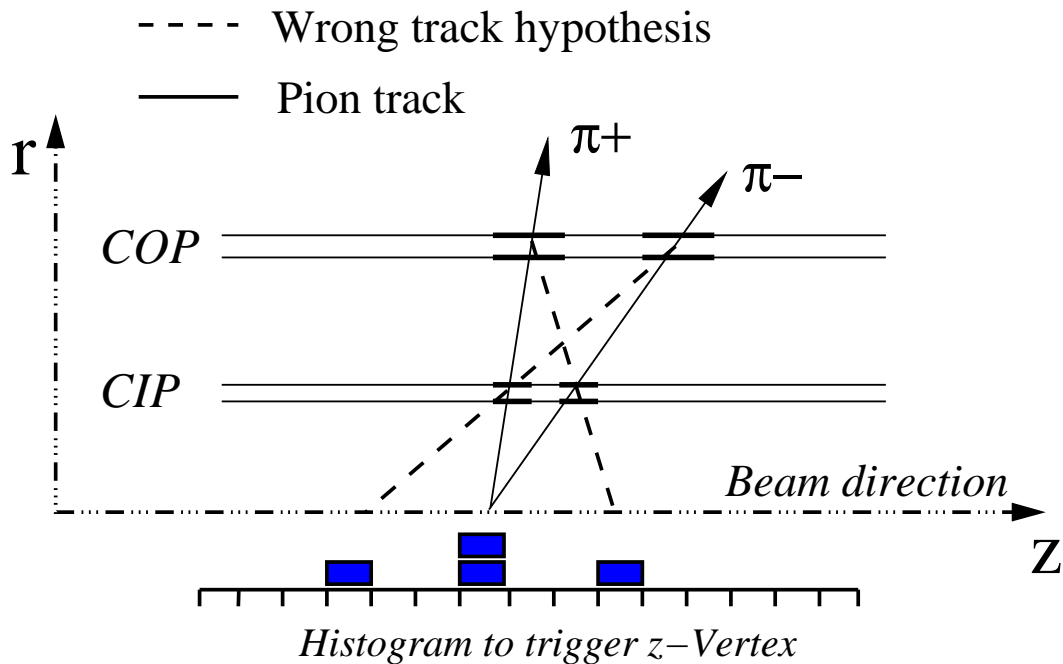


Figure 3.10: A schematic view of operation of the z -vertex trigger. The example of the ρ^0 decay pions detected in central region is shown.

The z -coordinates of all possible track candidates at $r = 0$ are filled in a histogram of 16 bins. The histogram is centered at the nominal interaction point and restricted to the z range of $-439 < z < 439$ mm. The width of each bin is ~ 55 mm. The bin with the largest number of track candidates is expected to be the ep interaction vertex in the current event. The z -vertex histogram is used to form several trigger bits. In the current analysis the following two of them are used. **1)** The `zVtx_T0` bit (TE 24) has a positive decision in case of a non-empty histogram. This is the most soft condition which indicates an activity in the central tracking system. **2)** The `zVtx_Cls` bit (TE 29) has a positive decision whenever the histogram is filled in four neighbouring bins. A positive decision of `zVtx_Cls` always includes a positive decision of `zVtx_T0`.

3.6.2 The Drift Chamber r - ϕ Trigger

The $DCR\phi$ trigger is based on charged tracks in the H1 central region. The $DCR\phi$ trigger requires at least ten active layers in the CJC: seven active layers in CJC1 and three active layers in CJC2 as shown in figure 3.4b. A track in the r - ϕ plane has a circular trajectory and is characterized by three parameters: 1) the track curvature in the solenoidal magnetic field; 2) the distance of closest approach (DCA)³; 3) the azimuthal angle ϕ in the DCA point (see Fig. 3.4).

³DCA is the closest point of the track circle to the centre of the H1 coordinate system

The $DCR\phi$ trigger accepts tracks with a minimum p_t value of 0.1 GeV . The $DCR\phi$ trigger occupies eight bits: TE 16 – TE 23. In the current analysis TE 17, named *DCRPh-Ta*, is used for the track candidates of the ρ^0 decay pions. *DCRPh-Ta* requires at least one track to be found.

3.7 H1 Software Packages

H1 software is written in standard FORTRAN77. The main H1 software packages are:

1. **BOS** – **B**ank **O**peration **S**ystem. BOS is a program system which performs the dynamic management of memory and data sets. The system supports a modular structure of the application program and portability of both the software and the data sets. All data sets of H1 are written in BOS banks.
2. **FPACK** – is a general package for a machine-independent input/output of data.
3. **LOOK** – is the H1 graphics and analysis system. Most of the H1 control histograms are performed by LOOK in analysis FORTRAN codes. The basic graphical operations are performed by **GKS**.
4. **H1ED** – is the H1 Event Display. H1ED is based on the LOOK graphics system, using BOS for memory management, FPACK for input/output and GKS for graphics. The program contains drawings of all the H1 components in different views and realize visual observation of events in them for real data and Monte-Carlo.
5. **H1GEN** – the H1 interface to the event generators. There is a rather wide set of generators used in the H1 experiment. Here only the two generators used in current work are mentioned. These are DIFFVM and PHOJET (see Sec. 2.6).
6. **H1SIM** – the H1 SIMulation program. It was created within the GEANT [78] framework. The H1SIM reads *generated* events and produces *simulated* events. The H1SIM response corresponds to the online response of the H1 detector.
7. **H1REC** – the H1 REConstruction package which contains the basic information about the tracks, calorimeter clusters, efficiencies, noise, deterioration e.t.c.
8. **H1PHAN** – PHysics ANalysis package is a set of tools to provide standard H1 physics analysis information linked to H1GEN, H1SIM and H1REC.

Chapter 4

Forward Proton Spectrometer

In this chapter the *horizontal stations* of the Forward Proton Spectrometer (FPS) [74] are described. The FPS components, maintenance, registration principles, and measurement procedure are presented here in detail. The FPS horizontal stations are used in the current work both as triggering and reconstruction stages. The FPS is a remote part of the H1 detector which extends the acceptance of the apparatus in the very forward region. The *horizontal stations* provide a direct measurement of the leading proton momentum in the kinematic range of the fractional momentum $E'_p/E_p > 0.95$.

4.1 FPS in the Forward Proton Beam Line

The FPS was added to the H1 detector¹ to measure the forward protons from ep interactions [76]. The bulk of processes with a forward proton measured in the FPS horizontal stations are diffractive² processes. The protons scattered at very small angles escape the main H1 apparatus and gallop over the beam pipe. The aim of the FPS is to tag these forward protons and to measure their momenta. The FPS is a tracking detector. Its measurement principle is that of a magnetic spectrometer. The magnetic field for the FPS is provided by the HERA beam line magnets. The shape of the *proton beam envelope* along the proton beam from the interaction point up to the FPS stations is a function of the HERA magneto-optics (see Fig. 4.1). The FPS is attached to the proton beam tube at distances between 60 m and 90 m from the interaction point.

There are two types of the FPS at the H1 experiment. They are termed *vertical* and *horizontal* stations. For each type two identical stations exist. The FPS stations are termed by the direction of their attachment in the x - y plane perpendicular to the beam direction. The *vertical stations* are inserted into the proton pipe from above i.e. along the y projection. The *horizontal stations* are inserted into the proton pipe from

¹In the ZEUS detector [75] the Leading Proton Spectrometer (LPS) similar to the H1 FPS is used.

²Deep inelastic processes with a leading proton in the final state are also measured by the FPS, but were not analyzed in this analysis.

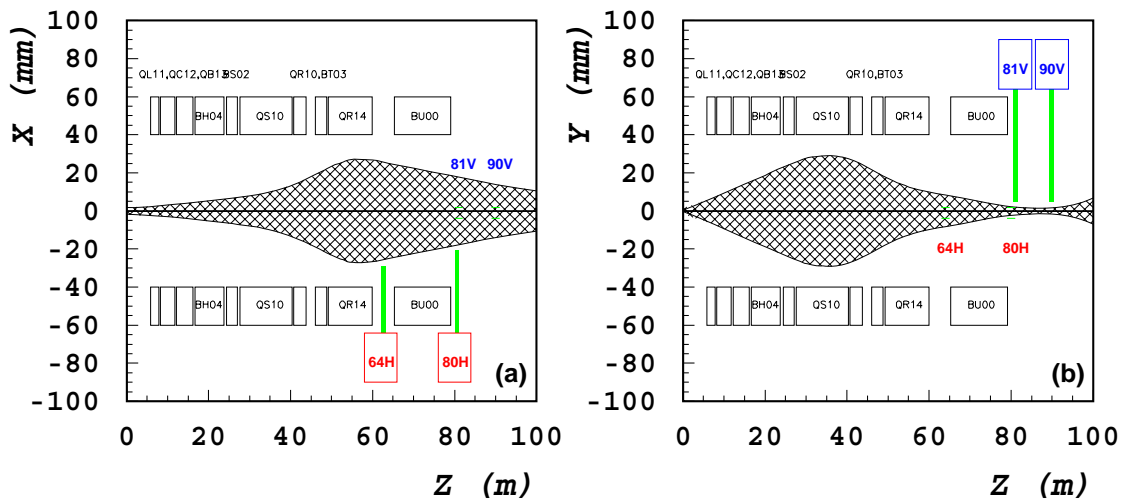


Figure 4.1: Schematic view of the proton beam shape and the FPS position along the beam pipe. **a)** x projection; **b)** y projection.

Kinematic variable	Vertical stations	Horizontal stations
Fractional momentum	$0.7 < E'_p/E_p < 0.9$	$0.95 < E'_p/E_p$
Square of e 4-momentum	$2 < Q^2 < 50 \text{ GeV}^2$	$Q^2 < 50 \text{ GeV}^2$
CME of γp system	$40 < W < 260 \text{ GeV}$	$20 < W < 100 \text{ GeV}$
IP fractional momentum	$0.1 < x_{\mathbb{P}} < 0.3$	$x_{\mathbb{P}} < 0.05$

Table 4.1: Kinematic ranges covered by the FPS vertical and horizontal stations.

aside i.e. along the x projection. The orientation of the vertical and horizontal stations with respect to the proton pipe is presented in figure 4.2.

The vertical and horizontal stations cover different kinematic regions of the leading protons, provide different trigger decisions and serve for different physical tasks. A schematic view of the vertical and horizontal FPS stations is shown in figure 4.2. The kinematic ranges are presented in table 4.1. The horizontal stations are placed at 80 m and 64 m, before and after the BU00 dipole magnet (see Fig. 4.1a). The vertical stations [76, 77] are placed at 81 m and 90 m behind the BU00 magnet (see Fig. 4.1b). The BU00 magnet bends the proton beam 5.7 mrad upwards.

The current work is concentrated on the measurement of the elastic ρ^0 -meson photoproduction with the scattered proton detected in the FPS horizontal stations. The scattered protons which are separated by the HERA magnets from the circulating proton beam have a typical offset of few millimeters from the proton beam. The width of the proton beam envelope in terms of standard deviations of a Gaussian fit to the beam profile in the x and y projections at the positions of both horizontal stations are:

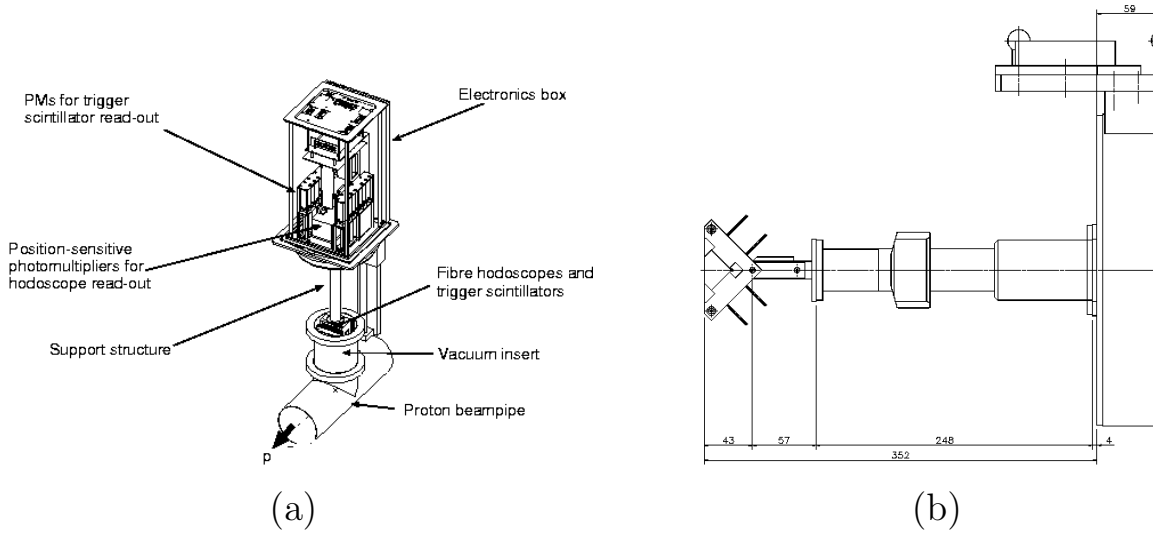


Figure 4.2: *Schematic view of the FPS mechanics: a) vertical station, b) horizontal station.*

$$\begin{aligned} \sigma_x(80H) &= 1.88 \text{ mm} , & \sigma_y(80H) &= 0.27 \text{ mm}; \\ \sigma_x(64H) &= 2.51 \text{ mm} , & \sigma_y(64H) &= 0.84 \text{ mm}. \end{aligned}$$

Here and further the horizontal stations are denoted by their distance of 80 m and 64 m from the nominal $e p$ interaction point: **80H** and **64H**, correspondingly.

4.2 Components of the Horizontal Stations

The FPS detector consists of the following elements: **1)** the active detector material: a) plastic scintillators, b) scintillating and light guide fibers; **2)** photomultipliers and readout electronics; **3)** mechanical framework: a) plunger vessel, b) driving system, c) position measurement device.

Fiber Modules and Trigger Tiles

Each station contains two subdetectors shifted to each other by 60 mm along the z -axis as shown in Fig. 4.3a. Each subdetector contains two *sets* of scintillating fibers. The sets are inclined by $\pm 45^\circ$ in the x - y plane with respect to the x -axis. The projections along the inclined sets are termed U and V . The $U - V$ plane has perpendicular orientation to the beam axis. The inclination of $\pm 45^\circ$ allows to avoid a too strong fiber bending in the narrow *plunger vessel*. The scintillating fibers are connected to *multi-channel photomultipliers* by light guide fibers.

Each fiber plane consists of five fiber layers disposed along the proton beam direction. Each layer consists of 24 fibers. The fiber diameter is 1 mm. The fiber pitch inside

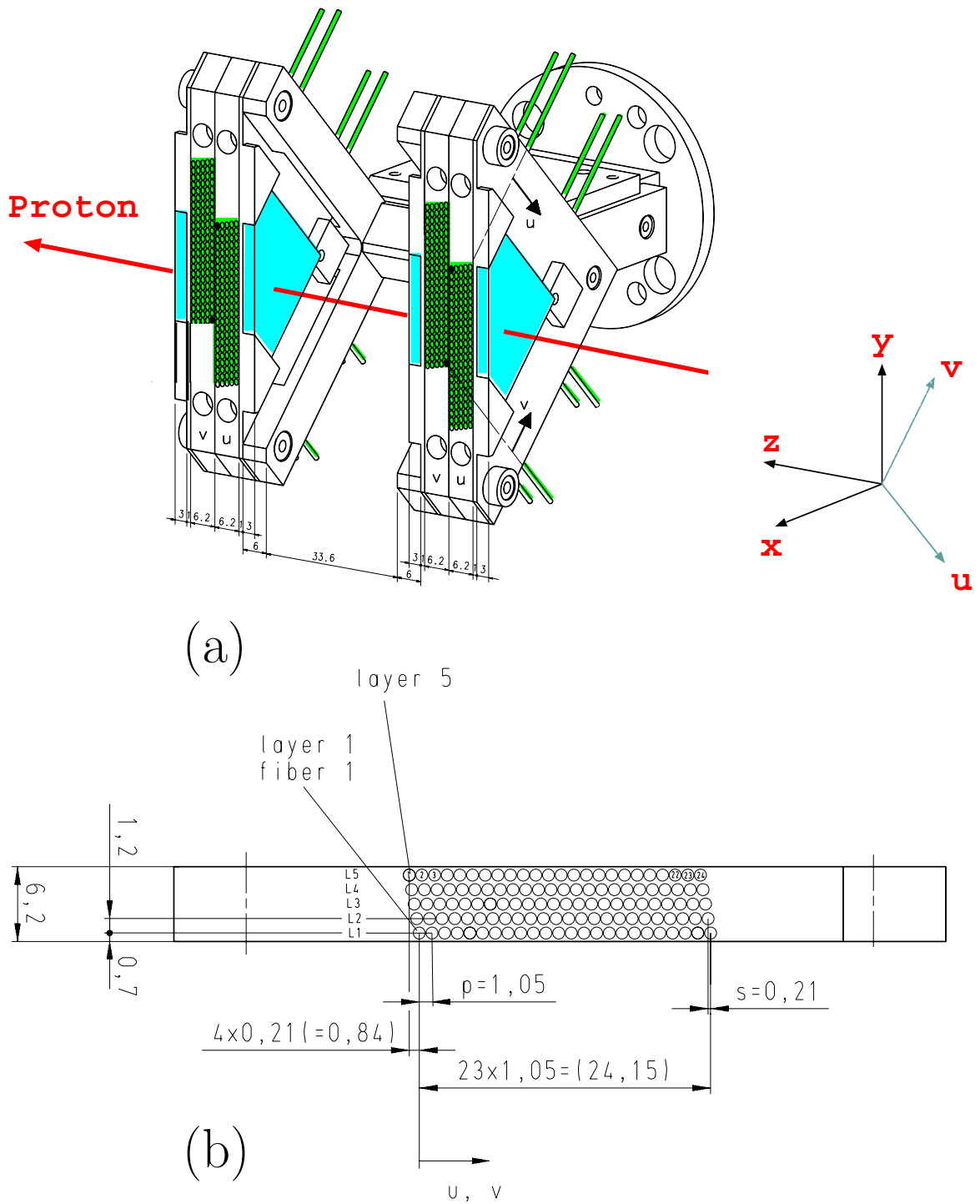


Figure 4.3: **a)** Three dimensional view of a FPS horizontal station. The distance between the subdetectors is about 60 mm in beam direction. **b)** View of the fiber detector end face. The five fiber layers are staggered by 0.21 mm.

each layer is 1.05 mm . In order to obtain better spatial resolution the neighboring fiber layers are staggered by 0.21 mm (see Fig. 4.3b).

Each subdetector is covered by plastic scintillation counters termed *trigger tiles*. The trigger tiles are placed before and behind the fiber planes as shown in figure 4.3a. They are 3 mm thick. The tiles copy the shape of the fiducial volume of the fiber detector. The readout of the trigger tiles is provided by *light guide fibers bundles* which are mounted at two sides of the tile and connected to one-channel photomultipliers.

Mechanics

The mechanical framework consists of three components:

- 1) the plunger vessel which provides mechanical support of the fiber detectors;
- 2) driving system, which moves the stations with respect to the proton beam;
- 3) measuring device which gives precise FPS distances with respect to the nominal beam axis.

The plunger vessel is a cylinder of 3 mm stainless steel. It is movable due to the flexible connection to the proton pipe via steel bellows. During the measurement the detectors are moved to their working positions close to the proton beam (inside the proton pipe). In case of high proton rates the driving system provides a fast retraction of the FPS stations to the parking positions far from the beam. Each station has a separate hydraulic driving system. The range for detectors movement is about 35 mm . Each FPS station is equipped by a Heidenhain³ measuring device (HDN). The actual detector position values measured by the HDN are read out every second by a slow control system. The actual HDN values are written to the data base. The mean precision of the HDN position values is about $10\text{ }\mu\text{m}$.

Photomultipliers and Electronics

For the fiber readout position-sensitive photomultipliers (PSPM) of serial type MCPM-124⁴ are used. The MCPM-124 has 124 channels performed by a corresponding anode pixel grid [74]. The MCPM-124 is a electro-static focused device with an anti-distortion electrode implemented between the photocathode and the first micro-channel plate. The photocathode quantum efficiency for the light spectrum of the fibers is 15%. Two micro-channel plates provide a gain of 3×10^5 at the voltage of 2.8 kV and total pulse time of 2.5 nsec .

The *anode pixels* have a size of $1.5 \times 1.5\text{ mm}^2$ and a pitch of 2.2 mm . The distance of 0.7 mm between anode pixels and the anti-distortion electrode reduce the *cross-talk* of the read-out signals from neighboring *anode pixels*. The average cross-talk of the MCPM-124 pixels is 1–2%. However a significant contribution of the electronic noise

³Messtaster Metro MT60, Dr.J.Heidenhain GmbH

⁴MELZ, Moscow, Russia.

may increase the cross-talk to the level of 10 %. To suppress the cross-talk the fiber-to-PSPM-pixel mapping is organized in a such a way that neighboring fibers are not coupled to neighboring PSPM pixels. Each PSPM has two reference pixels coupled via the light guide fibers to light emitting diodes (LED). The LEDs serve for monitoring and testing purposes.

Light guide fiber bundles transmit the scintillation light from the trigger tiles to the photomultiplier (PMT) of serial type R5600⁵. This PMT has a photocathode quantum efficiency of 20%, a gain of 10^6 at a voltage of 0.8 kV and pulse time of 0.65 nsec.

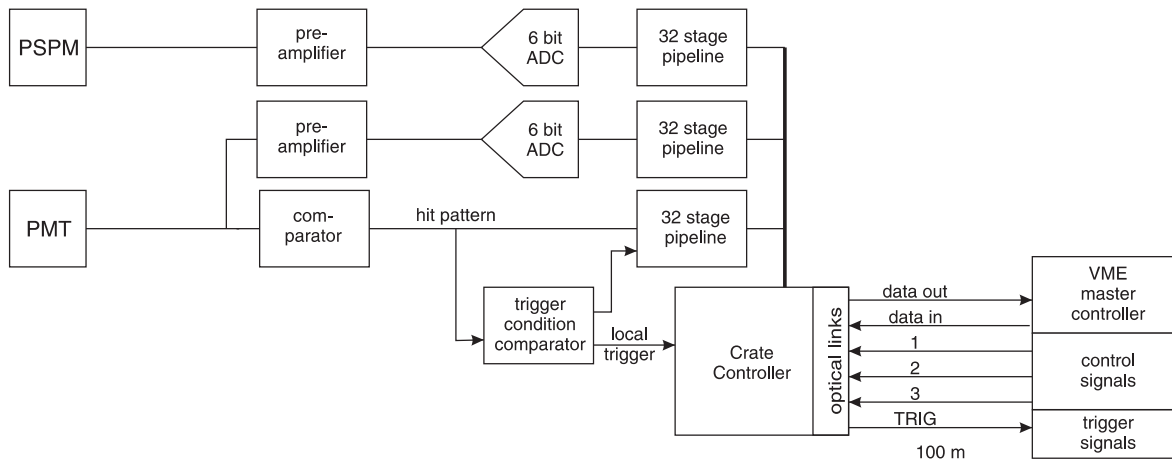


Figure 4.4: *The blockscheme of the FPS electronics. PSPMs, PMTs, preamplifiers and comparators are located inside the pot housing. ADC modules, trigger cards (TDC), pipelining modules and crate controller are mounted at the tunnel wall. Optical fibers provide signal transmission to the VME crates which are located outside of the tunnel in the experimental hall area.*

Signals from the photomultipliers are received by the FPS electronics which is subdivided into the three parts: **1)** The electronic box which is mounted at the plunger vessel close to the fiber detectors. It contains preamplifiers for the PSPMs and PMTs, PMT comparators and the reference LED modules. **2)** The ADC modules, trigger cards and pipelining electronics conjuncted to the common crate controller were mounted at the tunnel wall next to the FPS stations. **3)** The voltage supply and readout system.

The readout system is implemented in VME standard with optical connection to the crate controller. It is placed outside of the HERA tunnel in the experimental hall area.

⁵HAMAMATSU PHOTONICS, Japan.

4.3 Detector Position Measurement

Survey

The FPS position in the HERA tunnel is determined by a three-dimensional survey measurement which consists of two steps: **1)** geodesic measurements of the *mark-balls* MK1, MK2, MK3, MK4 as shown in figure 4.5; **2)** measurement of the eight *bench-marks* positions placed in the edge-holes of the subdetector frame (see Fig. 4.3). The mark-balls mounted on the steel plate are located on top of the FPS station. The bench-marks are placed on the stations end face, at both sides of each fiber set as shown in figure 4.6.

The geodesic survey measurement was done twice after the FPS exposition and before data taking. The mean precision of the mark-balls geodesic measurement is $100 \mu\text{m}$. The mean precision of the bench-marks position measurement is $20 \mu\text{m}$. The measured distances and relative tilts of the nominal beam axis to the mark-balls and bench-marks are used in the track reconstruction procedure.

Detector Position and Movement

The detector position gives the distance from the nominal proton beam axis to the lower edge of the FPS detector inside the proton beam pipe. This distance termed *detector position* is one of the most crucial values for data analysis with the FPS. The importance of the detector position is caused by two reasons: **1)** the FPS acceptance is very sensitive to the detector position; **2)** the accuracy of the detector position determines the accuracy of the measured proton track parameters which contributes to the error of the measured proton momentum.

As already mentioned above the FPS stations are movable detectors. During the data taking they are moved close to the circulating proton beam. In case of proton beam spikes of the HERA machine high rates of charged particles pass the FPS stations and the fiber detectors are retracted automatically to save the photomultipliers and fibers from radiation damage. The PSPMs based on micro-channel plates are very sensitive to high radiation rates.

When the proton beam quality is fine and correspondingly the radiation level low, the FPS detectors are moved again to the working positions. These working positions differ for different proton fills and each FPS station has a distribution of positions for every data taking period. The changes of the FPS position treated by the slow control procedure are written to the data base. The position values of both horizontal detectors are presented in figure 4.7. The distributions of figure 4.7 show the detector movement dynamics for the analyzed data and the corresponding simulation. The 80 m horizontal station is located about 10 mm closer to the beam than the 64 m horizontal station. This is related to the proton beam width at different distances to the interaction point as schematically shown in Fig. 4.1.

In figure 4.7 the detector positions after the calibration with respect to the real proton beam are presented. The calibration procedure is discussed in section 4.6.

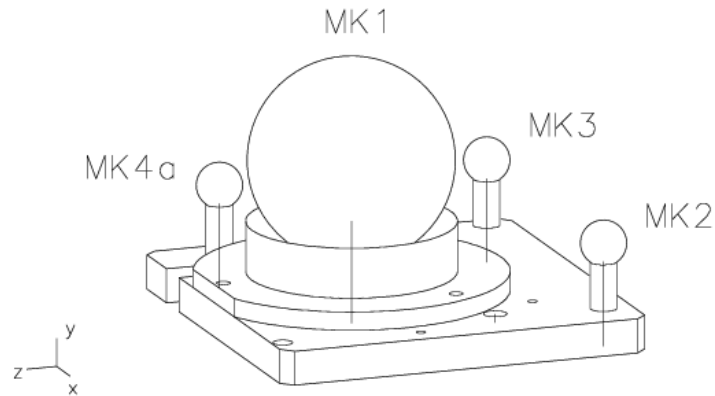


Figure 4.5: The mark-balls MK1, MK2, MK3, MK4 are placed at the top of the station frame. They serve as reference points to define spatial inclinations of the FPS frame and its distance from the nominal beam axis.

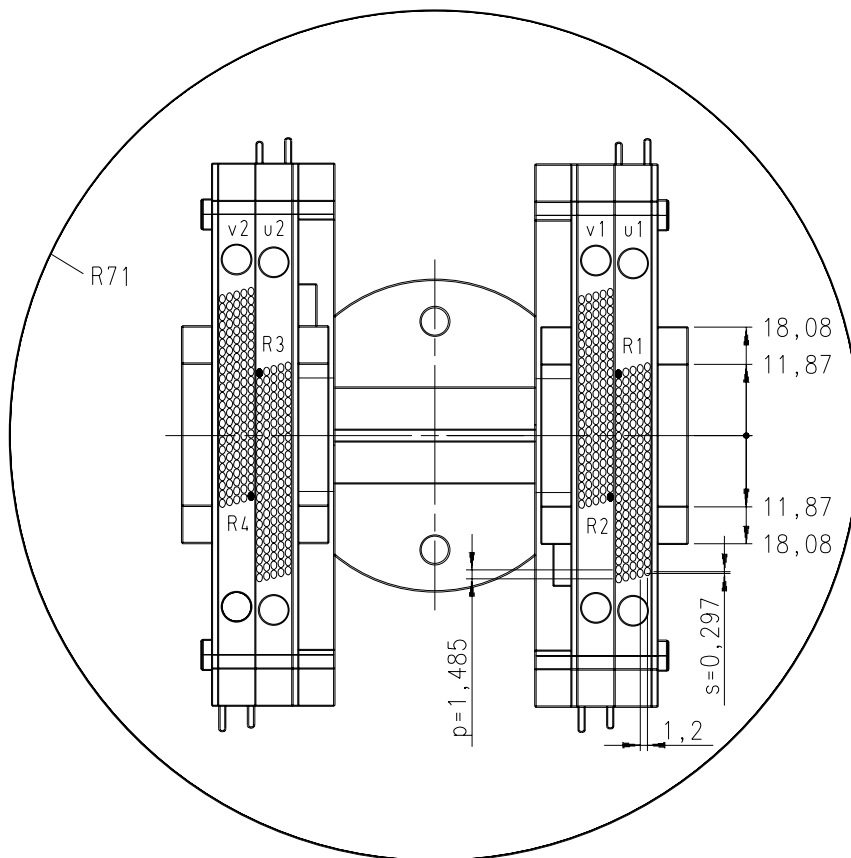


Figure 4.6: Side view at the FPS horizontal station in the z - y plane. The bench-marks for the survey measurement are visible as open circles in distances of several millimeters from the edges of the fiber sets.

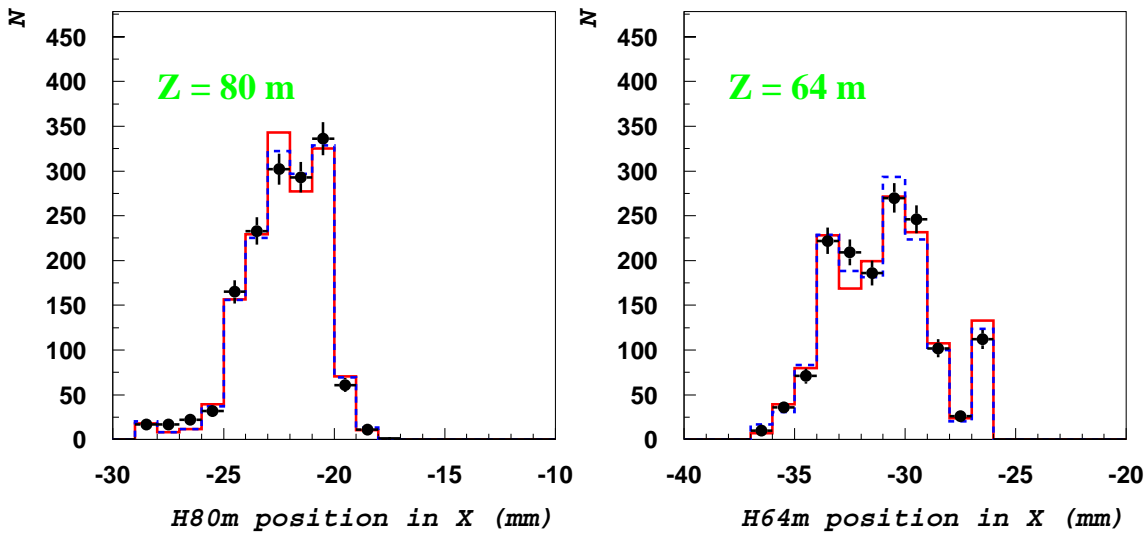


Figure 4.7: The distances of both horizontal stations from the real proton beam. **a)** the 80 m horizontal station; **b)** the 64 m horizontal station. Filled dots denote the FPS positions measured in data, solid and dashed line histograms denote the detector positions of MC events simulated by the generators PHOJET [62] and DIFFVM [61], respectively.

Simulation of the Detector Positions

The simulation of the FPS is implemented into the H1 simulation package H1SIM. The set of the FPS simulation modules written in standard FORTRAN 77 contains the following stages: **1)** The detector maintenance module – describes the detector geometry and materials definition – written using the GEANT [78] skeleton. **2)** The *digitization* module – simulates the detector response – fiber hits and clusters. The reconstruction efficiencies and measuring ability values are applied from data. **3)** The triggering module – simulates the trigger decision. The trigger tiles response is simulated using the triggering ability from data.

The detector position simulation was done beyond H1SIM. In order to determine the detector positions properly in the simulation the following two steps are applied:

I) The detector position is fixed in GEANT at the most close distance to the proton beam axis. The value of the closest distance is determined from data. The simulation is done at this fixed position.

II) The determination of the simulated detector positions is done at reconstruction stage (H1REC package). During the reconstruction of the simulated events the procedure which sets the new detector edge value is applied event by event (see Fig 4.8). If the track is out of the new edge, then this track is canceled. Otherwise the simulated event is accepted for further reconstruction. The new detector edge value is simulated event by event according to the detector positions measured in data.

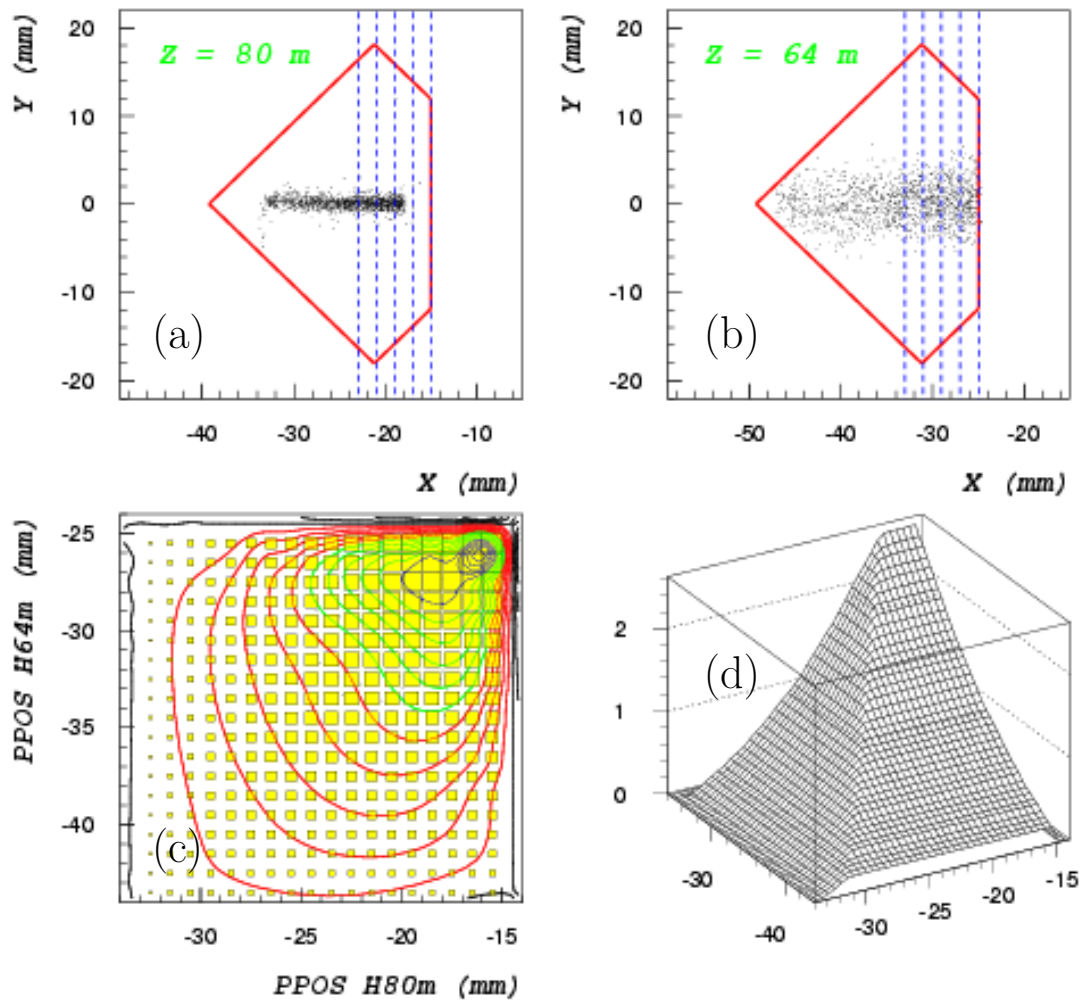


Figure 4.8: Track points **a)** in the 80 m horizontal station and **b)** in the 64 m horizontal station. Dashed lines mark possible detector positions according to the spectra shown in figure 4.7. Plots **c,d)** show the FPS acceptance as a function of both horizontal detector positions.

4.4 Proton Track Candidates

Reconstruction of the scattered proton track in the FPS [79] consists of the following stages:

- Cluster identification. A cluster is a group of neighboring fiber hits. To separate hits of the track from noise and background the cross-talk effect has to be suppressed. This is performed by a filtering algorithm which is applied to the fiber signal amplitudes A_i . The filtering algorithm transforms the channel amplitudes and provides a threshold decision after the transformation steps combined in equation 4.1: **i)** sum the amplitudes of the *direct* (j) and *diagonal* (k) neighboring pixels, **ii)** reweights this sum by coefficients which are optimized in methodical investigations, **iii)** subtract the reweighted sum from the measured amplitude.

$$\mathfrak{A}_i = 1.025 \cdot \left(A_i - 0.15 \sum_j A_j - 0.10 \sum_k A_k \right) . \quad (4.1)$$

The transformed amplitudes \mathfrak{A}_i are compared with the threshold value optimized in methodical investigations. The fiber hits with \mathfrak{A}_i above the threshold are accepted for clustering (see Ref. [79]). Each cluster contains at least two hits from the fibers of different layers.

- Local track reconstruction. A *local track* is a track inside one FPS station. The local track connects clusters of both subdetectors (see Fig. 4.3a, 4.9b,c) within the *tilt* threshold of 25 mrad . The reconstructed events may result with a high multiplicity of track candidates. To avoid the reconstruction of noisy events selection criteria listed in table 4.2 are applied in the current analysis.

An example of a reconstructed event as it looks in the H1 event display is presented in figure 4.9b,c for the 80 m and 64 m FPS horizontal stations, respectively. The fiber hits and local tracks strung between selected clusters inside the stations are schematically shown in the U-V planes.

Track definition criterion	Value
Minimum number of hits for a track fit	4
Maximum number of hits not used in a cluster	10
Minimum number of hit layers for a cluster	2
Maximum allowed angle for a track [mrad]	25
Maximum number of clusters per subdetector	5
Maximum number of projections per coordinate	4

Table 4.2: Local track selection criteria used in the current analysis.

- Global track reconstruction. A *Global track* is a track reconstructed between two FPS stations i.e. the local tracks in both stations are combined into one global track. In case of several local track candidates there are several reconstructed global track candidates and the reconstruction produce chose the global track candidate with the lowest χ^2 -value. The χ^2 of the global track is the sum of the calculated χ^2 -values of the local tracks. The global track parameters are calculated for one spatial point. This point is fixed as the approximate middle position between both horizontal stations at the distance of 72 m from the $e p$ interaction vertex.

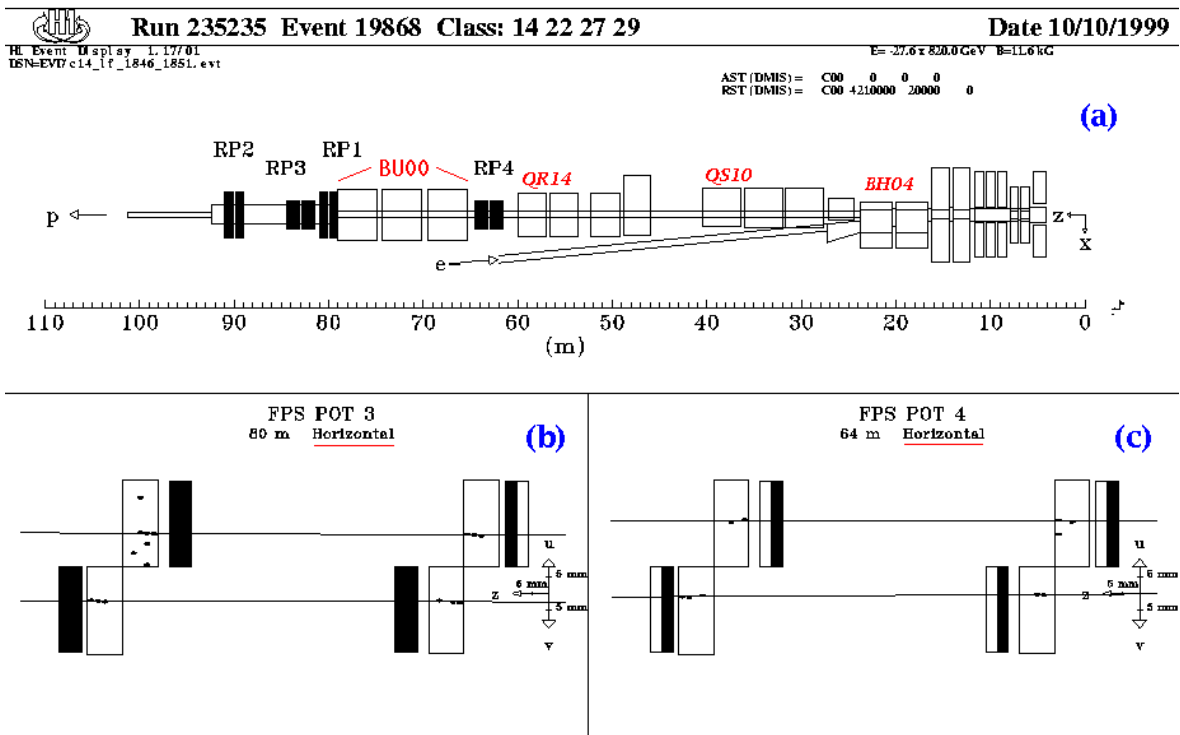


Figure 4.9: *Event display view at FPS detectors: a) forward beam line with HERA magnets and all four FPS stations. The horizontal stations are named RP4 and RP3. b,c) Fiber and trigger tile hits and the fitted track candidates in the U-V projections for the 80 m and 64 m horizontal stations, respectively.*

The scatter plots of the local tracks in x - y projection are shown in figure 4.10. The dashed line contours the fiducial volume of the fiber detectors at the approximate range of detector positions (histogrammed in Fig. 4.7).

The focusing effect in the proton beam magnetic system can be seen comparing the width of the 80 m and 64 m distributions shown in figure 4.10.

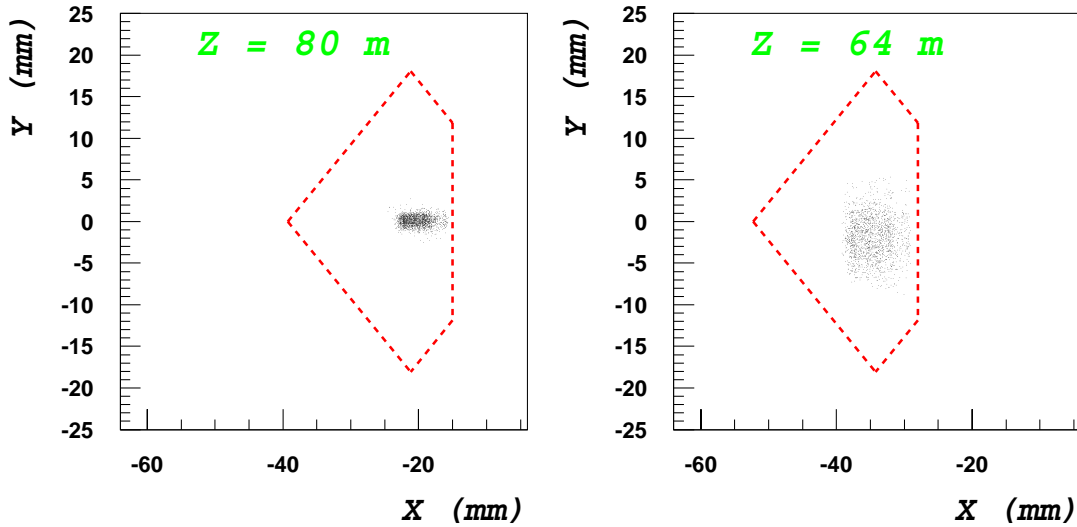


Figure 4.10: *Local tracks in x-y projection for 80 m and 64 m horizontal stations. The dashed lines contours schematically the fiducial volume of the fiber detectors. The distribution at 64 m is more wide than at 80 m caused by influence of the beam optics.*

4.5 Momentum Reconstruction

The scattered proton momentum measurement in the FPS is based on the optical properties [80] of the proton beam optics at HERA.

Transition from Track Parameters to Momentum

Using the focal and dispersion properties of the magnetic system one can reconstruct the energy (E'_p) and the polar angle (Θ_p) of the scattered proton from the measured track parameters [79, 81]:

$$\begin{aligned} \begin{pmatrix} X(z_f) \\ X'(z_f) \end{pmatrix} &= \begin{pmatrix} a_x(E_p) \\ c_x(E_p) \end{pmatrix} + \Theta_x \cdot \begin{pmatrix} b_x(E_p) \\ d_x(E_p) \end{pmatrix} , \\ \begin{pmatrix} Y(z_f) \\ Y'(z_f) \end{pmatrix} &= \begin{pmatrix} a_y(E_p) \\ c_y(E_p) \end{pmatrix} + \Theta_y \cdot \begin{pmatrix} b_y(E_p) \\ d_y(E_p) \end{pmatrix} . \end{aligned} \quad (4.2)$$

Here (X, X') and (Y, Y') – are the intercepts and slopes in x - z and y - z planes, correspondingly at the distance of $z_f = 72$ m from the interaction vertex. As mentioned above the spatial point of $z_f = 72$ m is selected for global track coordinate definition. The angles Θ_x and Θ_y are the projections of the proton's polar scattering angle at the interaction point, E_p is the reconstructed energy of the scattered proton. The

optical constants a, b, c, d describe the magneto-optical properties of the forward proton beam line. They are calculated by Monte Carlo method. Due to the magnetic system properties discussed above the optical constants of x - and y -projections are independent from each other.

Thus there are two independent solutions:

$$1) \quad (X, X') \xrightarrow{a_x, b_x, c_x, d_x} (E_x, \Theta_x) \quad ; \quad 2) \quad (Y, Y') \xrightarrow{a_y, b_y, c_y, d_y} (E_y, \Theta_y) \quad .$$

The equations 4.2 can be rewritten to express the slope through the intercept of the global track and the optical constants as:

$$\begin{aligned} X' &= c_x(E_p) + (X - a_x(E_p)) \cdot \frac{d_x(E_p)}{b_x(E_p)} \quad , \\ Y' &= c_y(E_p) + (Y - a_y(E_p)) \cdot \frac{d_y(E_p)}{b_y(E_p)} \quad . \end{aligned} \quad (4.3)$$

The visualization of the relation 4.2 between track parameters and energy and polar angles of the scattered proton is shown in figure 4.11.

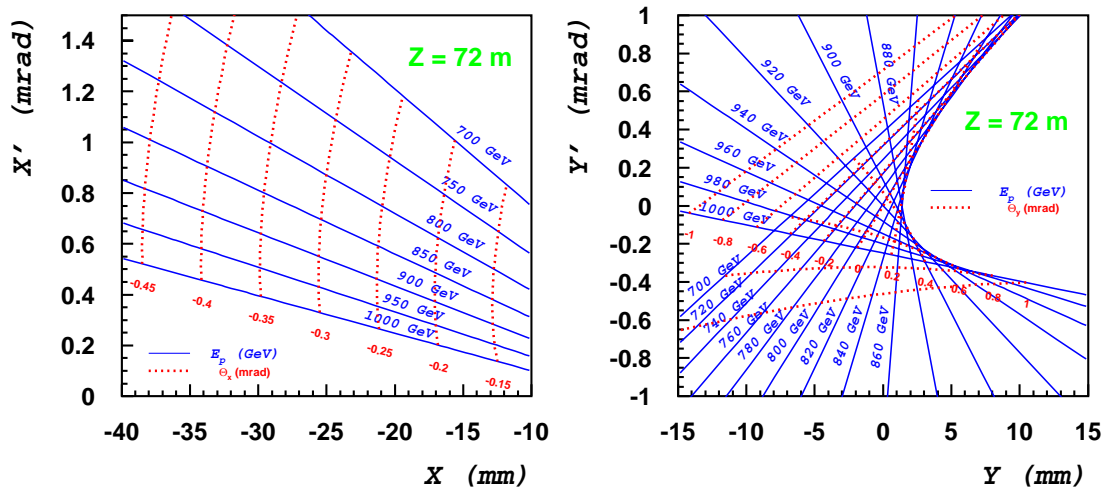


Figure 4.11: *The isolines of constant energy and scattering angles in dependence on the slope and intercept in: a) x - projection, b) y - projection. The solid lines denote the energy E_p and the dashed lines the polar angles Θ_x and Θ_y .*

Finally, the transformation

$$(E_x, \Theta_x, E_y, \Theta_y) \xrightarrow{\text{Cov}_{E_x, \Theta_x, E_y, \Theta_y}^{-1}} (E_p, \Theta_{x,p}, \Theta_{y,p})$$

(see Ref. [79]) is performed using the covariance matrix $\text{Cov}_{E_x, \Theta_x, E_y, \Theta_y}^{-1}$. One can see from the plots of figure 4.11 that each point in the track parameter planes (X, X') and (Y, Y') corresponds to a certain point in the (E_x, Θ_x) and (E_y, Θ_y) planes. The right plot of figure 4.11 shows that there is a significant region in the (Y, Y') plane where each point has two solutions in the (E_y, Θ_y) plane.

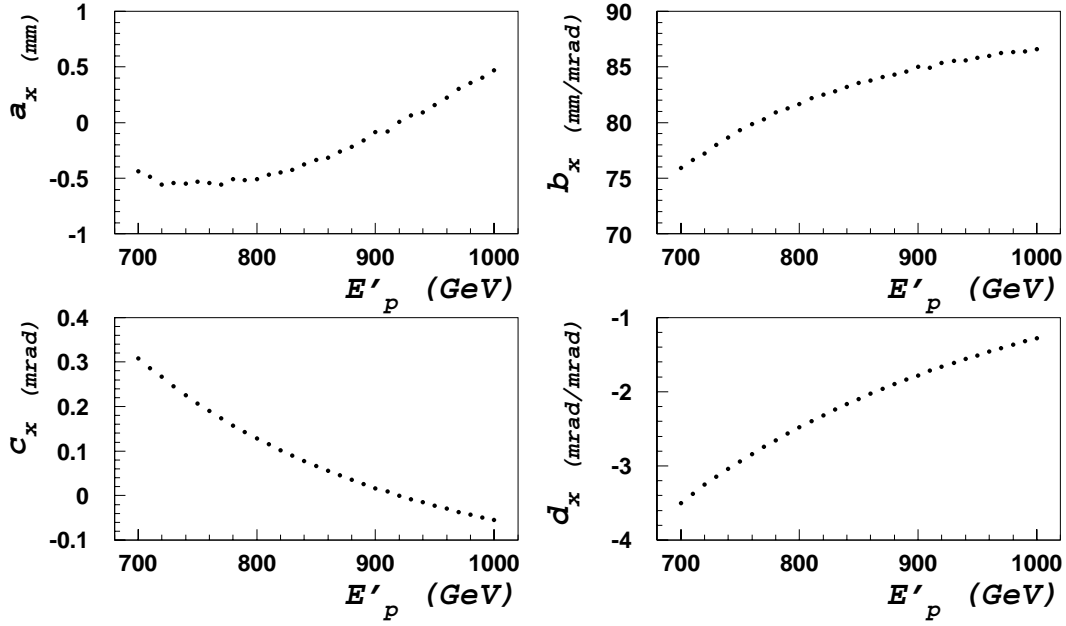


Figure 4.12: *x-projection*: The optical constants in dependence on the scattered proton energy. The optical constants a_x , b_x , c_x , d_x are used for the $(X, X') \Rightarrow (E_x, \Theta_x)$ transformation (see Eq. 4.2, 4.3).

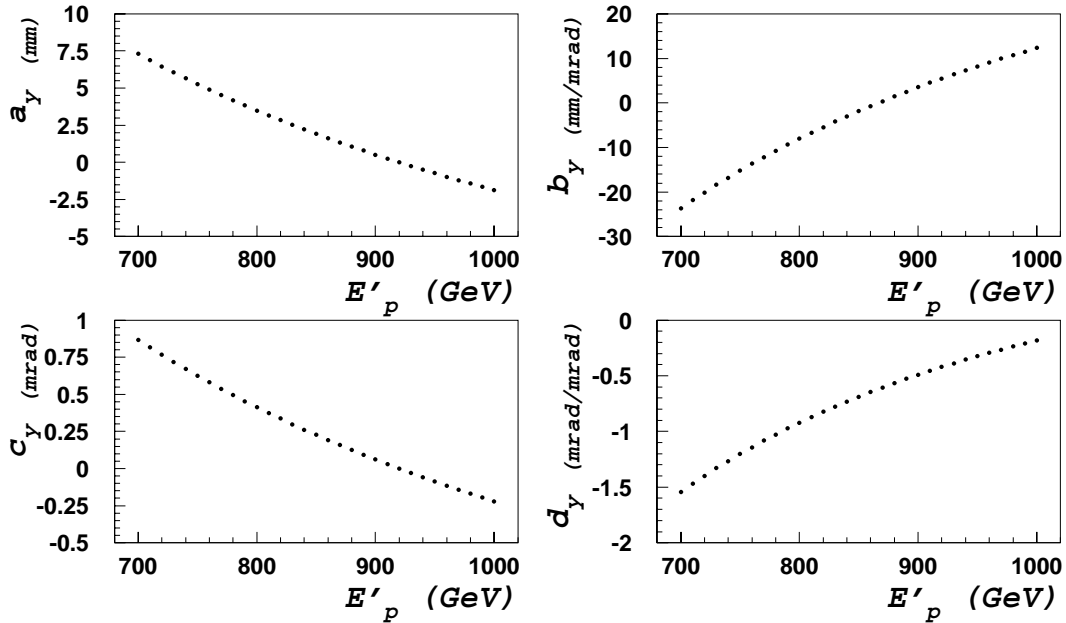


Figure 4.13: *y-projection*: The optical constants in dependence on the scattered proton energy. The optical constants a_y , b_y , c_y , d_y are used for the $(Y, Y') \Rightarrow (E_y, \Theta_y)$ transformation. (see Eq. 4.2, 4.3).

4.6 Calibration

The reconstruction of the track parameters of the scattered proton discussed in sections 4.3–4.4 asserts the scattered proton track parameters with respect to the nominal beam orbit (NB). The actual beam orbit (AB) has an offset and tilt with respect to the NB caused by the peculiarities of the proton beam injection. The transformation from the NB to the AB system is termed calibration and the offsets and tilts of AB with respect to the NB system are termed *calibration constants*. The calibration constants $\kappa_X, \kappa_{X'}, \kappa_Y, \kappa_{Y'}$ transform the scattered proton track parameters from the NB to the AB system:

$$\begin{aligned} X_{ab} &= X_{nb} + \kappa_X & ; & & Y_{ab} &= Y_{nb} + \kappa_Y \\ X'_{ab} &= X'_{nb} + \kappa_{X'} & ; & & Y'_{ab} &= Y'_{nb} + \kappa_{Y'} \end{aligned} \quad (4.4)$$

$X_{nb}, X'_{nb}, Y_{nb}, Y'_{nb}$ – are the track parameters with respect to the NB and $X_{ab}, X'_{ab}, Y_{ab}, Y'_{ab}$ – are the *calibrated* track parameters with respect to the AB system. The calibration constants $\kappa_X, \kappa_{X'}, \kappa_Y, \kappa_{Y'}$ are calculated for each luminosity fill.

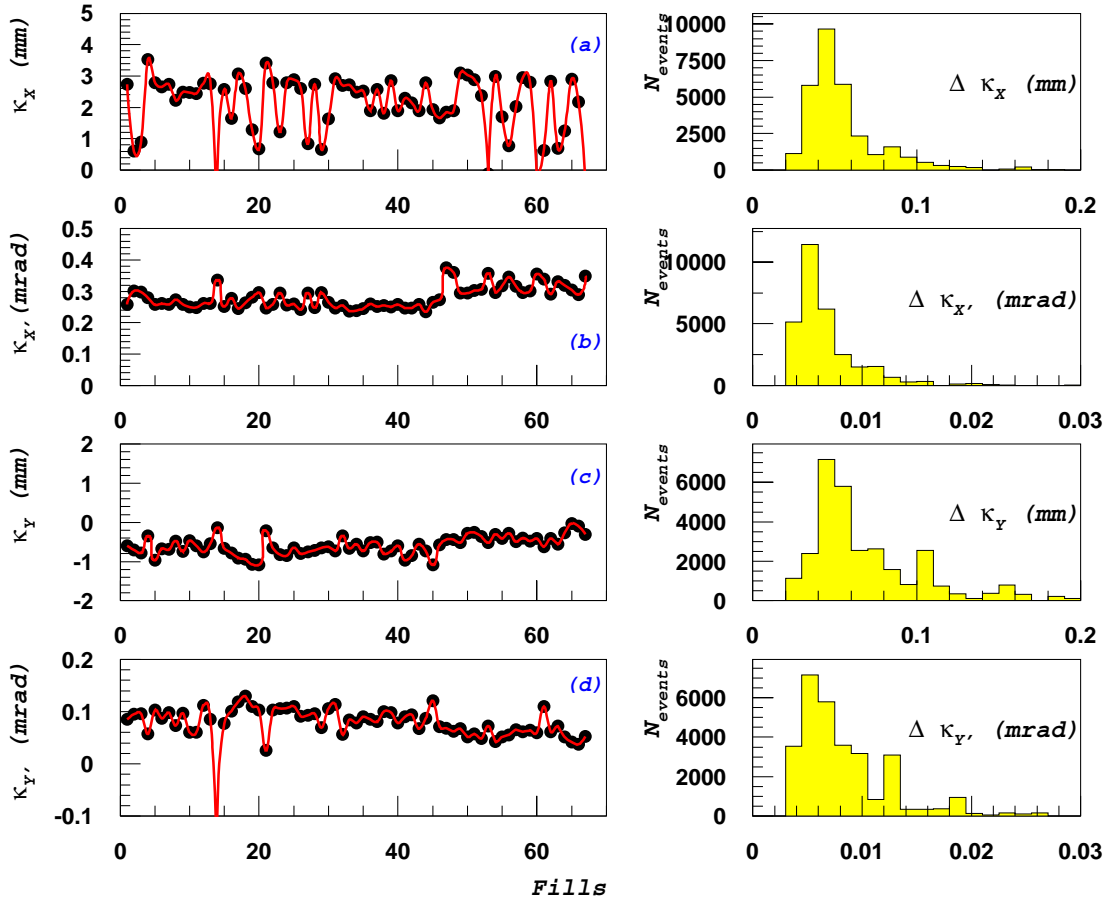


Figure 4.14: **a-d)** Distributions of the calibration constants in dependence of the luminosity fills. The histograms aside of calibration constants plots show the errors of the calibration constants.

As already mentioned above the transformations of x - and y -projections are independent from each other and this feature remains valid for the calibration: the constants κ_X and $\kappa_{X'}$ are independent from the κ_Y and $\kappa_{Y'}$. The calibration is performed using the kinematics of $\gamma p \rightarrow \rho^0 p$ events and contains the following steps.

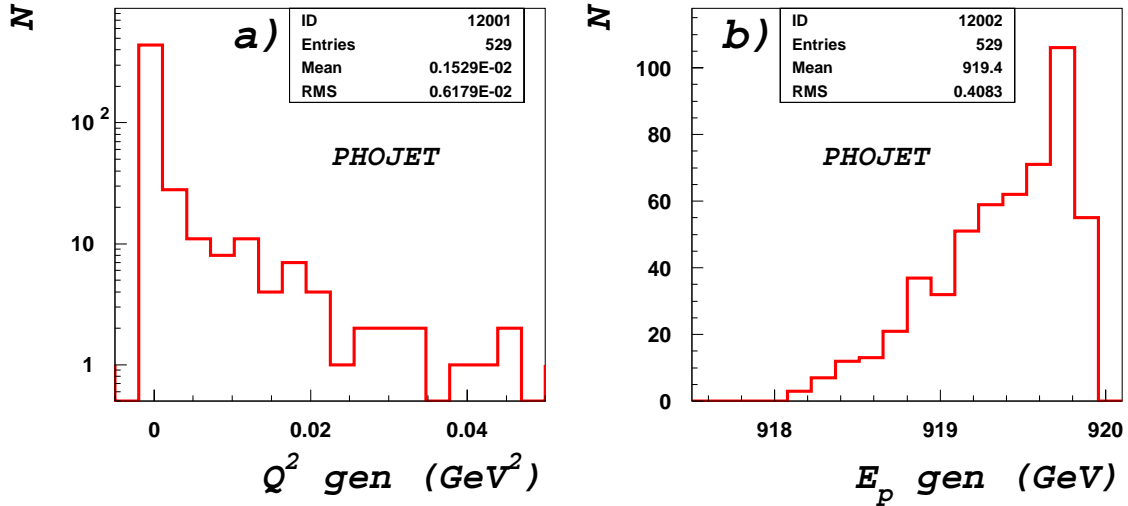


Figure 4.15: The number of Monte Carlo events with a proton detected in the FPS in dependence on **a)** the squared momentum transfer Q_{gen}^2 and **b)** the proton energy $E_{p, gen}$.

1) Calculation of the polar angles Θ_x and Θ_y of the scattered proton in the x and y projections, respectively. They are calculated from the energy and momentum of the ρ^0 -meson measured in central tracker: $p_{x,\rho}$, $p_{y,\rho}$, $p_{z,\rho}$ and E_ρ .

2) Interpolation of the optical constants a_x , b_x , c_x , d_x and a_y , b_y , c_y , d_y to the constant proton energy of $E_p = 919.5 \text{ GeV}$. This is the mean value of the proton energy of $\gamma p \rightarrow \rho^0 p$ events simulated with the FPS as can be seen in figure 4.15b.

3) Use the scattered proton angles Θ_x , Θ_y and the optical constants a_x , b_x , c_x , d_x ; a_y , b_y , c_y , d_y to predict the slope and intercept of the proton global track at the reference position of 72 m (see Eq. 4.2). The difference of the predicted (by equations 4.2) and measured global track parameters are termed *calibration constants*.

4) The procedure is repeated for proton energies of 918 GeV and 920 GeV to determine the systematical error due to the approach of a constant energy of 919.5 GeV .

5) The total error of the calibration constants is given by the width of the distributions of the calibration constants of all ρ^0 events adding the error due to the approach $E_p = 919.5 \text{ GeV}$.

The Q^2 of the $\gamma p \rightarrow \rho^0 p$ process shown in figure 4.15a is small enough to neglect its influence to the systematic errors of the calibration constants.

The comparison of the uncalibrated and calibrated track parameters for the analyzed data sample is presented in the scatter plots and histograms of figures 4.16 and 4.17, respectively. The difference between dashed histogram (uncalibrated tracks) and solid histogram (calibrated tracks) shows the influence of the calibration.

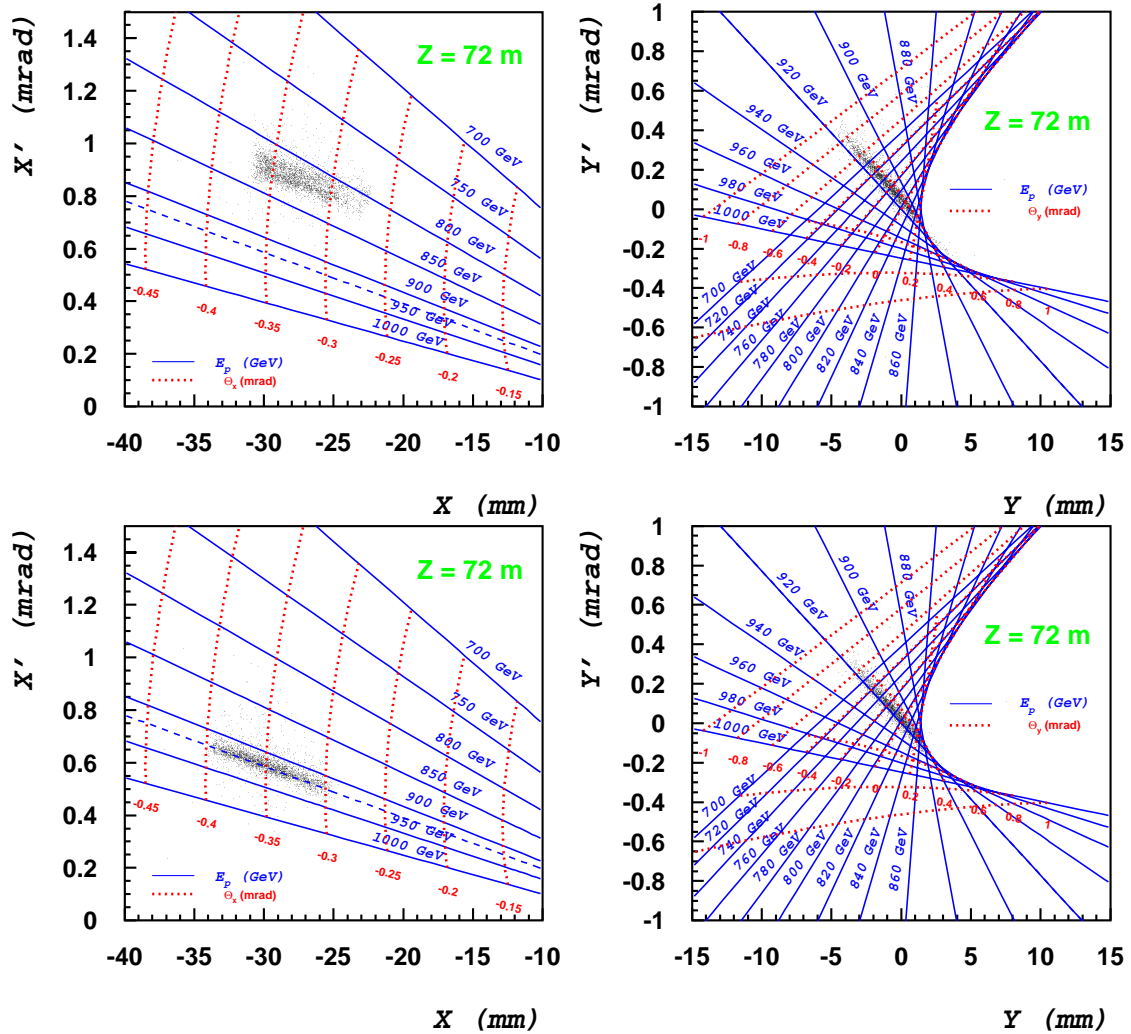


Figure 4.16: **Upper plots:** uncalibrated global tracks in the (X, X') and (Y, Y') planes; **Lower plots:** calibrated global tracks in the (X, X') and (Y, Y') planes.

The calibration is applied only for global tracks in data. There is no need to calibrate the simulated events, because the simulated beam protons coincide with the nominal beam orbit. As mentioned in section 6.3 the incoming beam is simulated using the smearing of polar angles ϑ_x and ϑ_y in x - and y -projections, respectively.

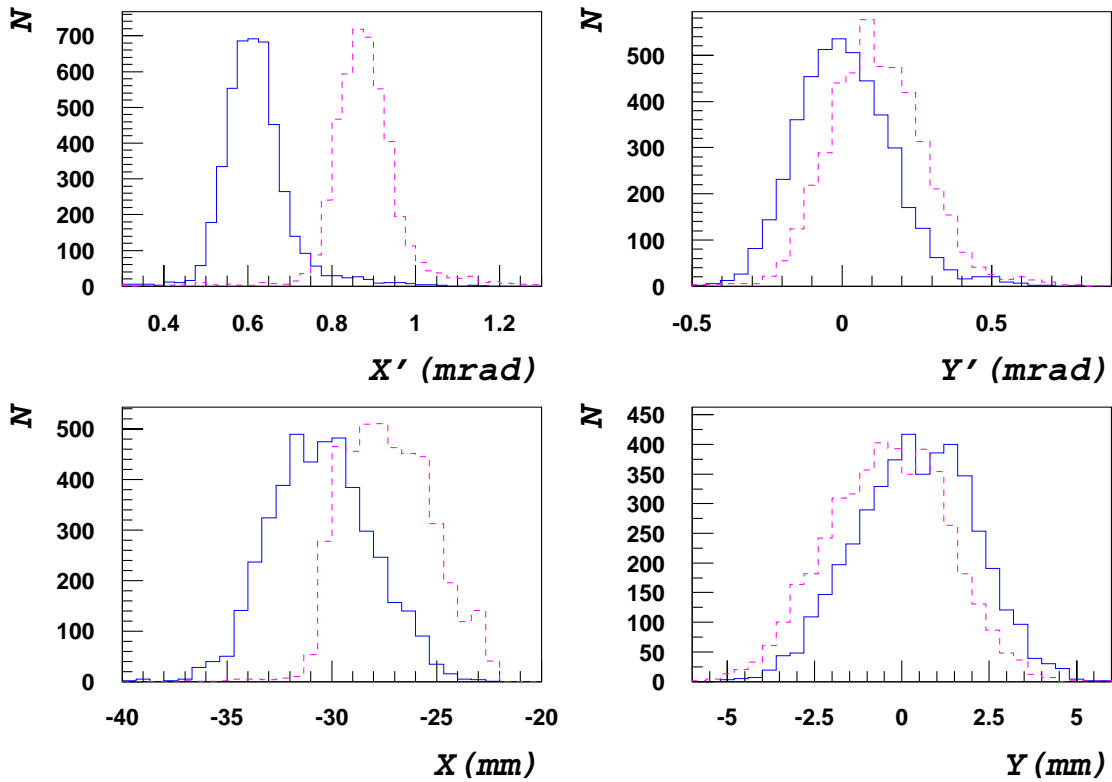


Figure 4.17: Dashed line histograms present reconstructed track parameters before calibration, solid line histograms – after calibration. X' and X are slope and intercept in x projection, Y' and Y – in y projection.

4.7 Proton Energy and Polar Angles

After the calibration the reconstruction procedure of the scattered proton momentum (discussed in section 4.5) is applied. The reconstructed energies and polar angle projections are shown in figure 4.18.

The energy calculated using the equations 4.2 is denoted E_x and E_y for the (X, X') and (Y, Y') transformations, respectively. The ideal case results with $E_x = E_y$. The smearing of the energy reconstruction is shown in figure 4.19 for data and MC. Comparing the width of $E_x - E_y$ in data and simulation (see Tab. 4.3) one can see that the smearing is larger in data than in simulation.

The dots present the data events used in the current analysis. The solid and dashed lines present MC reconstructed events generated by PHOJET and DIFFVM, respectively.

The scatter plots of reconstructed energies and polar angles in dependence on their reconstruction errors are presented at figure 4.20. The mean value of the $\Delta\Theta_y$ is one

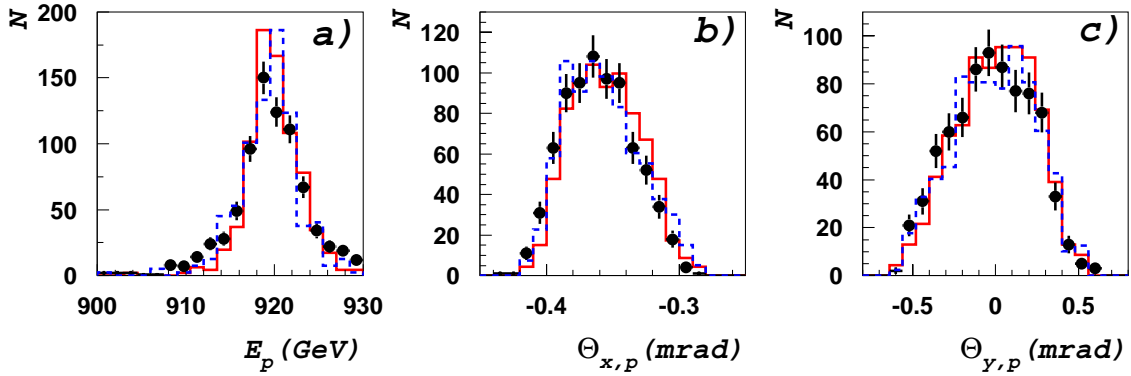


Figure 4.18: Energy and polar angle projections Θ_x and Θ_y of scattered proton measured in FPS horizontal stations.

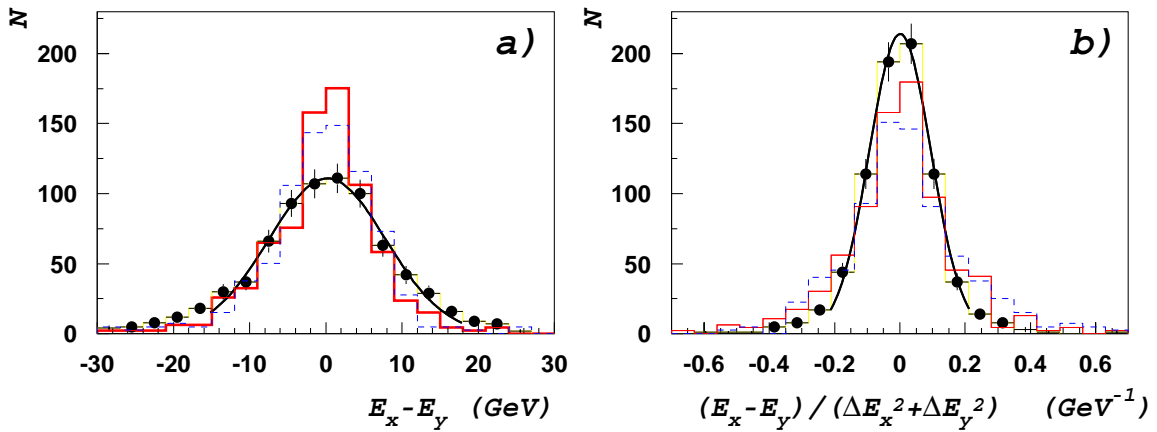


Figure 4.19: **a)** Difference of the proton energy values E_x and E_y reconstructed by optical and calibration constants in x and y projections, correspondingly. **b)** Difference divided by the sum of the squared errors ΔE_x and ΔE_y . These are the reconstruction errors of the proton energy values E_x and E_y .

	DATA	PHOJET	DIFFVM	Units
$\langle E_x - E_y \rangle$ (GeV)	-0.2	-0.1	-0.3	GeV
RMS($E_x - E_y$) (GeV)	9.4	6.5	8.1	GeV

Table 4.3: Mean values and root mean square deviations (RMS) for the scattered proton energy balance measured in the FPS.

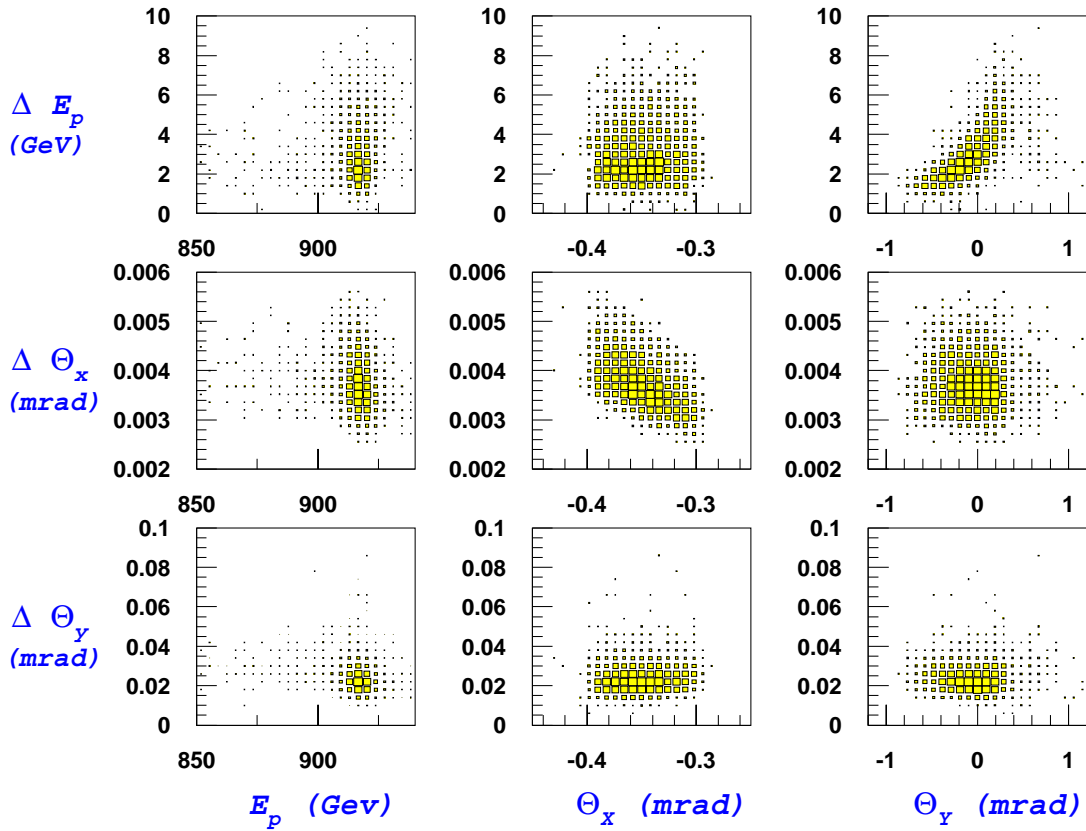


Figure 4.20: *The errors of the proton energy and polar angles in dependence on the proton energy and polar angles for protons measured in FPS horizontal stations.*

order of magnitude larger than the $\Delta \Theta_x$. The horizontal stations are constructed to move in the x -direction. Therefore they are more sensitive and the measurement is more precise in the x than in the y projection. The mean value of the energy error ΔE_p is approximately the same for all reconstructed energies E_p and angles Θ_x , Θ_y .

Chapter 5

Event Selection

The data used in the current analysis are collected during January–April 1999 $e^- p$ colliding period of HERA. The analysis is based on the scattered proton momentum measurement in the FPS horizontal stations and on the ρ -meson decay pions measurement in the H1 central tracker. The data used are taken from the *luminosity fills* with significant statistics of ρ^0 -meson candidates. The luminosity fill is defined as a group of several data runs. In what follows the data sample, selection criteria, background, vertex analysis, collected luminosity and photon flux calculation are described.

5.1 Data Sample

The collected event sample requires a coincidence of a positive trigger decision from both FPS horizontal stations (see Sec. 3.6). The data events used for the cross section measurement and trigger efficiency calculation are collected in two different samples. These samples are independent from each other.

Sample 1 – is used for the elastic ρ^0 cross section calculation. It is based on events with subtrigger ST 107. This subtrigger serves for the triggering of untagged photoproduction with a leading proton. The leading proton in photoproduction is defined as a scattered proton from $e p$ interaction. The definition of the ST 107 is:

$$\text{FPS_HOR} \ \&\& \ \text{DCRPh_Ta} \ \&\& \ \text{zVtx_cls} \ \&\& \ \text{v:3} \ \&\& \ \text{t:0} \quad (5.1)$$

The expression 5.1 contains the following elements (Sec. 3.6) combined in "AND" logic:

1) FPS_HOR – the FPS horizontal detectors trigger elements TE 164 and TE 165 of the 80 m and 64 m stations, correspondingly. 2) DCRPh_Ta – the DCR ϕ trigger element TE 17. 3) zVtx_cls – the zVtx cluster trigger element TE 29. 4) v:3 – the *Time of Flight* and *veto counters* coincided trigger decision. 5) t:0 – the zVtx_T0 one track trigger decision.

Sample 2 – is used for trigger efficiency calculation. The sample 2 is based on the positive trigger decisions from the H1 subtriggers which are *independent* from ST 107. A subtrigger is termed *independent* if it contains no component of the expression 5.1. The events with *independent* subtriggers are combined into the sample 2 by “OR” logic. The definition of independent subtriggers and their rates for selected runs are listed in table 5.1.

Subtrigger	Subtrigger components	Rate
ST 0	$SPCLe_JET > 2$ v:4 f:1	4860
ST 1	$SPCLe_JET > 2$ v:3 z:0 f:1 t:3	5383
ST 5	$SPCLe_JET > 2 SPCLe_JET_Cen_3 \& \& PToF_IA \& \& LAr_IF$ v:3 f:0	138
ST 23	$FwdMu_Val_Multi \& \& Mu_2_FEC$ v:5 f:0	30
ST 35	$SPCLe_JET > 2 \& \& SPCLe_ToF_E_2$ v:8 f:0	6022
ST 39	$FwdRay_T0 \& \& LAr_IF \& \& LAr_BR \& \& LAr_electron_2$ v:0 f:0	325
ST 46	VLQ_high_OR v:8 f:2	2673
ST 50	$eTAG \& \& (SPCLe_JET > 1 SPCLe_JET_Cen_2)$ v:0 f:1 r:3	305
ST 63	$FwdMu_Val_Any \& \& VETO_Or_Global$	3613
ST 66	$LAr_Etmis > 2 \& \& LAr_IF > 1$ v:3 f:5 t:8 l:0	232
ST 67	$LAr_electron_1$ v:4 f:5 t:8 l:0	289
ST 70	$eTAG \& \& SPCLe_ToF_E_1$ v:3 f:0 r:3	2551
ST 72	$SPCLe_ToF_E_1$ v:0 f:0	87
ST 76	$LAr_Etrans > 1 \& \& CIP_2$ v:0 t:3 f:0 r:7 l:0	13
ST 77	$LAr_Etmis > 1$ v:0 r:0 f:5 t:3 l:0	198
ST 81	$eTAG_all \& \& (SPCLe_JET > 1 SPCLe_JET_Cen_2)$ v:0 f:1 r:3	514
ST 86	$eTAG$	893
ST 97	$eTAG \& \& (FNC_Esum > 1) \& \& VLQ_noise$ v:8 f:2	4022
ST 99	$LU_ET_8 LU_ET_7$	9286
ST 105	$eTAG_all \& \& SPCLe_ToF_E_1$ v:3 f:0 r:3	133
ST 110	$VLQ_low_OR \& \& LAr_CB > 1 \& \& LAr_FB > 1$ v:8 f:3	25
$\bigvee_i ST_i$		30717

Table 5.1: The independent subtriggers with respect to the ST 107 with their trigger elements. The last row presents the number of events in the period from January to April 1999 used for trigger efficiency calculation. This value, denoted as $\bigvee_i ST_i$, combines all independent subtrigger rates in “OR” logic.

5.2 Selection Criteria

The reconstruction procedure is based on the H1REC package. The reconstructed events are selected by four sets of selection criteria: **I)** the trigger criteria; **II)** the detectors *basic* criteria; **III)** the proton selection criteria in FPS; **IV)** the elastic ρ^0 -meson selection criteria.

I Level 1 and Level 4 trigger criteria:

- i** Level 1: The ST 107 has a positive decision. This criterion includes the pre-scale factor (discussed in Sec. 3.6) PF 107 which suppress event rates of the ST 107 by a predefined run dependent weight. For runs selected in the current analysis the mean PF value of ST 107 is $\langle PF\ 107 \rangle = 1.6$. The run dependent PF 107 is used to calculate the operation luminosity of ST 107 (see Eq. 5.4).
- i** Level 4: The events belong to the *class 14*. The *class 14* – is the event classification criterion for leading baryons performed from the FPS side by a minimum number of hits in the fiber detectors using the *filtering procedure* ROPVER which is included in H1REC. The filtering rate of event classification is about 0.09 Hz.

II Detectors *basic* criteria:

- ii** High Voltage and read-out status “OK”.
Events are considered if the detectors involved to the measurement of untagged ρ^0 photoproduction are ready for read-out. These detectors are: 1) FPS horizontal stations; 2) Central Tracking Detectors – CJC, CIP, COP; 3) Forward Tracking Detectors – Radial & Planar drift chambers; 4) Calorimeters – LAr, SpaCal; 5) LUMI, ToF and Veto Counters. The same HV control criteria are applied for operation luminosity calculation.
- iii** The FPS horizontal stations are in *stable measuring position*.
The positions of the stations are measured on-line by the detector positioning equipment and recorded by the slow control system in time steps of seconds. The stability is checked off-line comparing the measured position values in dependence on time. The detector positions for selected runs are in the ranges $-30 \div -15\ mm$ and $-35 \div -25\ mm$ (see Fig. 4.7) for 80 *m* and 64 *m* stations, respectively.
- iv** There are no electron candidates in the SpaCal and/or LAr calorimeters.
This criterion is essential to reduce background from inelastic processes and beam gas/walls interactions.
- v** There is one positive and one negative charged track in the central tracker.
This criterion implies that there are no other tracks in the H1 trackers, neither in the central nor in forward region.

- vi The reconstructed z -Vertex is inside a distance of 30 cm from the nominal z_0 interaction point as shown in figure 5.4.

III The proton selection criteria in FPS:

- vii There is a reconstructed proton track in both 80 m and 64 m horizontal stations. At this analysis stage the *calibration* procedure of the FPS is performed.
- viii The reconstructed values of the scattered proton energy E_p and polar angle projections $\Theta_{x,p}$ and $\Theta_{y,p}$ are inside the following kinematic regions:
 - 1) $900 < E_p < 930 \text{ GeV}$;
 - 2) $-0.400 < \Theta_{x,p} < -0.295 \text{ mrad}$;
 - 3) $-0.700 < \Theta_{y,p} < 0.700 \text{ mrad}$.

IV Elastic ρ -meson selection criteria:

- ix The two pions invariant mass is inside of $0.5 \leq M_{\pi\pi} \leq 1.1 \text{ GeV}$ interval. This interval is chosen by the experimental conditions and cut the bulk of resonant background in the low mass region $M_{\pi\pi} \leq 0.5 \text{ GeV}$ and non-resonant background in the high mass region $M_{\pi\pi} \geq 1.1 \text{ GeV}$.
- x The inelasticity y calculated from outgoing hadrons is $0.004 < y < 0.060$ (see Eq. 2.9). This inelasticity region corresponds to the γp CME interval of $20 < W < 80 \text{ GeV}$. The distributions of y and W are presented in figure 6.5.
- xi The proton momentum transfer is $0.08 \leq |t| \leq 0.38 \text{ GeV}^2$. This $|t|$ interval is restricted by the FPS acceptance.
- xii The transverse momentum of the *leading pion* is greater than 0.45 GeV . The leading pion is the pion from the ρ^0 -decay with the greatest transverse momentum p_t . The leading pion reconstructed in the CJC is responsible for the DCR ϕ trigger decision. The necessity of this cut is needed to avoid large uncertainty of the DCR ϕ trigger efficiency below 0.45 GeV (see Fig. 6.8).
- xiii Pion identification.
The measured value of the ionization energy losses is used to calculate the probability $\mathcal{P}_{dE/dx}(\pi)$ that the measured particle is a pion (see Sec. 5.3). This criterion is applied for both, the positive and the negative pion candidates. If the probability $\mathcal{P}_{dE/dx}(\pi^+)$ is greater 5 % and $\mathcal{P}_{dE/dx}(\pi^-)$ is greater 5 % then this event is included in the analysis.
- xiv The difference of the ρ^0 -meson and scattered proton azimuthal angles $|\phi_p - \phi_\rho|$ is $0.7\pi < |\phi_p - \phi_\rho| < 1.3\pi$. The scattered proton and elastic ρ -meson measured in the CMS of ρ^0 -production plane have opposite directions. The angular distribution of ρ^0 photoproduction is briefly discussed in section 2.5. The reconstructed azimuthal angular difference $|\phi_p - \phi_\rho|$ has a smearing of about $0.15 \cdot \pi$ width. Twice this value is applied in this criterion.

The number of events in sample 1 with application of criteria **i–xiv** are listed in table 5.2.

Group	n _{sel}	Selection criteria	N _{events}
(I) L1&L4	i	Subtrigger 107 && Class 14	63287
(II) Basic sel.	ii	&& HV & read-out status “OK”	48266
	iii	&& FPS in stable measuring position	42500
	iv	&& No electron in SPACAL & LAr	42049
	v	&& One pos. and one neg. track in CT	7812
	vi	&& Reconstructed z -Vertex $Z_0 \pm 30$ cm	7379
(III) FPS sel.	vii	&& Proton track candidate in FPS	4405
	viii	&& Reconstructed proton in FPS	3288
(IV) ρ^0	ix	&& $0.5 \leq M_{\pi\pi} \leq 1.1$ GeV	1742
	x	&& $0.004 < y < 0.06$	1710
	xi	&& $0.08 \leq t \leq 0.38$ GeV ²	1610
	xii	&& $p_{t, \pi \text{ lead}} > 0.45$ GeV	1328
	xiii	&& Probability $\mathcal{P}_{dE/dx}(\pi) > 5\%$	1154
	xiv	&& $0.7 \cdot \pi < \phi_p - \phi_\rho < 1.3 \cdot \pi$	1030

Table 5.2: Number of events in the data sample 1 for the selection criteria **i–xiv**. The criteria **i–xiv** are grouped in four sets **I–IV** each of which denotes the different analysis stages.

5.3 Background Treatment

The possible background respects to the physics of the γp interaction, kinematics of ρ^0 production, and experimental conditions at H1. The following background sources to the untagged photoproduction with the measured scattered proton in the FPS, are considered: **1)** resonant and non-resonant diffraction processes produced in the γp interaction which may be misidentified as $\gamma p \rightarrow \rho^0 p$; **2)** erroneous particle identification of the measured charged particle as a pion candidate in the central H1 tracking system; **3)** non $e p$ proton-like track induced by remnant gas or proton pipe wall interactions and reconstructed in the FPS as the scattered proton of $\gamma p \rightarrow \rho^0 p$.

The last background source is checked by rates of local tracks measured in FPS horizontal stations at different experimental conditions (see Ref. [81]). The estimated contribution of the proton pipe contamination background is about 1%.

Physical Background to $\gamma p \rightarrow \rho^0 p$

The following physical background terms are:

1) contribution of elastic $\omega(782)$ [82] and $\phi(1020)$ [83] vector meson photoproduction;

2) contribution of non-resonant $\pi^+\pi^-$ production from the $\gamma p \rightarrow \pi^+\pi^- p$.

The spectra of possible physical background processes to the elastic $\rho^0(770)$ photoproduction simulated in PHOJET are shown in figures 5.1, 5.2. The background spectra of $\omega(782)$, $\phi(1020)$ and $\pi^+\pi^-$ which are shown in these figures are reduced after the application of selection criteria **i–viii** described in section 5.2.

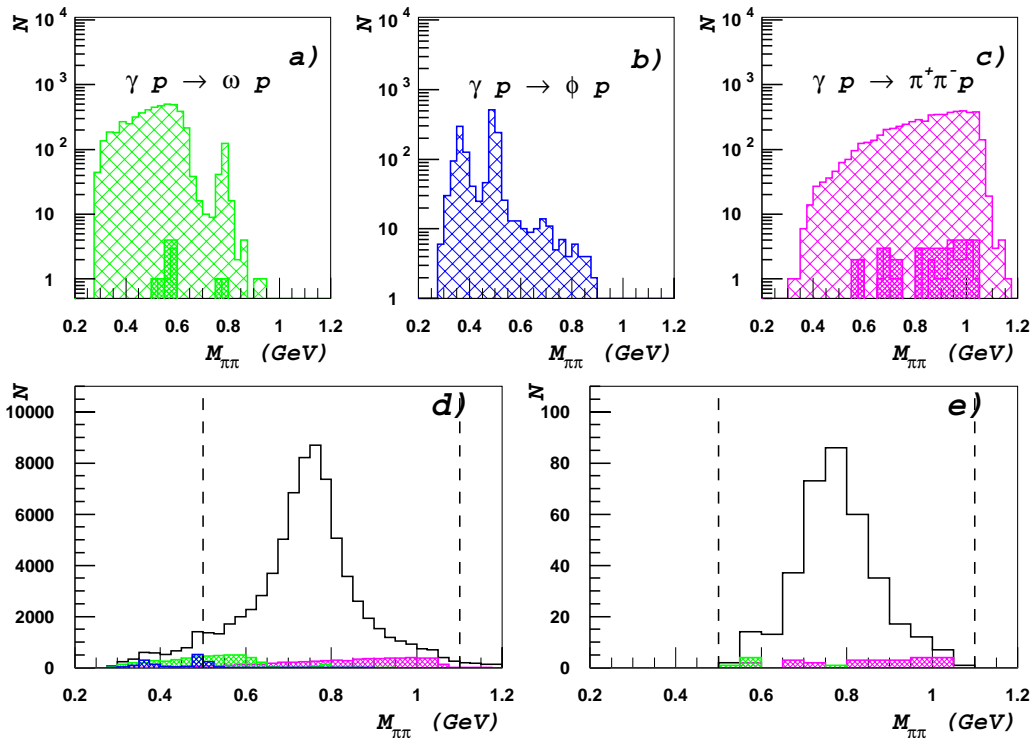


Figure 5.1: Distributions of the invariant mass of two pions $M_{\pi\pi}$ uncorrected for measurement efficiency. **a,b,c)** Background spectra of ω , ϕ and non-resonant $\pi^+\pi^-$ production, respectively. **d,e)** The open histograms represent the full simulated spectra of ρ^0 photoproduction plus background. The shaded histograms show the background distributions of plots **a,b,c**: **d)** before and **e)** after application of the selection criteria.

The cross-hatched histograms of plots **a,b,c** in figures 5.1, 5.2 show the background contribution at basic selection criteria of **i–vi** from ω , ϕ and non-resonant $\pi^+\pi^-$ production, respectively. The shaded histograms inside the cross-hatched histograms of plots **a,b,c** show the background remnant after the application of the final selection criteria **i–xiv** (see Sec. 5.2). There are no remnant events from the $\gamma p \rightarrow \phi p$, and the bulk of the remaining background is non-resonant $\pi^+\pi^-$ production process. The corresponding MC reconstructed event rates from the photoproduction processes simulated by PHOJET are presented in figures 5.1 and 5.2.

The contribution of different processes shown in figures 5.1 d,e and 5.2 d,e are listed in table 5.3. The fraction of vector mesons is simulated according to the values given in expression 2.47.

Photoproduction of		ρ^0	ω	ϕ	$\pi^+\pi^-$
Relative rate	Basic cuts	83.3 %	6.8 %	2.0 %	7.9 %
	Final cuts	91.6 %	1.7 %	0.0 %	6.7 %

Table 5.3: The relative rates of the ρ^0 -meson photoproduction and corresponding background reconstructed in Monte Carlo with the H1 central tracker and FPS horizontal stations. *Basic* and *final* cuts correspond to groups **I-II** and **I-IV**, respectively.

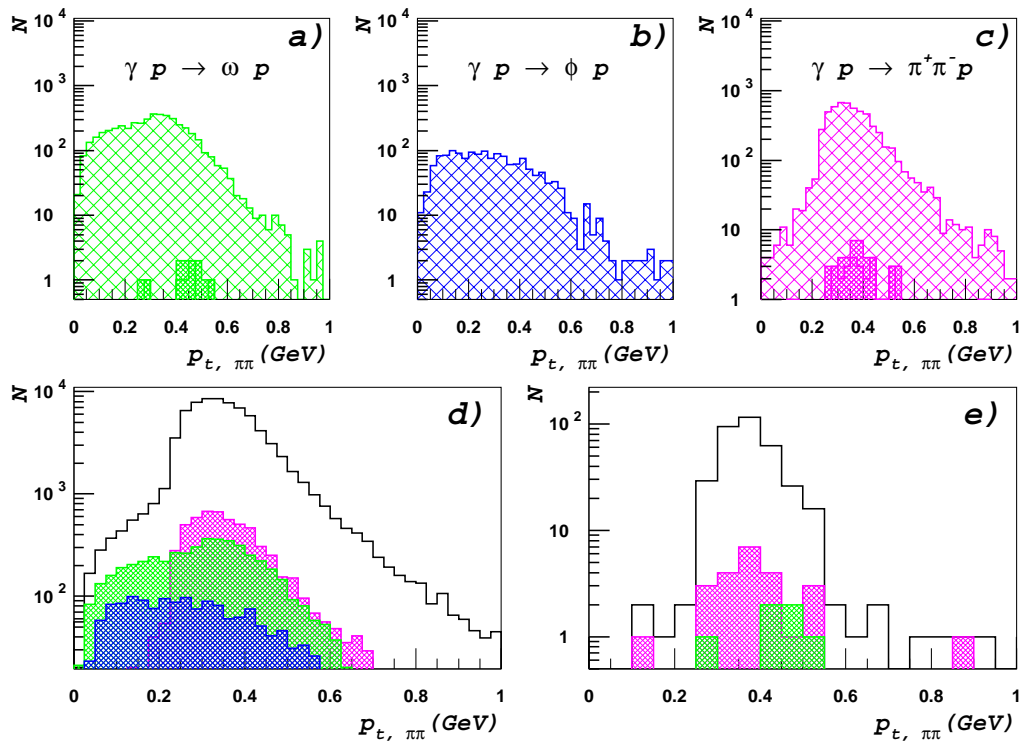


Figure 5.2: Distributions of the transverse momentum p_t of the $\pi^+\pi^-$ system measured in CJC. The distributions are not corrected for the measurement efficiency. **a,b,c)** The reconstructed p_t spectra of the simulated background of ω , ϕ and non-resonant $\pi^+\pi^-$ photoproduction, respectively. **d,e)** The open histograms represent the p_t spectrum of all simulated processes for the **basic (d)** and **final (e)** selection criteria. The shaded histograms in the plots **d** and **e** show the background distributions of plots **a,b,c** inside the full p_t spectra.

Identification of Pions in the Central Tracker

As discussed in sections 3.3, 3.6.2 charge and momentum values of the charged particles are given by the track parameters reconstructed in the CJC. The ionization loss in the central jet chamber CJC is used for particle identification.

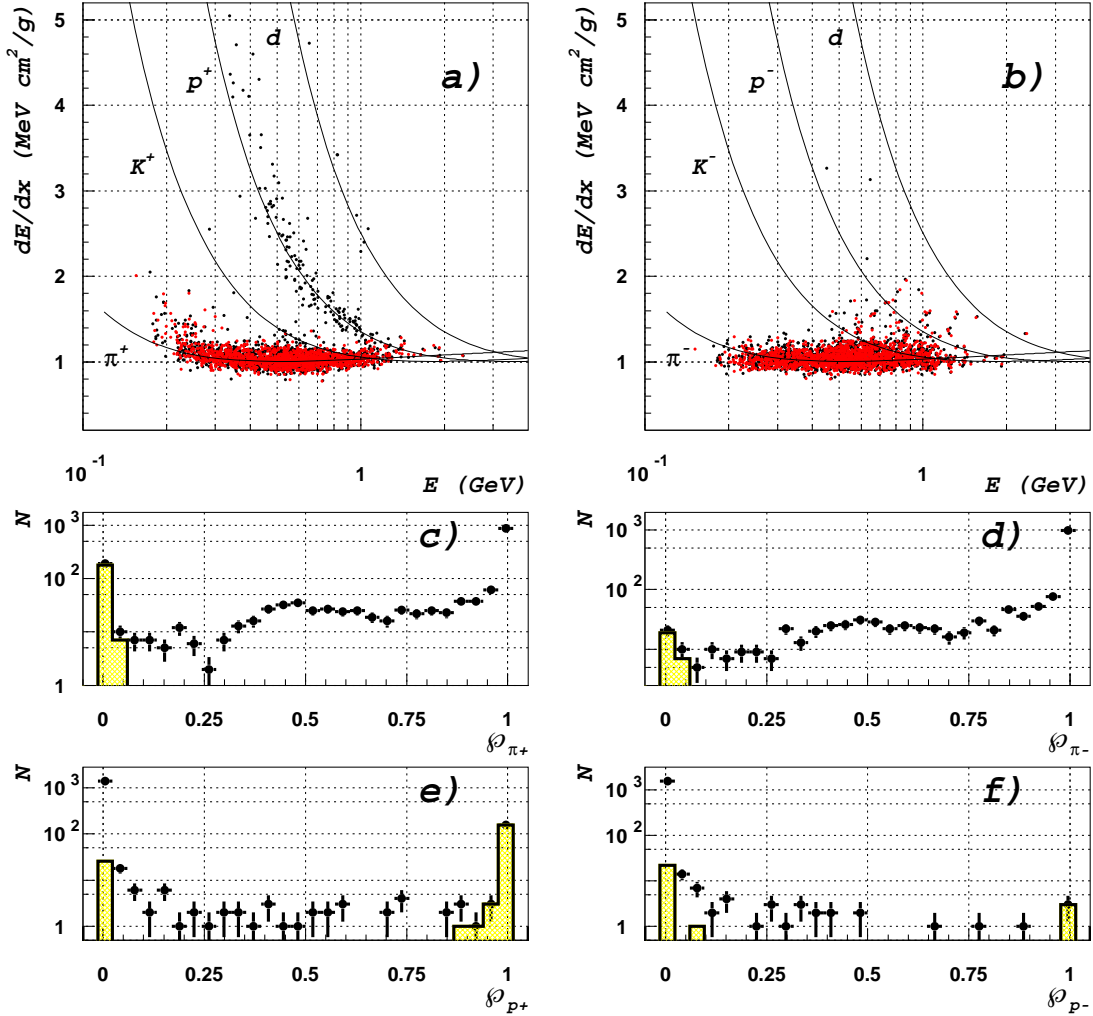


Figure 5.3: **a,b)** The ionization energy losses for positive and negative particles in the event sample selected by the criteria **i–xii** of table 5.2. **c–f)** The probability to have a π^+ , π^- , proton and antiproton respectively in this events sample.

The ionization energy losses of the charged particle are expressed by the Bethe-Bloch equation:

$$-\frac{dE}{dx} = \frac{4\pi n Z^2 e^4}{m_e v^2} \cdot \left[\ln\left(\frac{2m_e c^2}{\hat{I} \cdot (1 - \beta^2)} \cdot \frac{P^2}{M^2}\right) - 2\beta^2 - \delta \right] \quad (5.2)$$

where Z – atomic charge, e – electron charge, m_e – electron mass, v – velocity of the charged particle, $\beta = v/c$, n – is the number of electrons in a unit volume, \hat{I} – is the mean potential of atomic ionization, P and M are the momentum and mass of the charged particle respectively, δ – is the density correction term.

Equation 5.2 is used to identify particles by the comparison of the dE/dx value with the measured momentum P to chose the most appropriate mass M . This method defines a certain probability $\mathcal{P}_{dE/dx}$ calculated by the H1 software package DEDXMOD and used in the current analysis as the selection criterion **xiii** discussed in section 5.2. As one can see in figure 4.7 the most significant contribution to an erroneous pion identification is made by protons. The condition of $\mathcal{P}_{dE/dx}(\pi) > 5\%$ rejects about 13% of the accepted events. About 10% of rejected events belong to protons and the remaining 3% belong to kaons and deuterons.

5.4 Vertex Analysis

z -Vertex

In the current analysis the vertex is reconstructed in the central region of the H1 detector. A schematic view of the z -vertex reconstruction procedure of two pion candidates is shown in figure 3.10. The reconstructed vertex for selected events is presented in figure 5.4. It is important to evaluate the mean and variance of the z -vertex in order to reject background from ep scattering. The events with large deviations from the nominal interaction point are excluded by the criterion **vi** from the table 5.2.

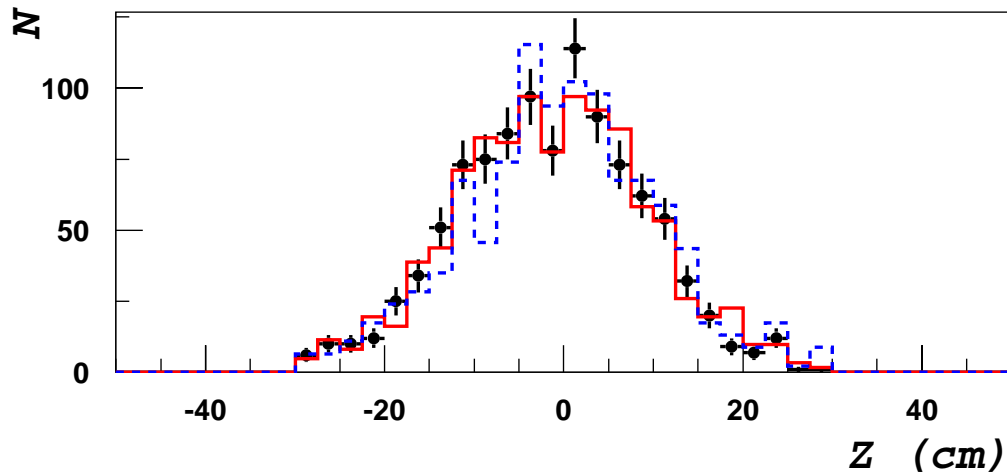


Figure 5.4: The z -vertex distributions of the analyzed events. The filled dots present data, the solid line – PHOJET, the dashed line – DIFFVM.

x, y -Vertex

A scan of the x , y and z -vertex positions for the analyzed luminosity fills are presented in figure 5.5. The dashed line of figure 5.5 represent the mean value of the vertex projection in the range of selected runs. This mean value is included in the Monte Carlo vertex simulation.

The optical features of the proton beam at the place of the horizontal stations makes the measurement ability of the horizontal stations sensitive mostly to the x -projection. The figure 5.5 shows that the y -position of the interaction point is more stable in comparison to the x -position.

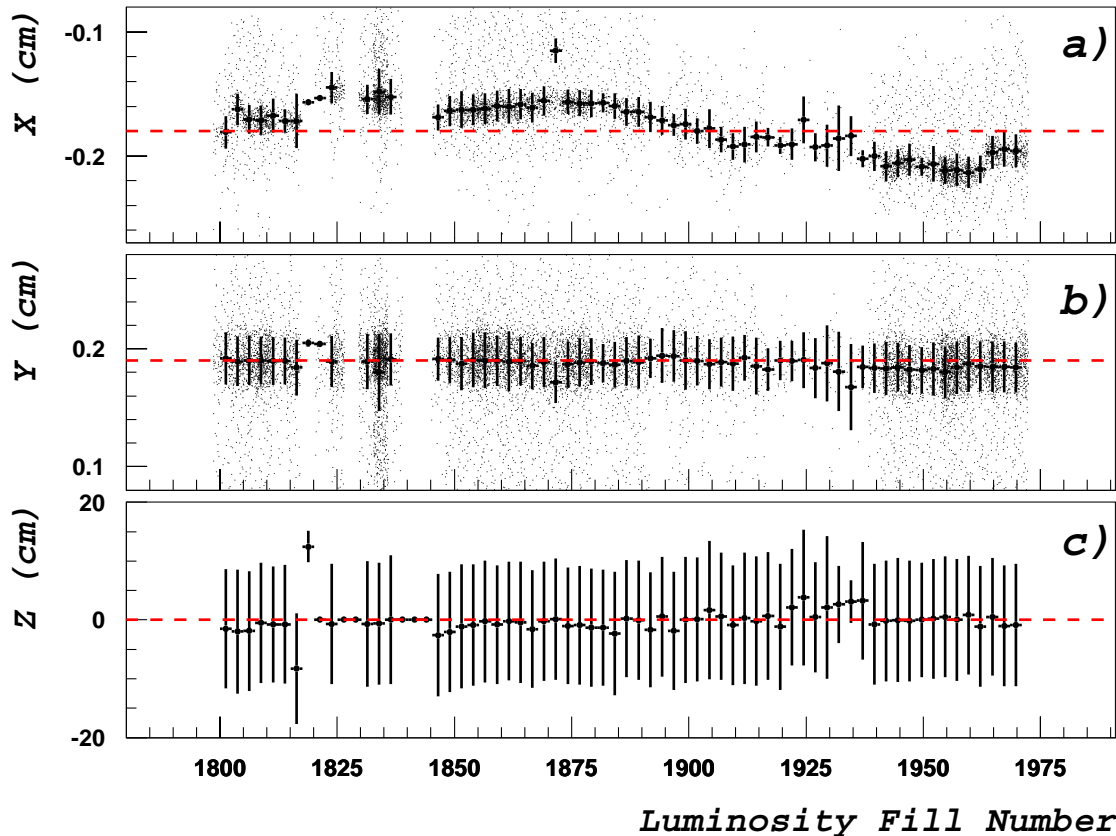


Figure 5.5: *The reconstructed vertex position of the analyzed data sample for different luminosity fills. a) x -vertex; b) y -vertex; c) z -vertex. Error bars represent the Gaussian spread. The dashed line denotes the mean value used in Monte Carlo for the vertex simulation.*

The polar angle of the scattered proton Θ_p measured in the FPS is reconstructed as a function of the optical constants (discussed in Sec. 4.5). This function is sensitive to the ep interaction point, hence the vertex position affects the Θ_p . The mean vertex position is luminosity fill dependent as one can see in figure 5.5.

5.5 Luminosity

As described in section 3.5 the H1 luminosity system counts the rate of the bremsstrahlung photons. This rate cannot be separated in luminosity monitors by their sources. Because of that the total rate of the Bethe-Heitler photons contains a crossbred from the ep interaction bunches and satellite bunches.

To subtract the satellite bunch fraction from the luminosity measurement, a correction procedure is applied run by run to the measured luminosity value. The satellite bunch correction λ , shown in figure 5.6 in dependence on the analyzed luminosity fills, is estimated by the ratio of the satellite rate to the total bremsstrahlung rate:

$$\lambda = N_{run}^{satel} / N_{run}^{tot} \quad (5.3)$$

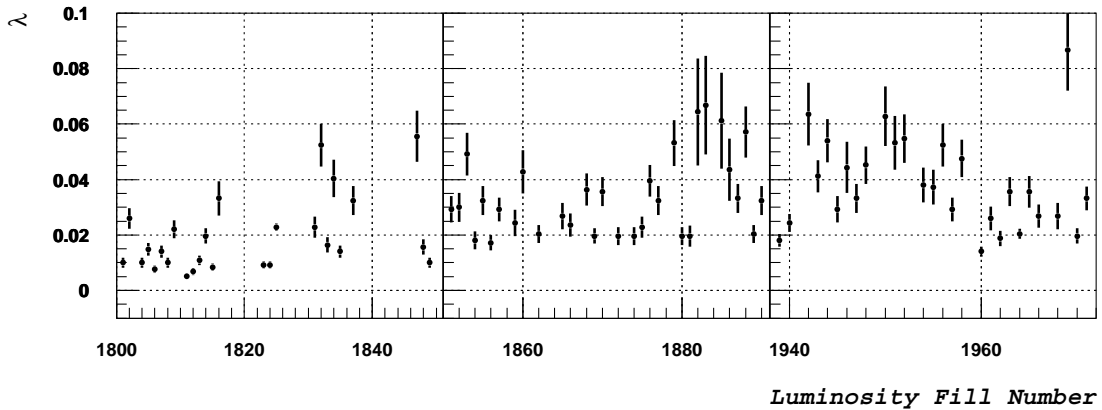


Figure 5.6: *Satellite bunches correction λ to the measured luminosity.*

In this analysis the luminosity is calculated according to equation 3.1 under the following conditions: **1)** the FPS horizontal stations are in measuring positions and the detectors involved in the analysis are ready for data taking (criteria **ii**, **iii**, table 5.2); **2)** the event vertex is inside the region of ± 30 cm around the z_0 position of the nominal vertex (criterion **vi**, table 5.2). **3)** The luminosity calculation is considered with respect to the subtrigger 107:

$$\mathcal{L} = \sum_{runs} \frac{\mathcal{L}_{run} \cdot (1 - \lambda)}{PF(107)} \quad (5.4)$$

Here \mathcal{L}_{run} – is the luminosity, measured in one data run at the conditions **ii**, **iii** and **vi** from table 5.2; λ – is the satellite bunches correction defined in expression 5.3; $PF(107)$ – is the pre-scale factor of ST 107.

The luminosity \mathcal{L} calculated under these conditions is termed *operation luminosity*. The operation luminosity for the selected luminosity fills is $\mathcal{L} = 2039.68 \text{ nb}^{-1}$. The operation luminosity in dependence on the luminosity fills is shown in figure 5.7.

The dependence of the operation luminosity \mathcal{L} from the number of collected events is presented in figure 5.8 for analysis stages of **II**, **III** and **IV** discussed in section 5.2 and listed in table 5.2. As one can see from figure 5.8 the distributions have a nonlinear behavior. This happens due to the varying FPS acceptance, which is a function of the changeable FPS detectors position. The slope variation in figure 5.8 indicates the FPS acceptance variation for the different run ranges. The dashed lines in figure 5.8 indicates the mean slope during the full range of the selected luminosity fills at the analysis stages of **II**, **III** and **IV**.

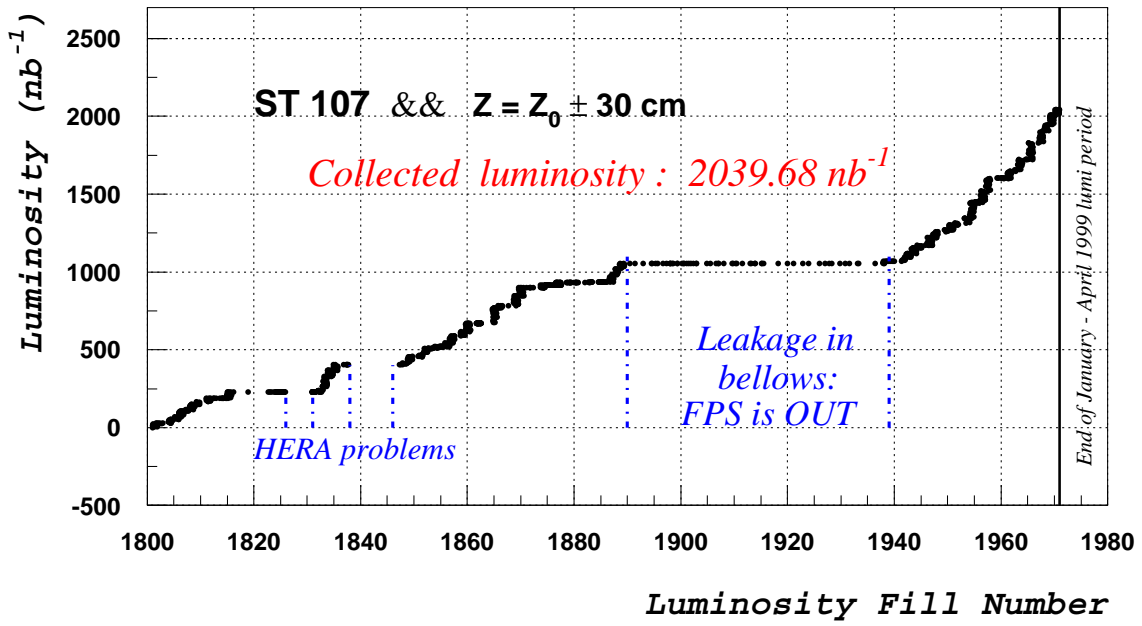


Figure 5.7: FPS operation luminosity of subtrigger 107 for selected luminosity fills.

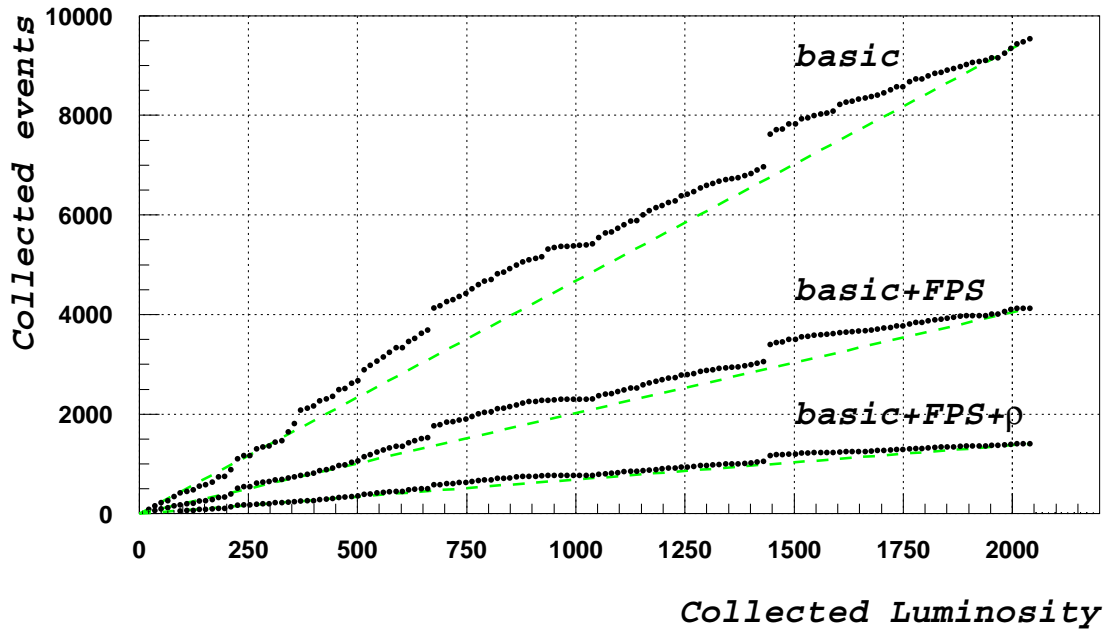


Figure 5.8: FPS operation luminosity versus number of collected events for three analysis stages II, III and IV as they are defined in table 5.2.

5.6 Photon Flux

In order to calculate the flux of quasi-real photons involved in γp interactions equation 2.17 is used. The integration limits of equation 2.17 are defined by the inelasticity and photon virtuality ranges. There is no information about the scattered electron in the current analysis and so the inelasticity and photon virtuality are calculated from the outgoing hadrons (see formulae 2.9, 2.10). The inelasticity range of the current analysis is $0.004 < y < 0.06$. The Q^2 range is estimated in the following two steps: 1) The lower limit Q^2_{min} is defined through the inelasticity value by formula 2.16. 2) The upper limit Q^2_{max} is determined by Monte Carlo. The full Monte Carlo sample is compared with the sample of rejected events with signals in SPACAL and/or LAr. (See selection criterion **iv** in table 5.2).

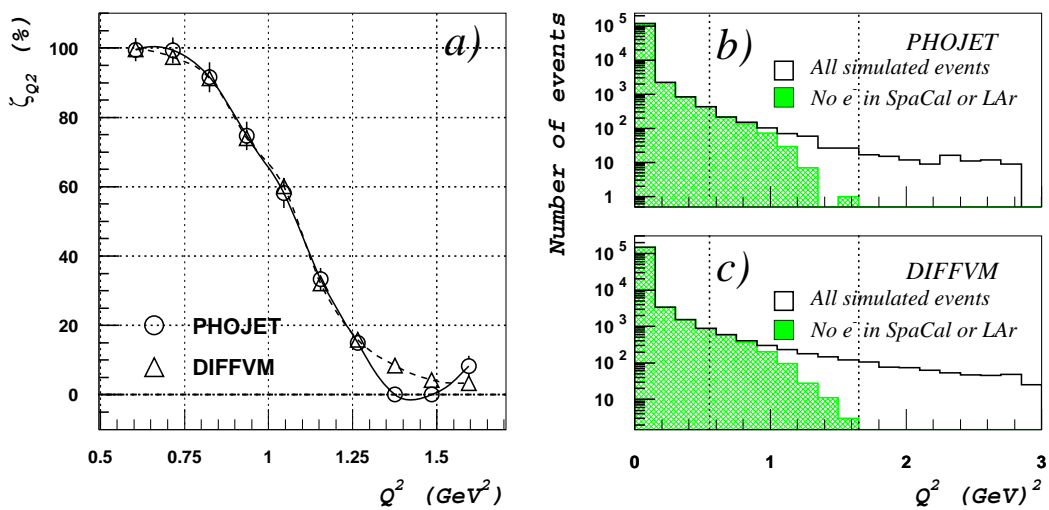


Figure 5.9: **a)** Efficiency in dependence on Q^2 for events with no electron seen in SPACAL or LAr. **b,c)** Q^2 distribution of all (open histogram) and the accepted (dashed histogram) events simulated by PHOJET and DIFFVM, respectively.

The Q^2 distributions of the events simulated by PHOJET and DIFFVM are presented in figure 5.9 b,c. The open histograms show the Q^2 distribution for *all events* simulated in $\gamma p \rightarrow \rho^0 p$ reaction. The shaded histograms show the Q^2 distribution only for those events which have no electron detected in the LAr or SpaCal. The rejection factor ζ_{Q^2} is defined as the ratio of the accepted events to all simulated events: $\zeta_{Q^2} = N_{no\ e}/N_{all}$. It indicates a decreasing probability to find a photoproduction event in the range $0.75 < Q^2_{max} < 1.5$. The ζ_{Q^2} distribution is presented in figure 5.9 a. The rejection factor ζ_{Q^2} shows the efficiency of the *veto criterion* of LAR or SpaCal defined by selection criterion **iv** from table 5.2. The Q^2_{max} value is the point where the criterion ζ_{Q^2} is about 60% (See Fig. 5.9 a). It is $Q^2_{max} = 1.0\ GeV^2$ with errors of $\pm_{0.25}^{0.50}\ GeV^2$.

The numerical integration of equation 2.17 over the inelasticity range $0.004 < y < 0.06$ and $Q^2_{max} = 1.0 \pm_{0.25}^{0.50}\ GeV^2$ results in a photon flux $\mathcal{F}_{\gamma/e} = 0.13866 \pm_{0.0017}^{0.0025}$.

Chapter 6

Monte Carlo and Data Treatment

This chapter is devoted to the Monte Carlo (MC) treatment and comparison of data with MC. The comparison is carried out for the kinematic reconstruction and measurement efficiency. As discussed in section 5.1 the kinematic reconstruction and trigger efficiency calculation in data are treated using the *sample 1* and *sample 2*, respectively as they are defined in section 5.1. The kinematic variables reconstructed in sample 1 and trigger efficiencies calculated in sample 2 are compared with MC. The reconstruction efficiency and acceptance are estimated by MC calculation.

To generate elastic ρ^0 -meson photoproduction processes in γp interactions the generators PHOJET [62] and DIFFVM [61] are used. The H1 simulation package H1SIM is used to simulate the H1 detector response and determine the measurement efficiency. The same reconstruction procedure of H1REC and the same set of selection criteria (described in section 5.2 and listed in table 5.2) are applied both to the data and MC event samples.

6.1 Quality of Monte Carlo Reconstruction

Correlation between Reconstructed and Generated Events

The MC reconstruction ability is investigated by comparison of the generated and reconstructed kinematic variables. The kinematic variables, dealt with here, are: 1) the CME of the γp system W ; 2) the invariant mass of the ρ^0 decay pions $M_{\pi\pi}$; 3) the proton transverse momentum $p_{t,p}$; 4) the ρ -meson transverse momentum $p_{t,\rho}$.

The scatter plots for the generated values versus MC reconstructed values of W , $M_{\pi\pi}$, $p_{t,p}$ and $p_{t,\rho}$ are shown in figure 6.1. The upper plots (Fig. 6.1 a-d) present the events which fulfill *basic* selection criteria listed in groups I–II of table 5.2. The lower plots (Fig. 6.1 e-h) present the events which fulfill *final* selection criteria of groups I–IV from table 5.2. Only the events which fulfill the *final* selection criteria are used further for comparison of data with MC and cross section calculation.

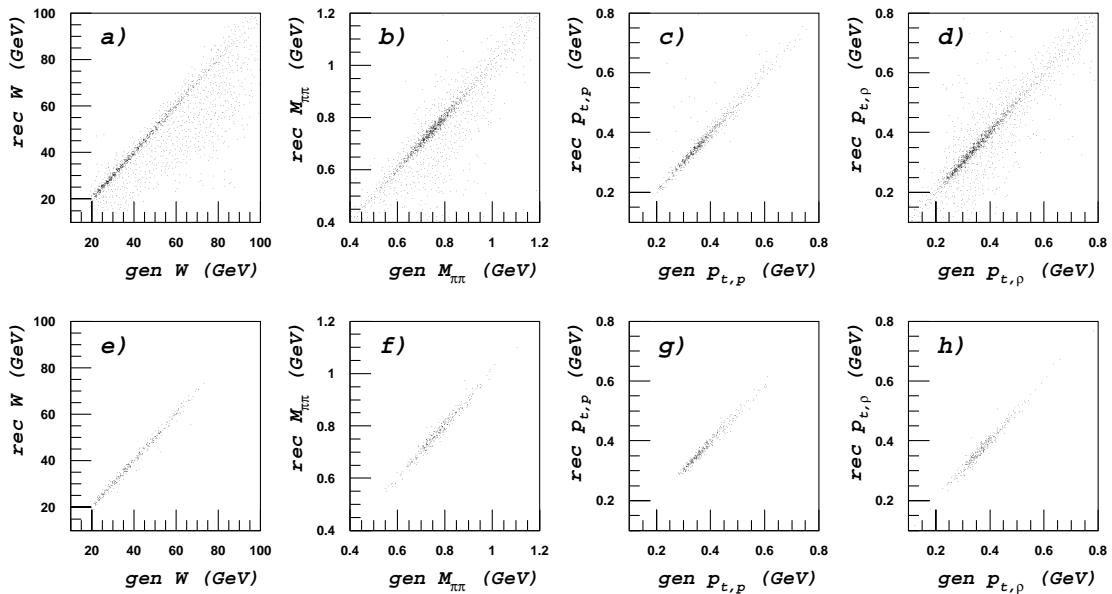


Figure 6.1: *Generated versus MC reconstructed kinematic variables. The events are collected with a-d) basic selection criteria of groups I–II, Tab. 5.2 and e-h) final selection criteria of groups I–IV, Tab. 5.2. a,e) CME of γp system W ; b,f) invariant mass of ρ decay pions $M_{\pi\pi}$; c,g) proton transverse momentum $p_{t,p}$; d,h) ρ -meson transverse momentum $p_{t,\rho}$.*

As one can see from figure 6.1 the application of the *final* selection criteria results with no crucial difference between generated and reconstructed values. The accuracy of the reconstruction procedure becomes visible from the MC resolution measurement.

Detector Resolution

In order to determine the resolution for the simulated kinematic variables the generated values \mathcal{V}_{gen} are compared to the MC reconstructed values \mathcal{V}_{rec} for those kinematic variables which are important in the current analysis. The absolute difference $\Delta\mathcal{V} = \mathcal{V}_{gen} - \mathcal{V}_{rec}$ and the relative difference $\delta\mathcal{V} = (\mathcal{V}_{gen} - \mathcal{V}_{rec})/\mathcal{V}_{gen}$ of generated and MC reconstructed values are shown in figure 6.2 for W , $M_{\pi\pi}$, $p_{t,p}$ and $p_{t,\rho}$. The mean values of the W difference histogram indicates the systematic shift of 100 MeV to lower values. The mean value $\langle\mathcal{V}\rangle$ and the root mean square deviation $RMS(\mathcal{V})$ of the histograms of figure 6.2 are listed in table 6.1. The values are presented for both MC reconstruction samples of the PHOJET and DIFFVM generators.

The relative values of RMS in table 6.1 is related to the fact that the γ virtuality is not directly measured in the current analysis and W is calculated from the variables of the outgoing hadrons (see Sec 2.1).

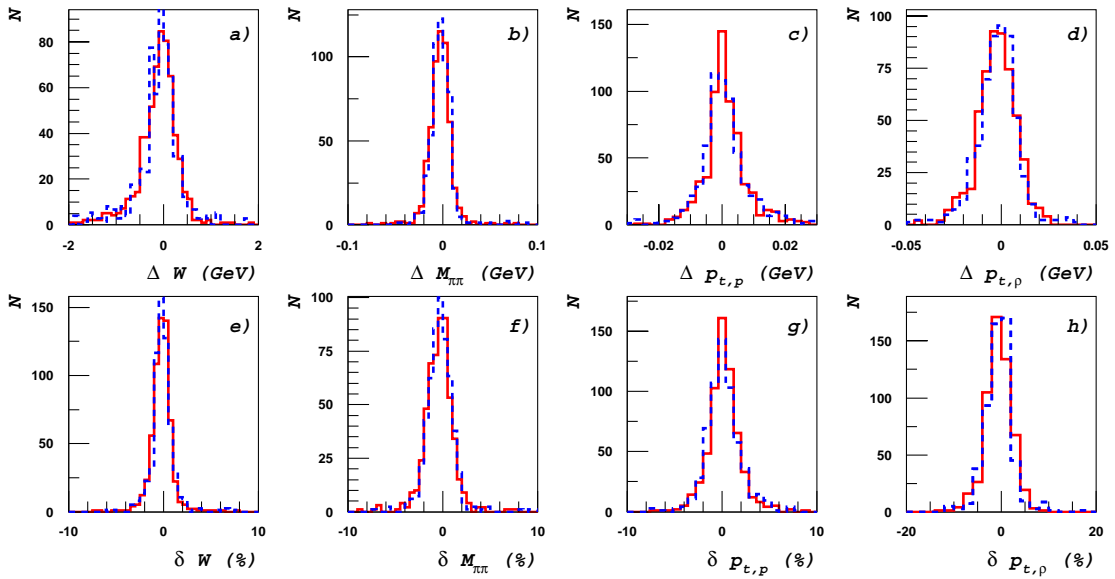


Figure 6.2: Histograms of the differences of generated and MC reconstructed kinematic variables W , $M_{\pi\pi}$, $p_{t,p}$ and $p_{t,\rho}$. **a–d)** the absolute difference of kinematic variables $\Delta\mathcal{V} = \mathcal{V}_{gen} - \mathcal{V}_{rec}$. **e–h)** relative difference of kinematic variables $\delta\mathcal{V} = (\mathcal{V}_{gen} - \mathcal{V}_{rec})/\mathcal{V}_{gen}$. Solid line denotes PHOJET distribution, dashed line – DIFFVM distribution. The mean values and root square deviations for histogrammed kinematic variables are listed in table 6.1.

PHOJET				
\mathcal{V}	$\langle\Delta\mathcal{V}\rangle$	RMS($\Delta\mathcal{V}$)	$\langle\delta\mathcal{V}\rangle$	RMS($\delta\mathcal{V}$)
	MeV	MeV	%	%
W	-115.3	428.4	0.22	1.20
$M_{\pi\pi}$	-3.0	12.6	0.41	1.56
$\mathbf{p}_{t,p}$	0.9	6.8	0.18	1.73
$\mathbf{p}_{t,\rho}$	-2.4	10.2	0.60	2.84
DIFFVM				
\mathcal{V}	$\langle\Delta\mathcal{V}\rangle$	RMS($\Delta\mathcal{V}$)	$\langle\delta\mathcal{V}\rangle$	RMS($\delta\mathcal{V}$)
	MeV	MeV	%	%
W	-110.3	465.4	0.13	1.25
$M_{\pi\pi}$	-1.9	12.7	0.29	1.53
$\mathbf{p}_{t,p}$	0.4	7.5	0.16	1.88
$\mathbf{p}_{t,\rho}$	-2.2	11.3	0.51	3.04

Table 6.1: Absolute difference $\Delta\mathcal{V} = \mathcal{V}_{gen} - \mathcal{V}_{rec}$ and relative difference $\delta\mathcal{V} = (\mathcal{V}_{gen} - \mathcal{V}_{rec})/\mathcal{V}_{gen}$ of generated \mathcal{V}_{gen} values and MC reconstructed values \mathcal{V}_{rec} for the kinematic variables W , $M_{\pi\pi}$, $p_{t,p}$ and $p_{t,\rho}$.

Migration

Due to the detector resolution the number of MC reconstructed events in a particular bin differs slightly from the number of generated events in this bin. This effect termed *migration* is a result of the systematic errors and reconstruction uncertainties. The migration is estimated bin by bin and expressed by the κ -factor. The κ -factor is given by the ratio:

$$\kappa = N_{rec}^{bin} / N_{gen}^{bin}$$

where N_{rec}^{bin} – is the number of reconstructed events in the bin and N_{gen}^{bin} – is the number of generated events in the same bin.

The ideal value of the κ -factor without bin migration is $\kappa = 1$. The dependence of the κ -factor on W , $M_{\pi\pi}$, $p_{t,p}$, and $p_{t,\rho}$ are shown in Fig. 6.3 for the PHOJET and DIFFVM event samples. The κ -factor depends on the bin width and event statistics. For the reason of low statistics at $W > 60$ GeV, $M_{\pi\pi} < 0.7$ GeV, $M_{\pi\pi} > 0.9$ GeV, $p_{t,p} > 0.4$ GeV and $p_{t,\rho} > 0.5$ GeV these bins have an enlarged width (see Fig. 6.3).

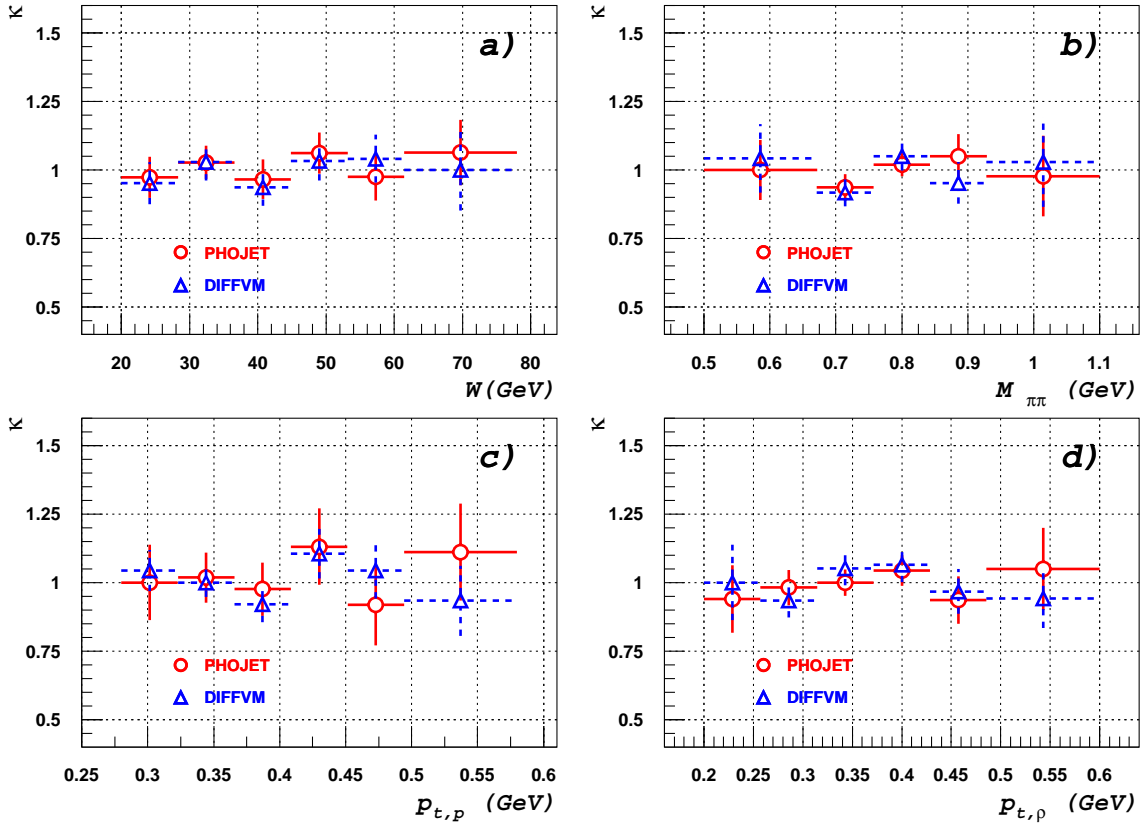


Figure 6.3: The distributions of the bin migration expressed by the factor $\kappa = N_{rec}^{bin} / N_{gen}^{bin}$ in dependence on the kinematic variables of: a) CME of γp system W ; b) invariant mass of two pions $M_{\pi\pi}$; c) proton transverse momentum $p_{t,p}$; d) ρ -meson transverse momentum $p_{t,\rho}$.

Purity

Due to migration not all events generated in a particular bin remain in this bin after reconstruction. The events remaining after the MC reconstruction are the *resident* events. The simulated events are termed resident in the bin if they are both generated and reconstructed in the same bin. The number of resident events is less than the number of all reconstructed events for the reason of bin migration.

The ratio of the bin *resident* events to the total number of reconstructed in this bin events is termed *purity*. The purity is expressed by the ξ -factor:

$$\xi = N_{rec}^{bin}(bin_{gen})/N_{rec}^{bin}$$

The purity in dependence on W , $M_{\pi\pi}$, $p_{t,p}$, and $p_{t,\rho}$ are shown in figure 6.4. The ξ -factor is correlated to the resolution of the kinematic variables presented in the histograms of figure 6.2.

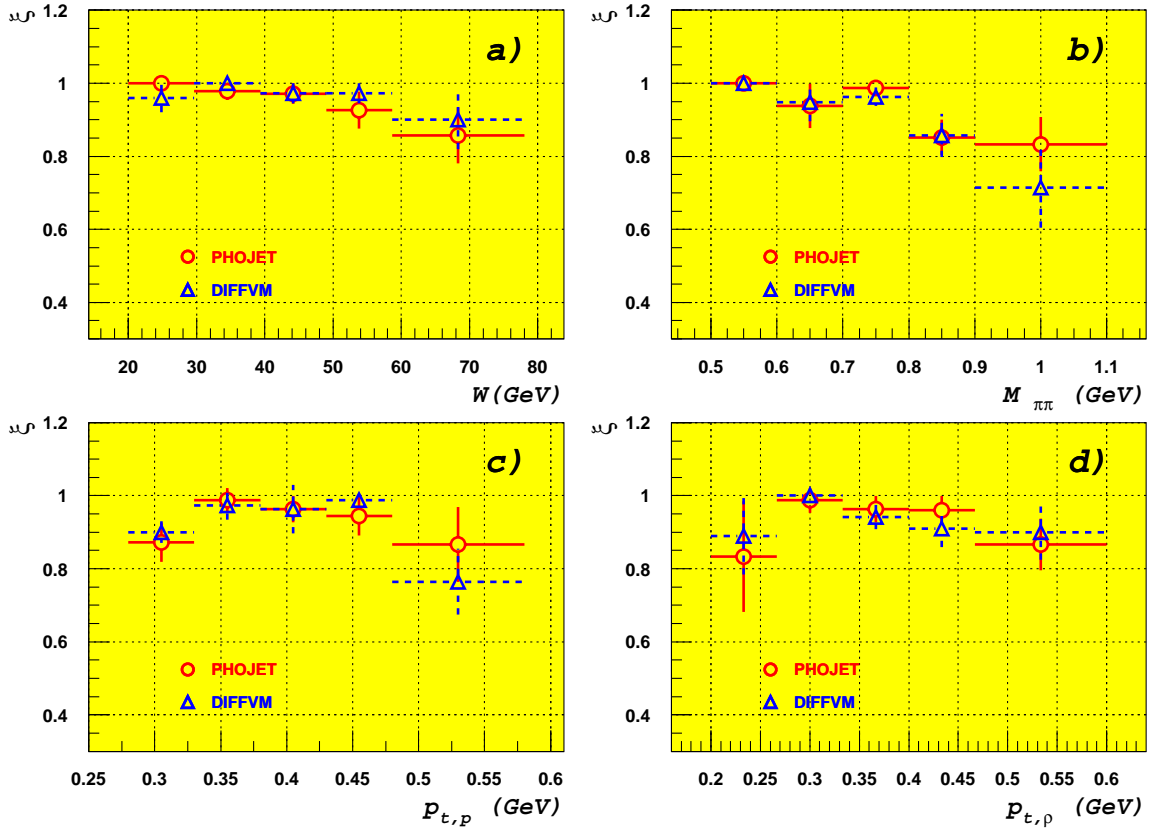


Figure 6.4: The distributions of the purity factor $\xi = N_{rec}^{bin}(bin_{gen})/N_{rec}^{bin}$ in dependence on the kinematic variables of: **a)** CME of γp system W ; **b)** invariant mass of two pions $M_{\pi\pi}$; **c)** proton transverse momentum $p_{t,p}$; **d)** ρ -meson transverse momentum $p_{t,\rho}$.

6.2 Comparison of Data and Monte Carlo

The MC events are simulated according to the experimental conditions and functionality of the H1 detector. The run dependent information has been also taken into account. The experimental conditions included in the simulation are: **1)** the number of collected events and measured luminosity in the corresponding run; **2)** the noise, measurement efficiency and acceptance of those detectors which are involved in the analysis; **3)** the beam tilts, angular dispersion of the beam and smearing of the interaction vertex; **4)** the H1 detector geometry and forward beam-line.

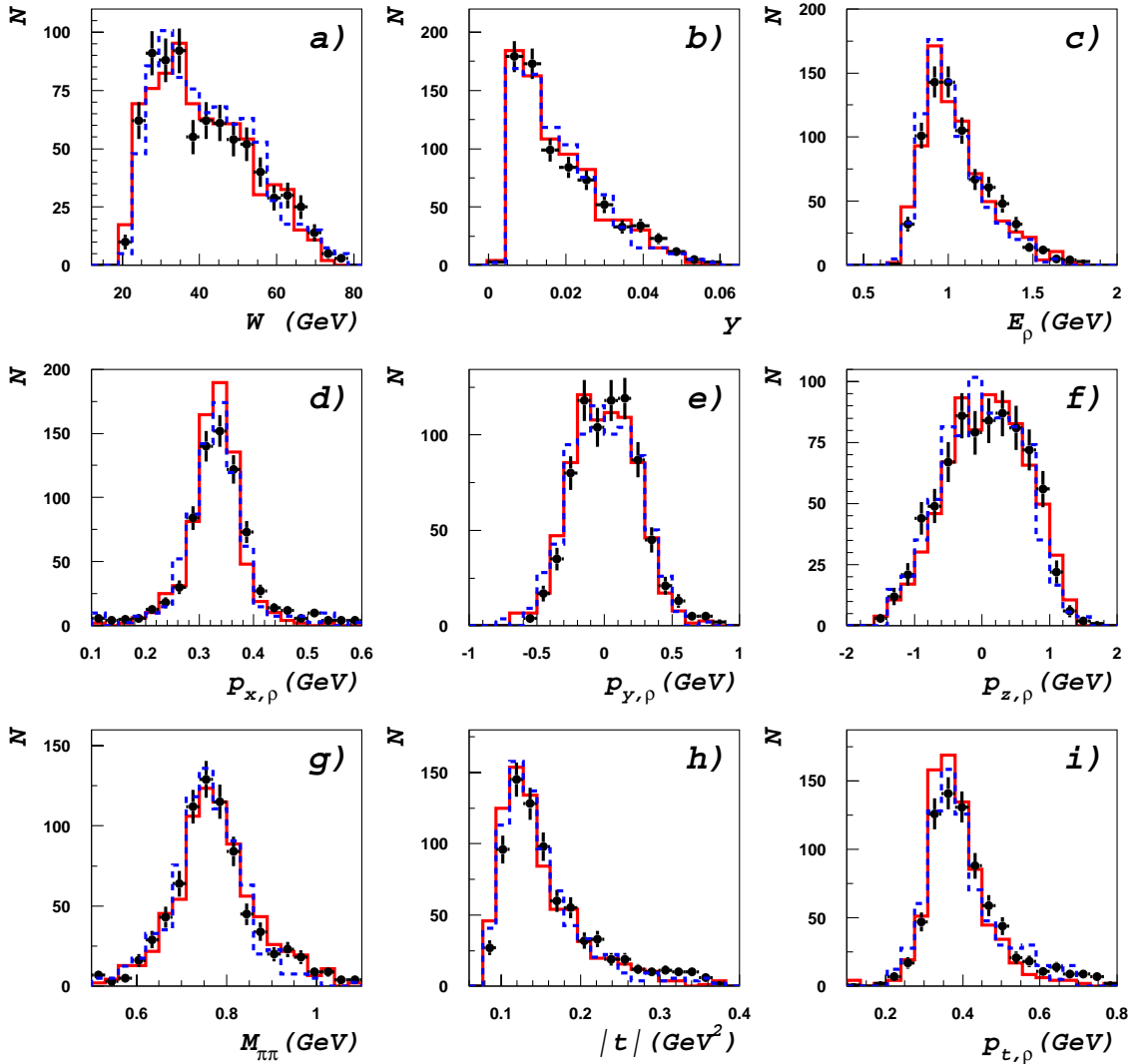


Figure 6.5: Control plots of relevant kinematic variables reconstructed in data and MC at final selection criteria of groups I–IV from table 5.2. Filled dots represent data, solid line – PHOJET, dashed line – DIFFVM.

In order to test how well MC simulation describes data, some distributions of kinematic variables of selected elastic ρ^0 -meson candidates in data are compared with corresponding distributions of kinematic variables in simulation. Figure 6.5 shows the reconstructed kinematic variables of the γp centre of mass energy W , the inelasticity y , the energy of the ρ^0 -meson E_ρ , the momentum of ρ^0 -meson in x, y, z projections $p_{x,\rho}, p_{y,\rho}, p_{z,\rho}$, the invariant mass of ρ^0 decay pions $M_{\pi\pi}$, the proton momentum transfer $|t|$ and the ρ^0 -meson transfer momentum $p_{t,\rho}$.

To check the conditions of ρ^0 -meson production in MC the angular distribution and the reference decay pion momentum in the ρ^0 decay system are compared to data. Figure 6.6 shows quite well agreement of both MC models with data. The angular distribution of the ρ^0 -meson production in ep scattering is described in section 2.5. The schematic view of ρ^0 -meson production and decay in ep scattering is presented in diagram 2.4. The ρ^0 decay angles in the CMS of the ρ -meson are defined by formulae 2.43.

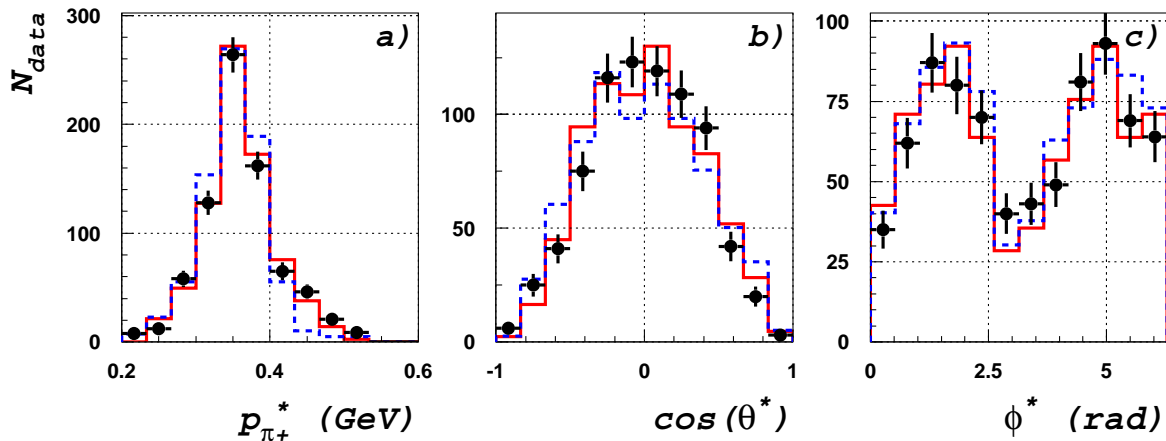


Figure 6.6: The distributions in the ρ^0 -meson CMS. **a)** The momentum and **b)** the polar angle of the decay π^+ -meson. **c)** The azimuthal angle of the ρ^0 decay system. The filled dots represent reconstructed data. The histograms represent MC reconstructed events: solid line – PHOJET, dashed line – DIFFVM.

The corresponding run dependent parameters are taken from the database in the simulation procedure in order to satisfy the experimental conditions. The number of simulated events for each selected run is proportional to the operation luminosity in this run. The operation luminosity is calculated by formula 5.4.

6.3 Momentum Balance

Simulated Momenta

The $e p$ scattering is simulated in the nominal interaction point and smeared in x, y and z coordinates according to the Gaussian distributions of data. The spacial parameters of the proton and electron beams used in the current analysis are presented in table 6.2. The comparison of the data with MC for the z -vertex distribution is shown in Fig. 5.4.

In addition the initial proton and electron momenta in x - and y -projections are simulated according to the smearing of the polar angle projections ($\vartheta_{x,p}$, $\vartheta_{y,p}$) and ($\vartheta_{x,e}$, $\vartheta_{y,e}$) of the induced proton and electron trajectories with respect to the nominal z -axis (see table 6.2). The polar angles ϑ_x and ϑ_y are also simulated according to Gaussian distributions.

Axis	Vertex offset [mm]	σ_{vertex} [mm]	σ_{ϑ} p-beam [μ rad]	σ_{ϑ} e-beam [μ rad]
x	-1.8	0.155	26.8	200.0
y	1.9	0.033	102.0	75.0
z	-6.1	113.0	–	–

Table 6.2: The beam parameters in x , y , z coordinates which were used in the simulation. The *vertex offset* – is the distance of the mean value of interaction point from the centre of the H1 coordinate system. The σ_{vertex} – is the width of the vertex Gaussian distribution. The σ_{ϑ} – is the polar angle width of the proton and electron beams.

Reconstructed Momenta

The momentum balance of the $\gamma p \rightarrow \rho^0 p$ process in the current analysis is checked by the difference of the scattered proton momentum measured in the FPS and the momentum of the ρ -meson measured in the CJC.

The ρ^0 -meson reconstructed in the CJC and the proton momentum reconstructed in the FPS satisfy the p_t -balance within the Gaussian fit width of 73 MeV, 57 MeV and 61 MeV for data, PHOJET and DIFFVM, respectively as one can see in figure 6.7 and in table 6.3. The width of the distributions indicate a smearing in reconstruction which affects the calculation of Q^2 , W or y from the variables of the outgoing hadrons (see Sec. 2.1). There is a small shift of mean values from zero in the distributions of figure 6.7. This shift indicates the accuracy of the calibration.

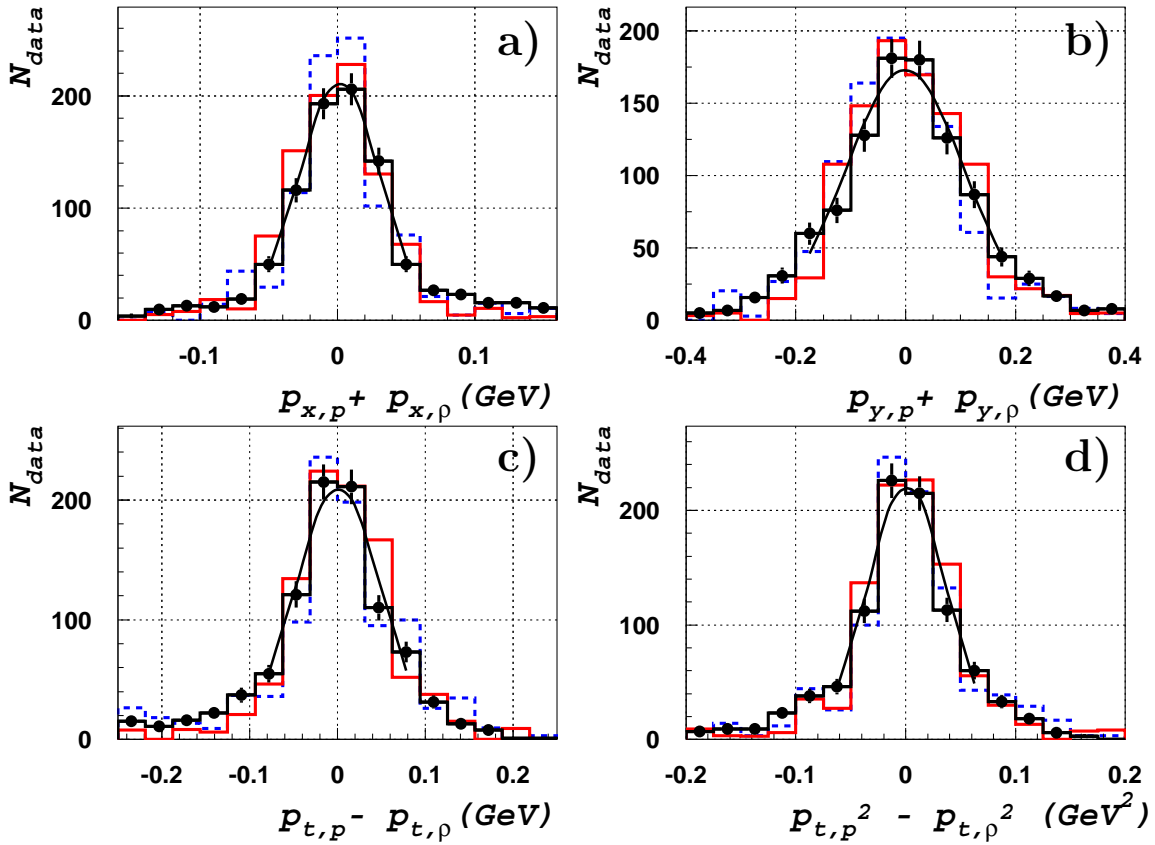


Figure 6.7: Momentum balance of the proton reconstructed in the FPS and ρ -meson reconstructed in the CJC: **a)** in x projection; **b)** in y projection; **c)** for transverse momenta $p_t = \sqrt{p_x^2 + p_y^2}$; **d)** for squared transverse momenta in supposition that $p_t^2 \approx |t|$. The filled dots, solid and dashed histograms denote the data, PHOJET and DIFFVM events, respectively. The Gaussian fit relates to the data.

\mathcal{V}	DATA		PHOJET		DIFFVM		Unit
	$\langle \mathcal{V} \rangle$	$RMS(\mathcal{V})$	$\langle \mathcal{V} \rangle$	$RMS(\mathcal{V})$	$\langle \mathcal{V} \rangle$	$RMS(\mathcal{V})$	
$\mathbf{p}_{x(\rho)} - \mathbf{p}_{x(p)}$	-3	48	5	37	4	40	MeV
$\mathbf{p}_{y(\rho)} - \mathbf{p}_{y(p)}$	-1	118	6	98	-1	95	MeV
$\mathbf{p}_{t(\rho)} - \mathbf{p}_{t(p)}$	5	73	-9	57	-3	61	MeV
$\mathbf{p}_{t(\rho)}^2 - \mathbf{p}_{t(p)}^2$	2	56	-6	46	-2	46	MeV ²

Table 6.3: Mean values $\langle \mathcal{V} \rangle$ and root mean square deviations $RMS(\mathcal{V})$ for the momentum balance of the proton measured in the FPS ($p_{x,p}$, $p_{y,p}$, $p_{t,p}$, $p_{t,p}^2$) and ρ -meson measured in the CJC ($p_{x,\rho}$, $p_{y,\rho}$, $p_{t,\rho}$, $p_{t,\rho}^2$). The histograms of the momentum balance distributions are presented in figure 6.7.

6.4 Measurement Efficiency

The full measurement efficiency ε of the elastic ρ -meson photoproduction in the current analysis contains two independent terms: the FPS efficiency and the efficiency of the central tracker (CT). Each term is a function of the geometrical acceptance, trigger efficiency and reconstruction efficiency discussed in this section.

6.4.1 Geometrical Acceptance

The geometrical acceptance \mathcal{A} is estimated by simulation of elastic ρ -meson production. It consists of the FPS acceptance – \mathcal{A}_{FPS} and acceptance of the CT – \mathcal{A}_{CT} .

1. The \mathcal{A}_{FPS} , restricted by the fiducial volume of the FPS horizontal stations, is a function of the beam profile and distance of the FPS detectors from the beam orbit.
2. The \mathcal{A}_{CT} is restricted by the central tracker size and fiducial polar angle shown in table 3.3. The polar angle range is fixed in the off-line reconstruction procedure to obtain a good measuring ability of charged particles in the CT.

6.4.2 Trigger Efficiency

The H1 trigger system and some details of the trigger definition are discussed in section 3.6. Here the trigger efficiencies estimated in data and MC for the selected event samples are presented. The trigger efficiency for the data is calculated using sample 2 as defined in section 5.1. As discussed in section 5.1 the sample 1 of ρ events is restricted by the positive decision of the subtrigger 107 (ST 107) defined by the expression 5.1. The efficiency values of the following trigger elements (TE) which constitute ST 107 are considered here:

- i) the FPS trigger tiles efficiency – ε_{FPS}^{trig} (TE 164 & TE 165) ;
- ii) the single track trigger efficiency in CT – $\varepsilon_{DCR\phi}^{trig}$ (TE 17) ;
- iii) the z -vertex cluster trigger efficiency – $\varepsilon_{zVtc}^{trig}$ (TE 29).

These trigger efficiencies, each of which is defined as a ratio of the number of reconstructed events with positive trigger decision to the number of all reconstructed events, are calculated in the following order:

- 1) The FPS trigger efficiency is calculated first.
- 2) The $DCR\phi$ trigger efficiency is calculated for a positive FPS trigger decision:

$$\varepsilon_{DCR\phi}^{trig} = \varepsilon_{DCR\phi}^{trig} \Big|_{(TE\ 164\ .and.\ TE\ 165)=1} \quad . \quad (6.1)$$

- 3) The z -vertex cluster trigger efficiency is calculated under the condition of both positive trigger decisions of the FPS and $DCR\phi$:

$$\varepsilon_{zVtc}^{trig} = \varepsilon_{zVtc}^{trig} \Big|_{(TE\ 164\ .and.\ TE\ 165\ .and.\ TE\ 17)=1} \quad . \quad (6.2)$$

FPS Trigger Tiles Efficiency

The FPS trigger decision is elaborated by the *trigger tiles* (see section 4.2) and written into the trigger bits TE 164 and TE 165 of the 80 *m* and 64 *m* horizontal stations, respectively. The decisions of TE 164 and TE 165 are independent from each other so that the value ε_{FPS}^{trig} contains two independent components: ε_{80H}^{trig} and ε_{64H}^{trig} which are the efficiencies of the 80 *m* and 64 *m* horizontal stations, respectively.

Each FPS horizontal station consists of four tiles. The trigger decision requests the signals from any combination of three tiles out of four (see Sec. 3.6). Thus, the trigger efficiency of the FPS station is calculated from a binomial distribution:

$$\begin{aligned} \varepsilon_{FPS\ station}^{trig} = & \epsilon_1 \cdot \epsilon_2 \cdot \epsilon_3 \cdot (1 - \epsilon_4) + \epsilon_2 \cdot \epsilon_3 \cdot \epsilon_4 \cdot (1 - \epsilon_1) + \\ & \epsilon_3 \cdot \epsilon_4 \cdot \epsilon_1 \cdot (1 - \epsilon_2) + \epsilon_4 \cdot \epsilon_1 \cdot \epsilon_2 \cdot (1 - \epsilon_3) + \\ & \epsilon_1 \cdot \epsilon_2 \cdot \epsilon_3 \cdot \epsilon_4 \end{aligned} \quad (6.3)$$

where the ϵ_i , ($i = 1, \dots, 4$) are termed *single tile* efficiencies.

In order to measure the *single tile* efficiency the unbiased event sample 2 is used counting single tile rates of those events which have a reconstructed proton in the FPS. The ratio of the single tile rate N_{tile} to the full number of events with reconstructed scattered proton N_{tracks} is defined as the *single tile* efficiency: $\epsilon_{tile} = N_{tile}/N_{tracks}$. The calculated *single tile* trigger efficiencies are presented for both horizontal stations in rows 1–4 of table 6.4. The last row of table 6.4 presents the trigger efficiency of the 80 *m* and 64 *m* stations calculated by expression 6.3.

N_{tile}	ε_{80H}^{trig} (%)	ε_{64H}^{trig} (%)
1	96.47	99.09
2	99.81	92.72
3	99.94	98.15
4	99.92	99.72
3/4	99.99	99.76

Table 6.4: The rows enumerated from 1 to 4 present the *single tiles* efficiency values of 80 *m* and 64 *m* horizontal stations. The last row typed in bold presents the trigger efficiency values of the FPS horizontal stations calculated by formula 6.3.

Trigger Efficiency of the Central Tracker

The trigger efficiency of the central tracker is termed DCR ϕ trigger efficiency $\varepsilon_{DCR\phi}^{trig}$. A brief overview of the DCR ϕ trigger is presented in section 3.6.2. In the current analysis the trigger element TE 17 named DCRPh_Ta is used. The trigger efficiency $\varepsilon_{DCR\phi}^{trig}$ is calculated under the condition of a positive decision of the FPS trigger.

The $DCR\phi$ trigger efficiency in data and MC is shown in figure 6.8 for the invariant mass $M_{\pi\pi}$ and the transverse momenta of the leading pion $p_{t,\pi\text{ lead}}$. According to the definition of selection criteria (see Sec. 5.2) the $p_{t,\pi\text{ lead}}$ is restricted to values above 0.45 GeV because of a large uncertainty of the trigger efficiency as shown in the left plot with the shaded background. The efficiency distributions of the polar and azimuthal angles are shown in figure 6.9.

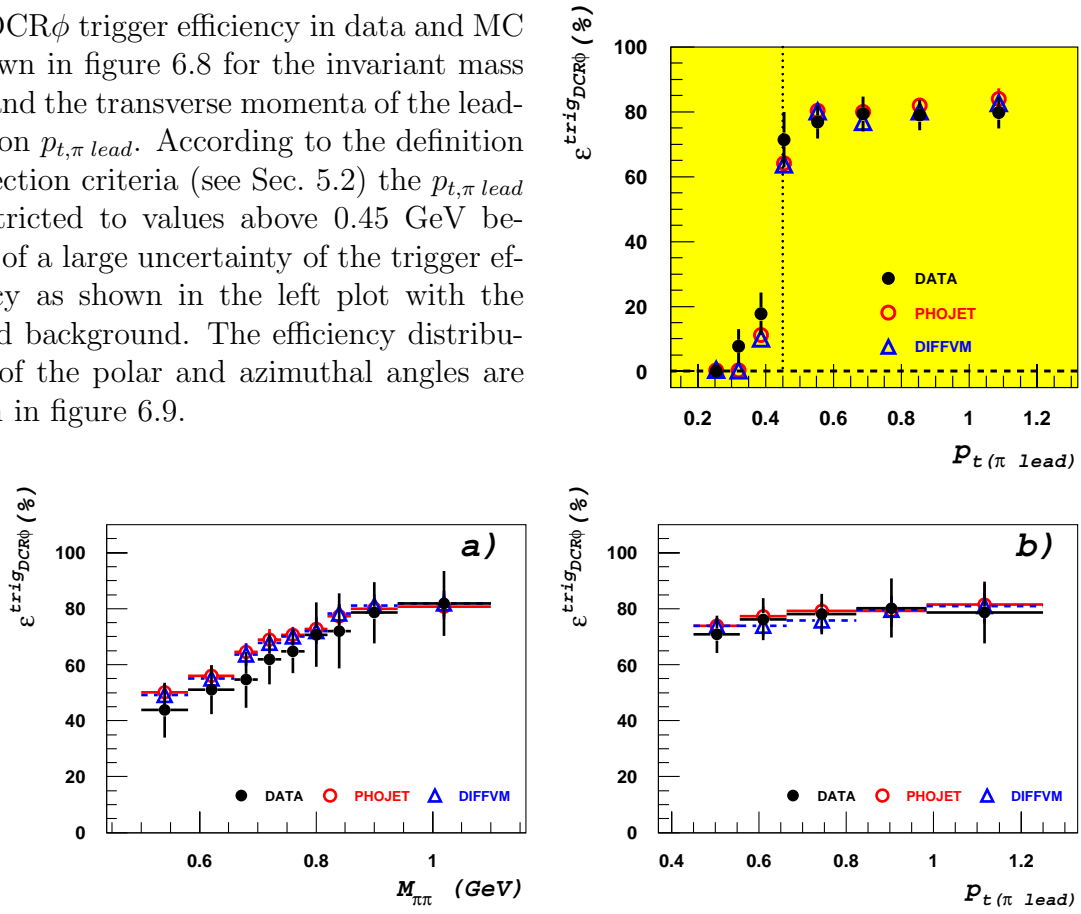


Figure 6.8: The $DCR\phi$ trigger efficiency in dependence on the effective mass $M_{\pi\pi}$ and the transverse momentum $p_{t,\pi\text{ lead}}$. The efficiency is calculated from data and MC.

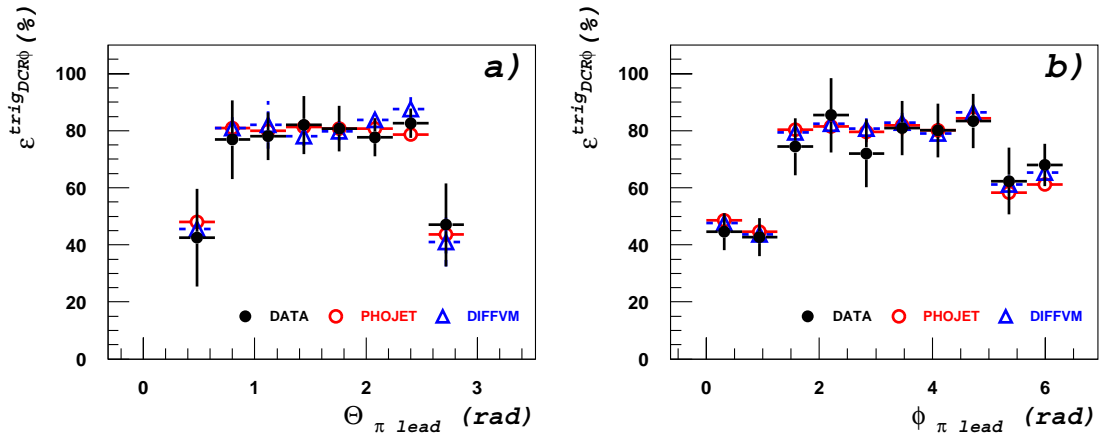


Figure 6.9: The $DCR\phi$ trigger efficiency in dependence on the polar angle $\Theta_{\pi\text{ lead}}$ and azimuthal angle $\phi_{\pi\text{ lead}}$ of the leading pion. The efficiency is calculated from data and MC.

Vertex Trigger Efficiency

The *vertex trigger* of the current analysis is covered by the *z-vertex cluster* trigger bit `zVtx_cls`, TE 29. The *z-vertex cluster* trigger is briefly discussed in section 3.6.1. The `zVtx_cls` trigger efficiency $\varepsilon_{zVtc}^{trig}$ is calculated under the condition of positive decisions of the FPS and $DCR\phi$ triggers (see expression 6.2).

The trigger efficiency $\varepsilon_{zVtc}^{trig}$ used in the current analysis is calculated using a cut on the transverse momentum of the leading pion $p_{t,\pi\text{ lead}} > 0.45$ GeV. The trigger efficiency $\varepsilon_{zVtc}^{trig}$ is presented in figure 6.10 in dependence on the effective mass $M_{\pi\pi}$ and transverse momentum $p_{t,\pi\text{ lead}}$. In figure 6.11 it is presented in dependence on the polar and azimuthal angles of the leading pion $\theta_{\pi\text{ lead}}^*$ and $\phi_{\pi\text{ lead}}^*$. These angles are measured in the ρ^0 -meson decay system as shown in scheme 2.4 and presented in figure 6.6.

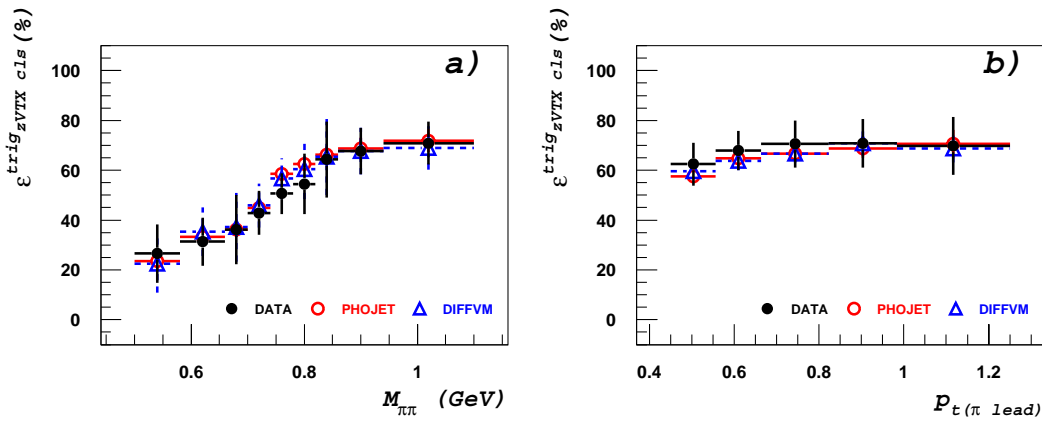


Figure 6.10: The z -vertex trigger efficiency in dependence on the effective mass $M_{\pi\pi}$ and transverse momentum $p_{t,\pi\text{ lead}}$ for data and MC of the PHOJET and DIFFVM generators.

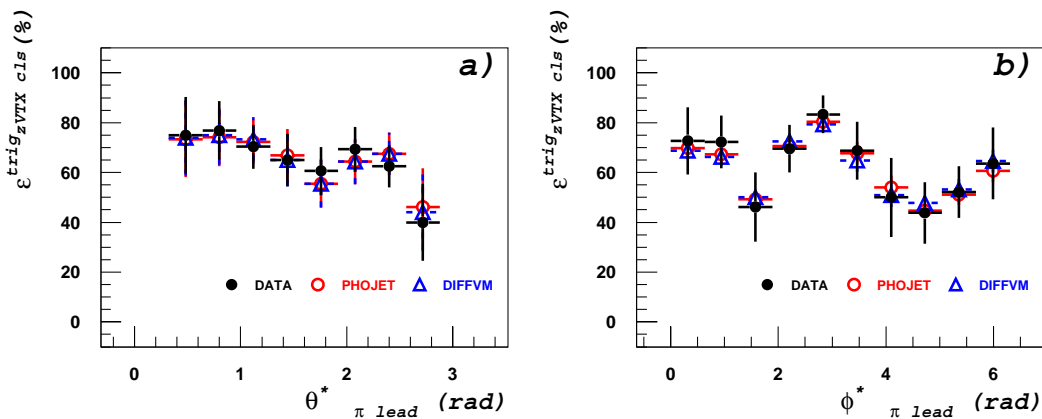


Figure 6.11: The z -vertex trigger efficiency in dependence on the polar and azimuthal angles $\theta_{\pi\text{ lead}}^*$ and $\phi_{\pi\text{ lead}}^*$ for data and MC of the PHOJET and DIFFVM generators.

6.4.3 Reconstruction Efficiency

The reconstruction efficiency ε^{rec} in the current analysis is calculated by MC under the conditions of the *basic* selection criteria **i–vi** which are defined in section 5.2 and listed in table 5.2.

The reconstruction efficiency ε^{rec} consists of the following contributions:

- i) the scattered proton reconstruction efficiency in the FPS – ε_{FPS}^{rec} ;
- ii) the ρ -meson reconstruction efficiency in the CJC – $\varepsilon_{\rho CJC}^{rec}$;
- iii) the z -vertex reconstruction efficiency – ε_{zVtx}^{rec} .

The reconstruction efficiencies ε_{FPS}^{rec} and $\varepsilon_{\rho CJC}^{rec}$ are independent from each other and from the vertex reconstruction efficiency ε_{zVtx}^{rec} . The reconstruction efficiencies ε_{FPS}^{rec} and $\varepsilon_{\rho CJC}^{rec}$ are calculated using the full MC event sample. The ε_{zVtx}^{rec} is calculated for the MC events which have reconstructed ρ -meson decay pion candidates:

$$\varepsilon_{zVtx}^{rec} = \varepsilon_{zVtx}^{rec} \Big|_{\text{reconstructed } \rho \text{ in the CJC}} \quad (6.4)$$

The ε_{zVtx}^{rec} is calculated for the z coordinate range of $-30 < z < 30 \text{ cm}$ (see Sec.5.2).

Reconstruction Efficiency of Scattered Proton in FPS

The FPS reconstruction efficiency takes into account: **a)** fiber detectors *single layer* efficiency (Fig. 6.12); **b)** proton track reconstruction efficiency (Fig. 6.13). The total FPS reconstruction efficiency used in the cross section calculation includes the reconstruction efficiency and acceptance. It is presented in figure 6.14.

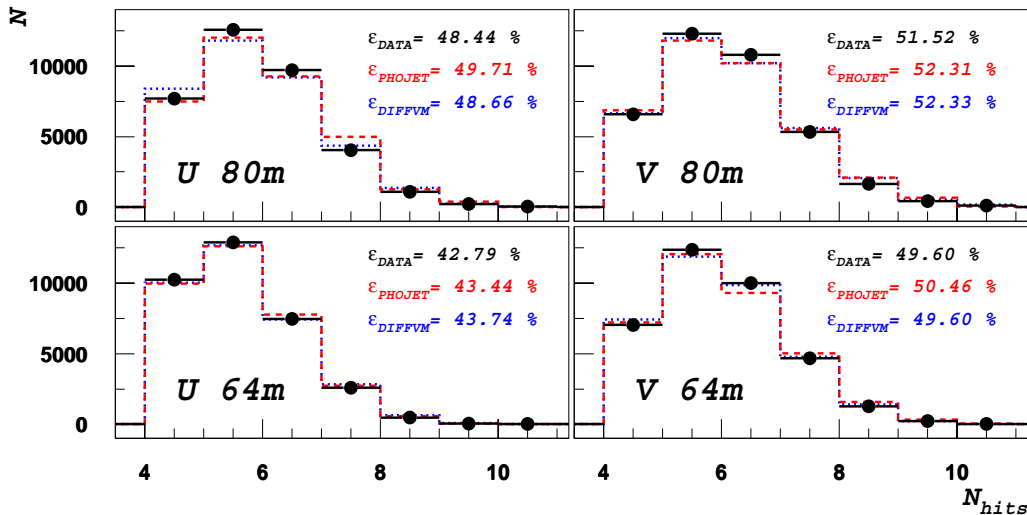


Figure 6.12: The multiplicity of fiber hits in the projections *U* and *V* (see Sec. 4.2). Each projection contains two subdetectors each with 5 layers. Binomial fits of the distributions are used to determine the mean single layer efficiency.

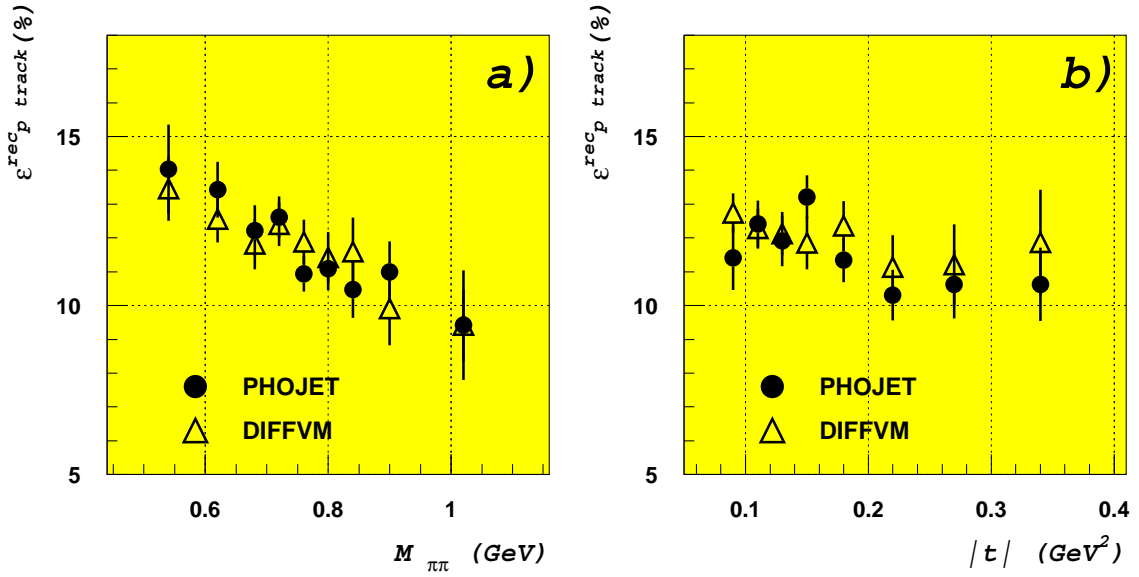


Figure 6.13: The proton track reconstruction efficiency in the horizontal stations in dependence on: **a)** invariant mass $M_{\pi\pi}$, **b)** proton momentum transfer $|t|$. The proton track reconstruction efficiency is calculated for the basic selection criteria **i–vi** from table 5.2.

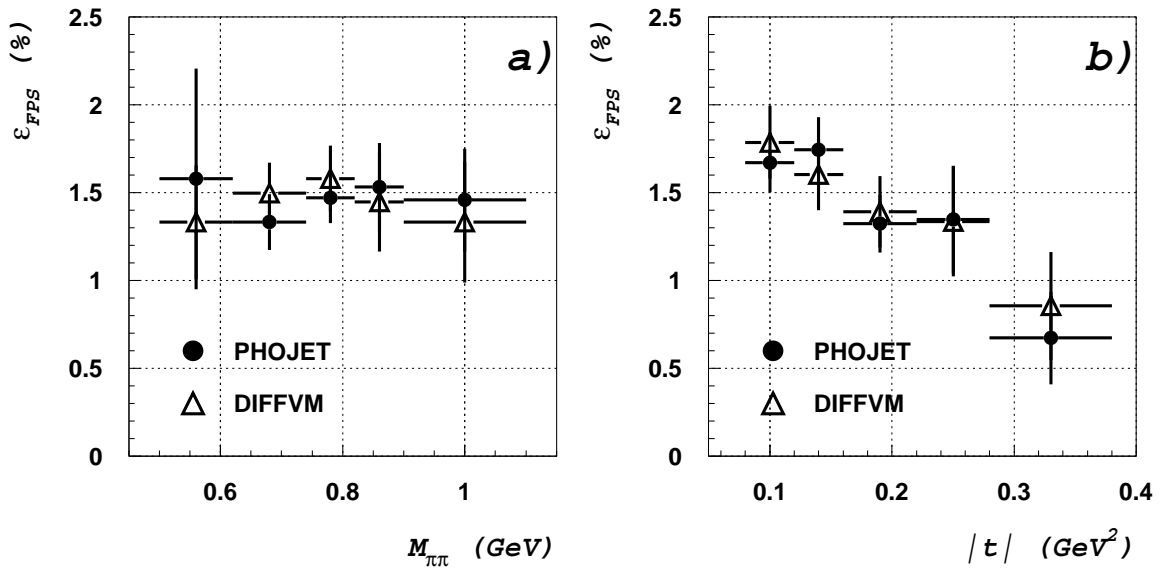


Figure 6.14: The total FPS reconstruction efficiency $\varepsilon_{FPS}^{\text{rec}}$ in dependence on: **a)** invariant mass $M_{\pi\pi}$, **b)** proton momentum transfer t .

Reconstruction Efficiency of the ρ -meson in CJC

The reconstruction efficiency of ρ^0 decay pions in the CJC is: $\varepsilon_{\rho}^{rec} = N_{\pi^+\pi^-} / N_{tot}$, where N_{tot} is number of the elastic ρ events simulated in central region of the H1 detector with the *basic* criteria **i–iv** of table 5.2 and $N_{\pi^+\pi^-}$ is the number of events with a couple of reconstructed pions in the CJC. The reconstruction efficiency in dependence on the invariant mass $M_{\pi\pi}$ and the momentum transfer $|t|$ is presented in figure 6.15.

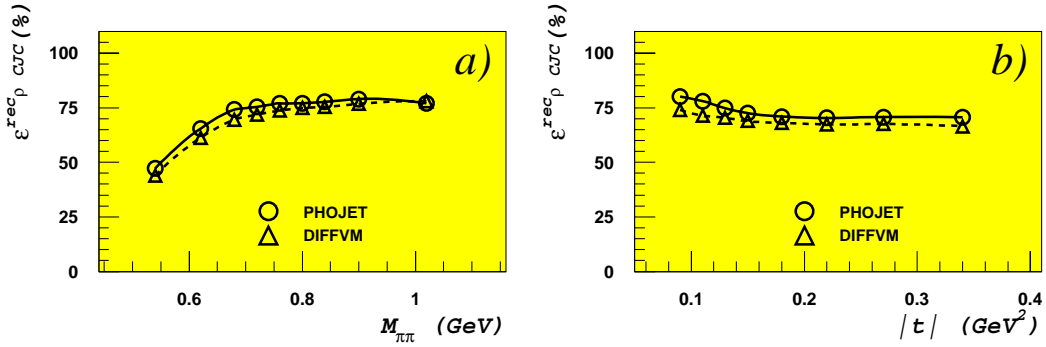


Figure 6.15: The reconstruction efficiency of ρ^0 -meson decay pions ε_{ρ}^{rec} in dependence on: **a)** the invariant mass $M_{\pi\pi}$, **b)** the proton momentum transfer $|t|$. It is calculated with the basic criteria **i–iv** of table 5.2.

Vertex Reconstruction Efficiency

The z -vertex reconstruction efficiency shows the fraction of events reconstructed in the range $-30 < z < 30$ cm (see Sec.5.2). The z -vertex reconstruction efficiency is calculated as: $\varepsilon_{zVtx}^{rec} = N_{zVtx} / N_{\pi^+\pi^-}$. Here $N_{\pi^+\pi^-}$ is the total number of reconstructed ρ^0 events and N_{zVtx} is the number of events with a reconstructed vertex which is inside the interval of ± 30 cm around the nominal ep interaction point. The ε_{zVtx}^{rec} distributions in dependence on $M_{\pi\pi}$ and $|t|$ are shown in figure 6.16.

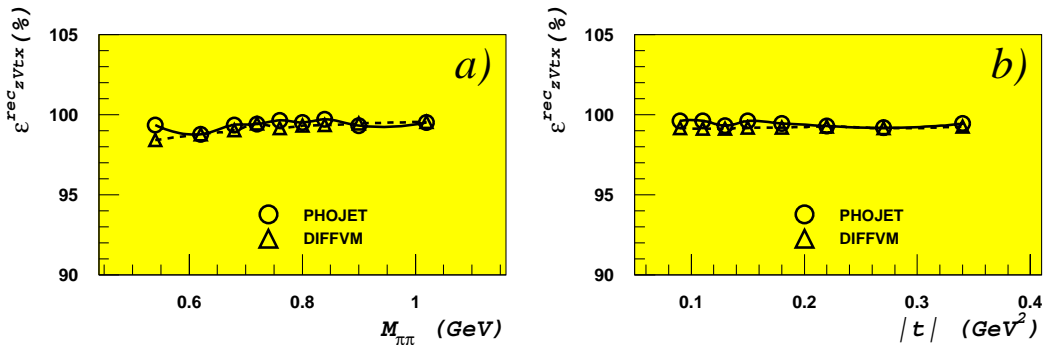


Figure 6.16: The z -vertex reconstruction efficiency of ρ^0 -meson events ε_{zVtx}^{rec} in dependence on: **a)** the invariant mass $M_{\pi\pi}$, **b)** the proton momentum transfer $|t|$. It is calculated with the basic criteria **i–v** of table 5.2.

6.5 Systematic Errors

The current analysis contains systematic errors from the following sources: **1)** luminosity measurement; **2)** photon flux calculation; **3)** beam gas background; **4)** central tracker measurement ability; **5)** scattered proton measurement in FPS.

The systematic errors are listed in table 6.5. The total systematic error used in cross section calculation is 13 %.

	Analysis step systematics	Uncertainty
1	Luminosity	1.3 %
	Total luminosity \oplus Satellite corrections	1.1 \oplus 0.7 %
2	Photon flux calculation	1.6 %
3	Beam gas background	0.1 %
4	Central Tracker measurement ability	7.6 %
4	trigger \oplus reconstruction efficiency	6.5 \oplus 4.0 %
5	Scattered proton measurement in FPS	9.6 %
	FPS reconstruction ability \oplus FPS acceptance	5.8 \oplus 7.7 %
Σ	Total systematic error	13.0 %

Table 6.5: Systematic errors for the elastic ρ^0 -meson photoproduction measurement.

(1) Luminosity Measurement

The luminosity measurement results with a systematic error of 1.3%. It consists of:

- a) the *total luminosity* measurement error of 1.1 %;
- b) the *satellite corrections* error of 0.7 %.

(2) Photon Flux Calculation

The error of the photon flux calculation results from the integration limits of the Weizsäcker-Williams approximation (see Eq. 2.17). Because no information about the scattered electron is available in the analyzed sample, the inelasticity is calculated from the variables of the outgoing hadrons (see Eq. 2.9) to be in the range $0.004 < y < 0.06$. The lower limit of Q^2 is calculated by formula 2.16. The upper limit of Q^2 is estimated as it is discussed in section 5.6. The photon flux is calculated with a systematic uncertainty of 1.6 %.

(3) Beam Gas Background

The beam gas background is estimated by the counting rates of the FPS station trigger tiles. The rates are counted in five time slices where only one of them is the slice of the $e p$ interaction. The rates in the $e p$ interaction slice are compared with rates in the other slices to estimate the level of beam gas contamination. In the current analysis each horizontal station is triggered by a fraction of 0.3 % of events from beam gas interaction. The coincidence of both horizontal stations results in a contribution of 0.1 %.

(4) Measurement of the ρ^0 in Central Tracker

The systematic uncertainty of the ρ^0 -meson measurement in the central tracker consists of trigger and reconstruction uncertainties. The trigger efficiency systematic uncertainty of 6.5 % is estimated by the uncertainty of the decay pion transverse momentum. The event kinematics requires two tracks in the central region and no other track either in forward, backward or central parts of H1. The systematic error of the ρ^0 -meson reconstruction in the Central Tracker is 4 %. The total systematic uncertainty of Central Tracker is 7.6 %.

(5) Measurement of Scattered Proton in FPS

The systematic error of the scattered proton measurement consists of the FPS acceptance and track reconstruction uncertainties. The systematic error of the FPS acceptance is estimated by the variation of the FPS positions (see Sec. 4.3). The calculated uncertainty of the FPS acceptance is 7.7 %.

The scattered proton momentum value, measured in the FPS, is reconstructed with a systematic uncertainty of 5.8 %. The systematic error of the momentum reconstruction was estimated using the leading proton transverse momentum smearing of $p_t = \pm 10$ MeV. The overall uncertainty in FPS calculated as the quadratic sum of the FPS acceptance and momentum reconstruction uncertainties is 9.6%.

Chapter 7

Elastic ρ^0 Cross Section

In this chapter the cross section of the elastic ρ^0 -meson photoproduction $\sigma_{\gamma p \rightarrow \rho^0 p}$ is presented. The cross section measured in the current analysis is based on event sample 1 discussed in chapters 5 and 6.

The differential cross sections in dependence on the invariant mass of the ρ^0 -meson decay pions $d\sigma/dM_{\pi\pi}$ and in dependence on the proton momentum transfer $d\sigma/d|t|$ are presented in three intervals of the γp centre of mass energy W . In addition the $d\sigma/dM_{\pi\pi}$ in three intervals of $|t|$ and the $d\sigma/d|t|$ in three intervals of $M_{\pi\pi}$ are presented. The measured differential cross section is restricted to the kinematic region $0.5 < M_{\pi\pi} < 1.1 \text{ GeV}$ and $0.08 < |t| < 0.38 \text{ GeV}^2$. The measured cross section, extrapolated to the full kinematic region, has been compared with previous measurements.

Differential Cross Section

In this section both the invariant mass $M_{\pi\pi}$ and proton momentum transfer $|t|$ are denoted as \aleph . The differential cross-section in dependence on \aleph is calculated in bins of width $\Delta\aleph$ by the following formula:

$$\frac{d\sigma_{\gamma p \rightarrow \rho^0 p}}{d\aleph} = \frac{N_\rho}{\mathcal{F}_{\gamma/e} \cdot \mathcal{L} \cdot \varepsilon_{FPS} \cdot \varepsilon_{CT}} \cdot \frac{1}{\Delta\aleph} \quad . \quad (7.1)$$

Here

N_ρ – is the number of the selected elastic ρ^0 events in one bin of width $\Delta\aleph$. The final sample described in section 5.2 results with $N = 1030$ of ρ^0 -meson candidates. The background rate estimated in Monte Carlo simulation is used to calculate the background contribution N_{bkg} in the data. This background contribution is used to determine the true number of observed ρ^0 -mesons by: $N_\rho = N - N_{bkg} = 943$.

ε_{FPS} , ε_{CT} – are the bin dependent measurement efficiencies of the FPS and CT respectively, calculated in the range of $\Delta\aleph$ as described in section 6.4.

$\mathcal{F}_{\gamma/e}$ – is the photon flux from induced electrons which is calculated by numerical integration of the Weizsäcker-Williams approximation using formula 2.17. The calculated photon flux (see Sec. 5.6) for the investigated kinematic region of $0.004 < y < 0.06$ and $Q_{max}^2 = 1 \pm_{0.25}^{0.50} \text{ GeV}^2$ is $\mathcal{F}_{\gamma/e} = 0.13866 \pm_{0.0017}^{0.0025}$.

\mathcal{L} – denotes the operation luminosity integrated over the analyzed data taking period (see Eq. 5.4) with respect to the detector status and the pre-scale of subtrigger 107 as described in section 5.5. The operation luminosity value for the analyzed event sample is $\mathcal{L} = 2039.68 \text{ nb}^{-1}$.

7.1 Distribution by the Invariant Mass

7.1.1 Uncorrected Mass Spectrum

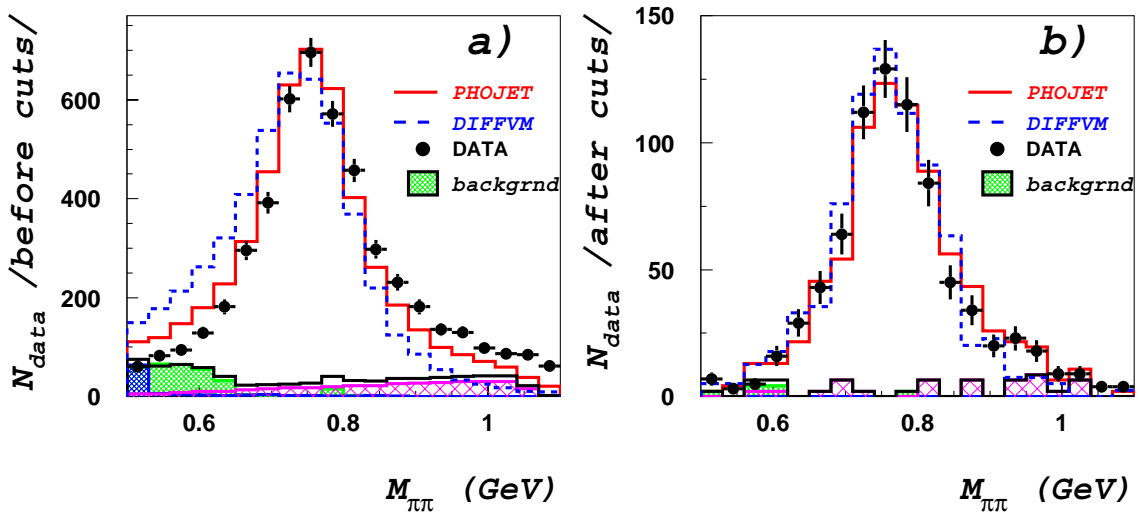


Figure 7.1: The invariant mass distributions of data and MC events uncorrected for the measurement efficiency. **a)** Basic sample. **b)** Final sample. The solid and dashed lines denote the spectra simulated by PHOJET and DIFFVM, respectively. The filled dots represent the data. The shaded and cross-hatched histograms in the bottom of mass spectra indicate the background distributions.

The invariant mass distributions of two ρ^0 -meson decay pions measured in the H1 central tracker are presented in figure 7.1. These distributions are uncorrected for the measurement efficiency. Figures 7.1a and 7.1b show the comparison of data to MC for the mass spectra before (basic sample, groups I–II, table 5.2) and after (final sample, groups I–IV, table 5.2) the measurement of the proton in the FPS and analysis selection criteria application. The selection criteria are described in section 5.2.

The comparison of figure 7.1b with 7.1a shows a significant reduction in statistics and shape of the invariant mass distribution. The MC distributions are normalized to the number of events in the data. The data is represented by dots. The solid and dashed lines denote the spectra simulated by PHOJET and DIFFVM, respectively.

As one can see in figure 7.1a the distributions for DIFFVM and PHOJET are different in the low mass region before selection criteria application. This difference is explained by the different generation models (see section 2.4) applied in PHOJET and DIFFVM. The PHOJET generator uses a multiple Pomeron exchange model which includes absorptive corrections. In contrast to PHOJET, the DIFFVM generator use single Pomeron exchange. Because the main contribution of absorptive corrections comes from the low masses diffractive background the DIFFVM distribution for low masses is enhanced in comparison with PHOJET distribution. After the application of final selection criteria both MC distributions are in agreement with each other and with data as shown in figure 7.1b. The background distributions shown as shaded and cross-hatched histograms in figure 7.1 are discussed in section 5.3.

The PHOJET distribution in figure 7.1 contains reconstructed elastic ρ^0 -mesons together with the physical background contributions, discussed in section 5.3. The deep shaded histograms of figure 7.1 show the rest of ω and ϕ mesons and slightly shaded histogram represents non-resonant $\pi^+\pi^-$ events reconstructed in PHOJET. The DIFFVM distribution of figure 7.1 contains only elastic ρ -mesons without background.

7.1.2 Differential Cross Section $d\sigma/dM_{\pi\pi}$

The following functional form is applied to fit the differential cross section $d\sigma/dM_{\pi\pi}$ of the ρ^0 and $\pi^+\pi^-$ production in γp interaction:

$$\frac{d\sigma_{\gamma p \rightarrow \rho^0 p}}{dM_{\pi\pi}} \propto \left| A \cdot \frac{\sqrt{M_{\pi\pi} m_\rho \Gamma_\rho(M_{\pi\pi})}}{M_{\pi\pi}^2 - m_\rho^2 + im_\rho \Gamma_\rho(M_{\pi\pi})} + B \right|^2 . \quad (7.2)$$

Here A and B are the *resonant* and *non-resonant* amplitudes, respectively. A pure resonance state ($B = 0$) is described by the relativistic Breit-Wigner function $BW_\rho(M_{\pi\pi})$ which is expressed by the formula:

$$BW_\rho(M_{\pi\pi}) = \frac{M_{\pi\pi} m_\rho \Gamma_\rho(M_{\pi\pi})}{(M_{\pi\pi}^2 - m_\rho^2)^2 + m_\rho^2 \Gamma_\rho^2(M_{\pi\pi})} . \quad (7.3)$$

Here m_ρ is the nominal value of the ρ^0 mass and $\Gamma_\rho(M_{\pi\pi})$ is the momentum dependent width of the ρ^0 resonance. The width $\Gamma_\rho(M_{\pi\pi})$ has been parametrized in the following way:

$$\Gamma_\rho(M_{\pi\pi}) = \Gamma_0 \left(\frac{p^*}{p_0^*} \right)^3 \frac{2}{1 + (p^*/p_0^*)^2} , \quad (7.4)$$

as a function of the pion momentum p^* in the $\pi^+\pi^-$ rest frame (see Fig. 2.4). The momentum p_0^* is the pion momentum at the nominal ρ -meson mass m_ρ and Γ_0 is the nonrelativistic width of the ρ^0 state.

The experimental values of the $d\sigma/dM_{\pi\pi}$ distribution are skewed to the Breit-Wigner resonant fitting profile. The low mass values are enhanced and the mass peak is shifted to the low mass region. This effect is explained by the interference between

the resonant ρ^0 and non-resonant $\pi^+\pi^-$ Drell type background [84, 85]. Thus, the skewing of the experimental data indicates a non-zero B amplitude of equation 7.2. In what follows, two parametrization schemes with a non-zero B term are discussed. These schemes are used in current analysis to fit the ρ^0 mass distribution.

Ross-Stodolsky Parametrization

The phenomenological parametrization suggested by M.Ross and L.Stodolsky [86] use the skewing factor $(M_\rho/M_{\pi\pi})^n$ multiplied by the relativistic Breit-Wigner function:

$$\frac{d\sigma(M_{\pi\pi})}{dM_{\pi\pi}} = f_\rho BW_\rho(M_{\pi\pi}) \left(\frac{m_\rho}{M_{\pi\pi}} \right)^{\mathbf{n}} + f_{bkg} \quad . \quad (7.5)$$

The background term f_{bkg} is parametrized using the pion mass m_π in the following way:

$$f_{bkg} = \alpha_1 (M_{\pi\pi} - 2m_\pi)^{\alpha_2} e^{-\alpha_3 M_{\pi\pi}} \quad . \quad (7.6)$$

The function of formula 7.5 is fitted to the measured mass distribution. The result termed Ross-Stodolsky fit is shown in figure 7.2a. The skewing parameter \mathbf{n} indicates the difference between Ross-Stodolsky and pure Breit-Wigner fits. There is no difference in case of $\mathbf{n} = 0$. The positive value of the \mathbf{n} parameter provides an enhancement of the low mass side and suppress the high mass side. The skewing parameter \mathbf{n} is a function of the proton momentum transfer $|t|$ as one can see in figure 7.4.

Söding Parametrization

In the same year in parallel to M.Ross and L.Stodolsky the skewing was discussed by P.Söding [35] in terms of the resonant and non-resonant $\pi^+\pi^-$ interference. There was found that the interference of the ρ^0 photoproduction with Drell-type background produce a shift of the ρ^0 mass distribution of about $25 MeV$. To describe this effect an additional term $\mathbf{I}(M_{\pi\pi})$ can be introduced to the Breit-Wigner function $BW(M_{\pi\pi})$ in order to estimate the contribution of the non-resonant $\pi^+\pi^-$ production:

$$\frac{d\sigma(M_{\pi\pi})}{dM_{\pi\pi}} = f_\rho BW_\rho(M_{\pi\pi}) + f_I \mathbf{I}(M_{\pi\pi}) + f_{bkg} \quad , \quad (7.7)$$

where f_I is the *relative normalization constant* of the interference contribution which is given by the following relation:

$$\mathbf{I}(M_{\pi\pi}) = \frac{m_\rho^2 - M_{\pi\pi}^2}{(m_\rho^2 - M_{\pi\pi}^2)^2 + m_\rho^2 \Gamma^2(M_{\pi\pi})} \quad . \quad (7.8)$$

Here $\Gamma(M_{\pi\pi})$ is a relativistic momentum dependent width (see Eq. 7.4). The interference term $\mathbf{I}(M_{\pi\pi})$ is related to the form-factor expressed by formula 2.24.

The background term f_{bkg} has a linear behavior with a very low tilt and can be considered as constant. The fit of the measured distribution with the Söding parametrization described by formula 7.7 is presented in figure 7.2b.

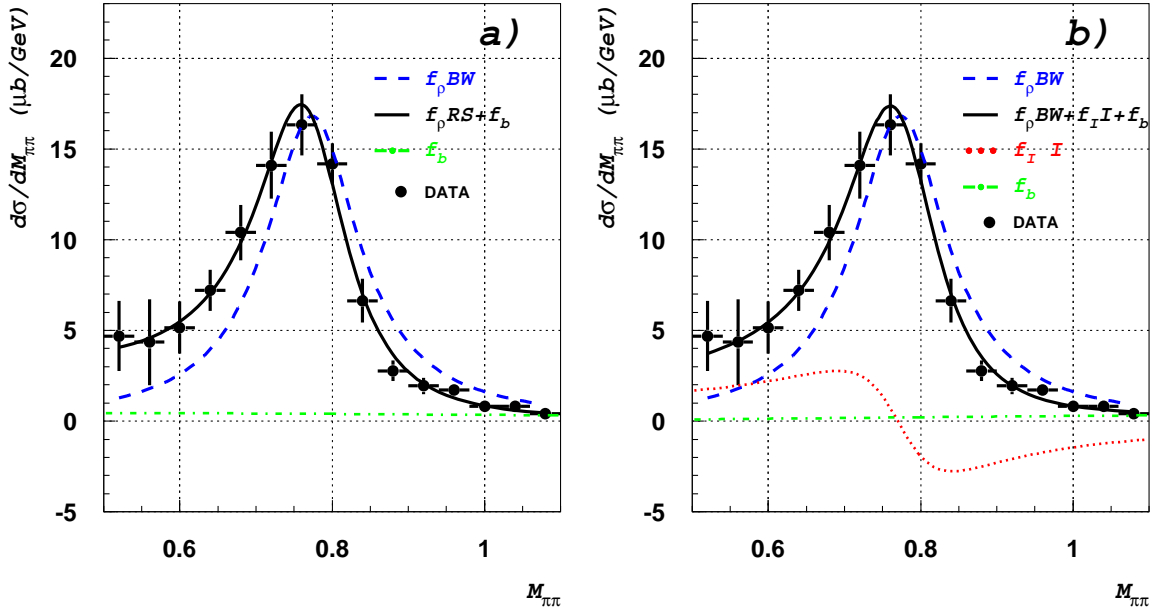


Figure 7.2: The differential cross section distributions in dependence on the invariant mass of the two pions $M_{\pi\pi}$. The dots present the cross section calculated by formula 7.1. **a)** The Ross-Stodolsky fit (solid curve) and the relativistic Breit-Wigner fit (dashed curve); **b)** The Söding fit (solid curve) and relativistic Breit-Wigner fit (dashed curve). The curve of the Söding interference term $f_I \cdot \mathbf{I}(M_{\pi\pi})$ defined by equation 7.8 is plotted as dotted line. The interference term $\mathbf{I}(M_{\pi\pi})$ has positive values for the low mass side and negative values for the high mass side.

7.1.3 Cross Section $d\sigma/dM_{\pi\pi}$ in $|t|$ and W Intervals

In order to investigate the differential cross section $d\sigma/dM_{\pi\pi}$ dependence on invariant mass $M_{\pi\pi}$, in the measured kinematic region, the analyzed data sample is subdivided into the $|t|$ and W intervals as discussed in this section.

Cross Section $d\sigma/dM_{\pi\pi}$ in $|t|$ Intervals

The cross section $d\sigma/dM_{\pi\pi}$ measured in three intervals of the proton momentum transfer $|t|$ is shown in figure 7.3. Each column of figure 7.3 corresponds to the $|t|$ intervals listed in tables 7.1, 7.2. The intervals are chosen to get a reasonable statistics in each $|t|$ interval.

The upper and lower plots in figure 7.3 present the Ross-Stodolsky and Söding parametrizations, respectively (solid curve) with the Breit-Wigner fit (dashed curve). The skewing parameter \mathbf{n} of the Ross-Stodolsky parametrization is decreasing with increasing $|t|$ as shown in figure 7.4a. The skewing dynamics of the Söding parametrization is shown in figure 7.4b.

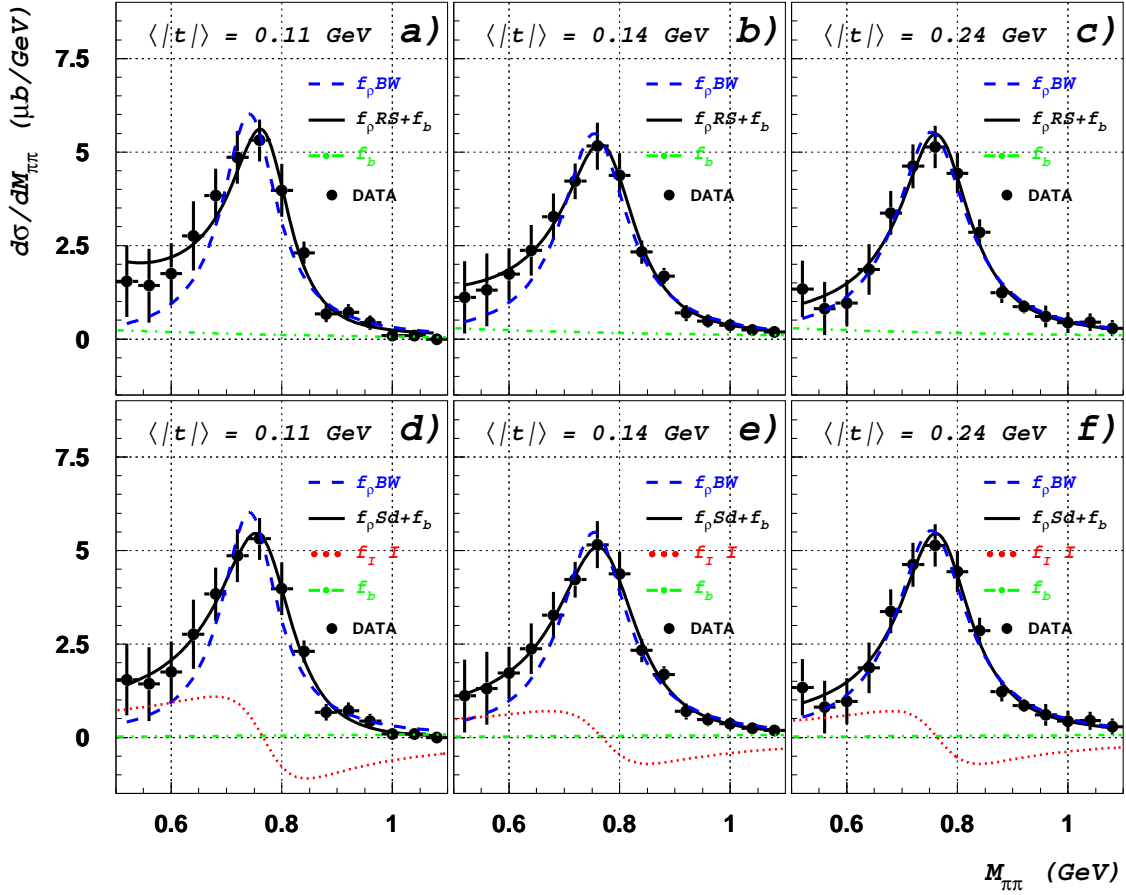


Figure 7.3: The differential cross section $d\sigma/dM_{\pi\pi}$ in three $|t|$ intervals. The filled dots show the measured $d\sigma/dM_{\pi\pi}$ values. The upper plots (a-c) present the Ross-Stodolsky fit (solid line) and relativistic Breit-Wigner fit (dashed line). The lower plots (d-f) present the Söding fit (solid line) and relativistic Breit-Wigner fit (dashed line).

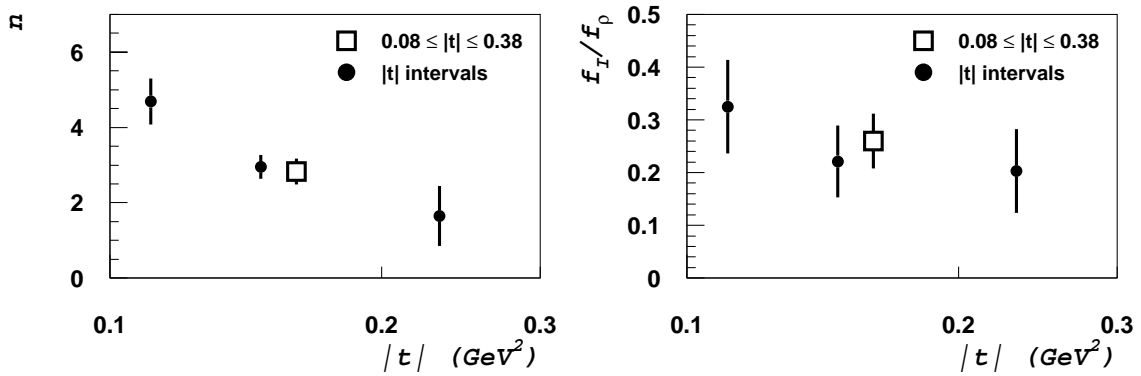


Figure 7.4: The open squares present the skewing parameters in the kinematic range of $0.08 \leq |t| \leq 0.38$ and the filled dots present the skewing parameters in three intervals of the proton momentum transfer $|t|$: a) parameter n of the Ross-Stodolsky parametrization; b) ratio f_I/f_p of the Söding parametrization.

Cross Section $d\sigma/dM_{\pi\pi}$ in W Intervals

The differential cross section $d\sigma/dM_{\pi\pi}$ is calculated in three W intervals which are chosen to get similar statistics in each W interval. In figure 7.5 the data points and fitting profiles are presented. The upper plots of figure 7.5 are fitted by the Ross-Stodolsky and lower plots by the Söding parametrization. The fit results are listed in tables 7.3 and 7.4 for Ross-Stodolsky and Söding parametrizations, respectively.

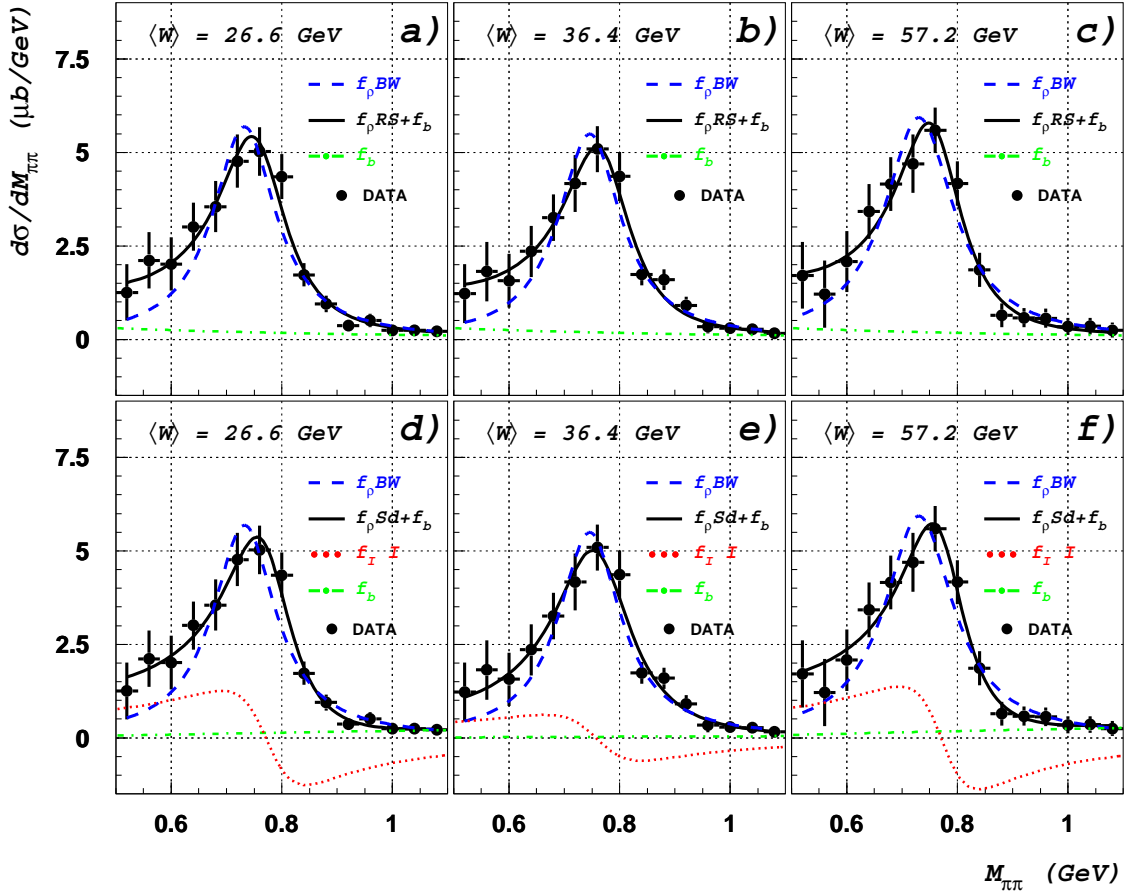


Figure 7.5: The differential cross section $d\sigma/dM_{\pi\pi}$ in three W intervals. The measured $d\sigma/dM_{\pi\pi}$ values are shown by filled dots. The upper plots (a-c) present the Ross-Stodolsky fit (solid line) and relativistic Breit-Wigner fit (dashed line). The lower plots (d-f) present the Söding fit (solid line) and relativistic Breit-Wigner fit (dashed line).

It can be seen in tables 7.3 and 7.4 that there is no skewing dependence on W . Within the errors the skewing factors \mathbf{n} and f_I/f_ρ in the W intervals are constant.

Ross-Stodolsky parametrization					
$\Delta t $ range (GeV ²)	$\langle\Delta t \rangle$ (GeV ²)	M_ρ (GeV)	Γ_ρ (GeV)	\mathbf{n}	χ^2/ndf
$0.08 \leq \Delta t < 0.13$	0.111	773.1 ± 9.9	131.7 ± 13.3	4.69 ± 0.61	8.7 / 8
$0.13 \leq \Delta t < 0.17$	0.147	772.6 ± 5.9	159.2 ± 13.3	2.95 ± 0.32	6.4 / 8
$0.17 \leq \Delta t \leq 0.38$	0.232	764.1 ± 11.4	154.8 ± 14.9	1.65 ± 0.79	7.4 / 8
$0.08 \leq \Delta t \leq 0.38$	0.161	765.6 ± 3.9	147.9 ± 9.7	2.83 ± 0.34	3.8 / 8

Table 7.1: The Ross-Stodolsky parametrization fit parameters for the three $|t|$ intervals.

Söding parametrization					
$\Delta t $ range (GeV ²)	$\langle\Delta t \rangle$ (GeV ²)	M_ρ (GeV)	Γ_ρ (GeV)	\mathbf{f}_I	χ^2/ndf
$0.08 \leq \Delta t < 0.13$	0.111	765.9 ± 17.0	163.7 ± 28.5	0.27 ± 0.12	8.6 / 8
$0.13 \leq \Delta t < 0.17$	0.147	768.2 ± 13.5	176.9 ± 23.7	0.19 ± 0.10	5.1 / 8
$0.17 \leq \Delta t \leq 0.38$	0.232	763.7 ± 15.2	158.3 ± 21.3	0.11 ± 0.09	7.2 / 8
$0.08 \leq \Delta t \leq 0.38$	0.161	769.2 ± 8.7	149.7 ± 13.1	0.64 ± 0.17	3.7 / 8

Table 7.2: The Söding parametrization fit parameters for the three $|t|$ intervals.

Ross-Stodolsky parametrization					
ΔW range (GeV)	$\langle\Delta W\rangle$ (GeV)	M_ρ (GeV)	Γ_ρ (GeV)	\mathbf{n}	χ^2/ndf
$20. \leq \Delta W < 33.$	27.9	760.1 ± 8.9	153.2 ± 14.6	2.98 ± 0.59	4.6 / 8
$33. \leq \Delta W < 46.$	38.7	767.3 ± 9.1	150.8 ± 15.2	3.24 ± 0.71	5.5 / 8
$46. \leq \Delta W \leq 78.$	56.3	761.5 ± 12.6	147.6 ± 18.5	3.46 ± 0.92	8.1 / 8
$20.0 \leq \Delta W \leq 78.0$	41.5	765.6 ± 3.9	147.9 ± 9.7	2.83 ± 0.34	3.8 / 8

Table 7.3: The Ross-Stodolsky parametrization fit parameters for the three W intervals.

Söding parametrization					
ΔW range (GeV)	$\langle\Delta W\rangle$ (GeV)	M_ρ (GeV)	Γ_ρ (GeV)	\mathbf{f}_I	χ^2/ndf
$20. \leq \Delta W < 33.$	27.9	771.0 ± 11.4	151.8 ± 18.3	0.29 ± 0.07	4.3 / 8
$33. \leq \Delta W < 46.$	38.7	757.2 ± 14.0	173.7 ± 24.7	0.16 ± 0.09	7.6 / 8
$46. \leq \Delta W \leq 78.$	56.3	770.5 ± 15.5	145.6 ± 21.8	0.30 ± 0.09	8.8 / 8
$20.0 \leq \Delta W \leq 78.0$	41.5	769.2 ± 8.7	149.7 ± 13.1	0.64 ± 0.17	3.7 / 8

Table 7.4: The Söding parametrization fit parameters for the three W intervals.

7.2 Proton Momentum Transfer Dependence

7.2.1 Uncorrected $|t|$ Spectrum

The proton momentum transfer $|t|$ distributions of the basic and final samples in data and Monte Carlo are presented in figure 7.6. The MC distributions are normalized to the number of events in the data. The solid and dashed lines denote the spectra simulated by PHOJET and DIFFVM, respectively. The filled dots represent the data. The deep and slightly shaded background at the bottom of the plots results from ω -, ϕ -mesons and non-resonant Drell-type $\pi^+\pi^-$ production, respectively. The background contribution is simulated by the PHOJET generator.

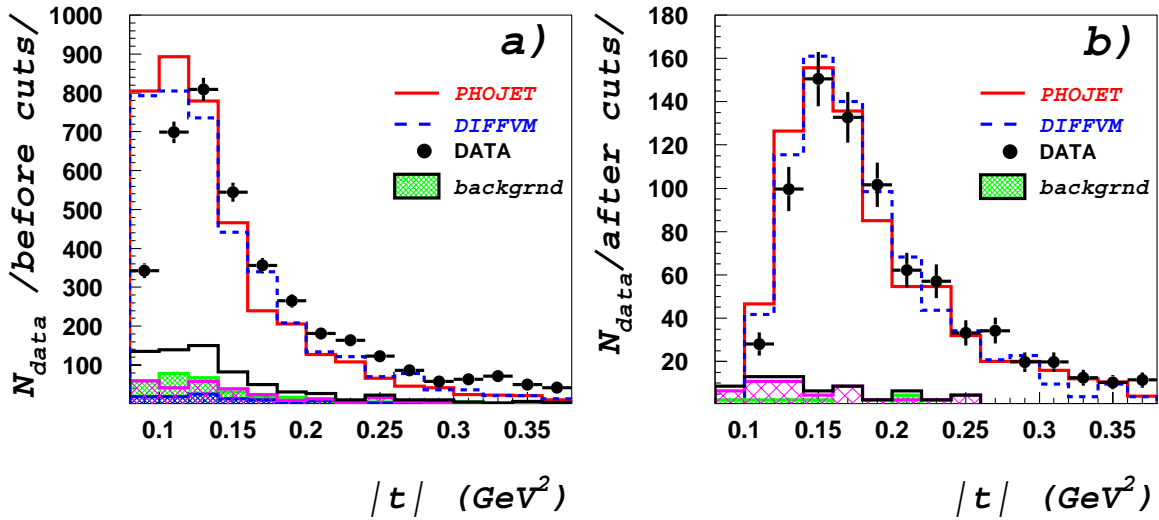


Figure 7.6: The proton momentum transfer distributions uncorrected for the measurement efficiency in **a)** the basic sample, **b)** the final sample. The dots, solid and dashed lines denote the spectra of data, PHOJET and DIFFVM, respectively. The shaded histograms at the bottom of the plots show the background contribution simulated by PHOJET.

7.2.2 Differential Cross Section $d\sigma/d|t|$

The differential cross section $d\sigma/d|t|$ is measured in the momentum transfer region $0.08 < |t| < 0.38 \text{ GeV}^2$ which is limited due to the FPS acceptance and efficiency. The cross section $d\sigma/d|t|$ is calculated for the events within the invariant mass interval (see Sec. 7.1) of $0.5 < M_{\pi\pi} < 1.1 \text{ GeV}$.

According to the Regge formalism and shrinkage discussed in section 2.4 the cross section $d\sigma/d|t|$ can be described by the function:

$$\frac{d\sigma_{\gamma p \rightarrow \rho^0 p}}{d|t|} = A e^{-b|t|} \quad . \quad (7.9)$$

The parameter b in the exponent is termed *logarithmic slope* or b -slope. The b -slope indicates the $|t|$ dependence of the coupling constants used in the Regge approach. At small values of $|t| \simeq p_{t,p}^2 \simeq (p\Theta)^2$ the normalized cross section value is:

$$\frac{d\sigma/d|t|}{(d\sigma/d|t|)_{t=0}} = e^{-b|t|} \simeq 1 - b(p\Theta)^2 \quad . \quad (7.10)$$

The normalized intensity of light with wave number k for optical diffraction from a circular aperture of radius R is:

$$\frac{I}{I_0} \simeq 1 - \frac{R^2}{4}(k\Theta)^2 \quad . \quad (7.11)$$

The comparison of equation 7.10 with 7.11 results with the following relation:

$$b = \frac{R^2}{4} \quad . \quad (7.12)$$

Thus, the b -slope can be understood as the radius of the interactions which is related to the size of the ρ^0 wave packet.

Cross Section $d\sigma/d|t|$ in the FPS acceptance range

The measured $d\sigma/d|t|$ is restricted to the W kinematic region of $20 < W < 78 \text{ GeV}$ due to acceptance and measurement efficiency.

The b -slope is obtained by a fit of the differential cross section in five $|t|$ bins plotted in figure 7.9a. The fitting function of equation 7.9 is used. The b -slope fit result of the elastic ρ^0 photoproduction is:

$$\boxed{b = 10.11 \pm 1.54 \text{ (stat.)} \pm 1.25 \text{ (syst.) GeV}^{-2}} \quad (7.13)$$

The fit parameter A of equation 7.9 in the kinematic region of measured $d\sigma/d|t|$ is:

$$A = 4.5 \pm 0.3 \text{ (stat.)} \pm 0.3 \text{ (syst.) } \mu\text{b/GeV}^2 \quad .$$

The measured cross section $\sigma_{\gamma p \rightarrow \rho^0 p}^{\text{measured}}$ was calculated integrating $d\sigma/d|t|$ over the five $|t|$ bins:

$$\sigma_{\gamma p \rightarrow \rho^0 p}^{\text{measured}} = \sum_{i=1}^5 \frac{d\sigma}{d|t|} \Big|_i \cdot \Delta|t|_i \quad . \quad (7.14)$$

The measured ρ^0 -meson cross section in the kinematic region $0.08 < |t| < 0.38 \text{ GeV}^2$, $0.5 < M_{\pi\pi} < 1.1 \text{ GeV}$ and $20 < W < 78 \text{ GeV}$ is:

$$\boxed{\sigma_{\gamma p \rightarrow \rho^0 p}^{\text{measured}} = 3.76 \pm 0.35 \text{ (stat.)} \pm 0.49 \text{ (syst.) } \mu\text{b}} \quad (7.15)$$

Evaluation of Systematic Errors

The brief overview of the systematic uncertainties of the measured variables is done in section 6.5. In order to estimate the systematic uncertainties of the measured b -slope and elastic ρ^0 photoproduction cross section the analysis was repeated varying the parameters which are involved in the cross section measurement. To estimate the systematic error of the $|t|$ spectrum the transverse momentum of the incoming proton beam was shifted by ± 10 MeV (see Sec. 6.5). The value of 10 MeV was chosen in methodical investigations. These artificially shifted values applied for each event of the data sample constitute the *shifted analysis sample*. The two *shifted analysis samples* with "large acceptance" and "low acceptance" defined in dependence on the FPS positions are analyzed in addition to the samples of shifted transverse momenta.

The errors of the b -slope and integrated cross section differences obtained in the *shifted analysis samples* were summed in quadrature. These values are presented as the systematic errors of expressions 7.13 and 7.16.

Cross section $d\sigma/d|t|$ in W intervals

The cross section $d\sigma/d|t|$ is measured in three intervals of W . The W intervals are chosen to have nearly the same event statistics in each interval (see Sec. 7.1.3). The measured differential cross sections $d\sigma/d|t|$ for three W intervals are presented in figure 7.7. The b -slope of equation 7.9 is expected to increase logarithmically with the interaction energy (see Sec. 2.4). The fit results of figure 7.7 are listed in table 7.6.

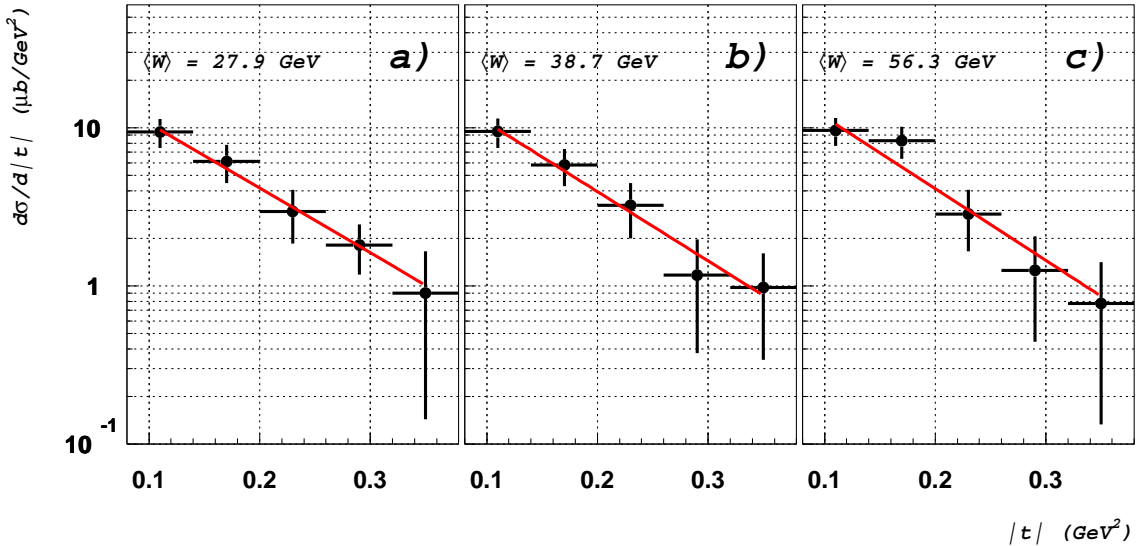


Figure 7.7: The differential cross section $d\sigma_{\gamma p \rightarrow \rho p}/d|t|$ measured in three W intervals. The ranges of the W intervals together with fit results of the b -slope are listed in table 7.6.

Cross section $d\sigma/d|t|$ in $M_{\pi\pi}$ intervals

The b -slope depends on the range of the ρ^0 -meson decay pion invariant mass $M_{\pi\pi}$. The cross section $d\sigma/d|t|$ considered in three intervals of $M_{\pi\pi}$ is shown in figure 7.8. The b -slope decreases with increasing $M_{\pi\pi}$. This effect can be explained [87] by the contribution of non-resonant $\pi^+\pi^-$ background as discussed in section 5.3. The b -slope in dependence on $M_{\pi\pi}$ is shown in figure 7.9d.

Parameter	Invariant Mass Intervals			Units
$\Delta M_{\pi\pi}$ range	$0.5 < M_{\pi\pi} < 0.735$	$0.735 < M_{\pi\pi} < 0.8$	$0.8 < M_{\pi\pi} < 1.1$	GeV
$\langle \Delta M_{\pi\pi} \rangle$	0.679	0.767	0.880	GeV
b	10.95 ± 2.15 (stat)	10.06 ± 2.02 (stat)	9.28 ± 2.39 (stat)	GeV ⁻²

Table 7.5: The b -slope in three $M_{\pi\pi}$ intervals. The corresponding differential cross section $d\sigma/d|t|$ in $M_{\pi\pi}$ intervals are shown in figure 7.8. The b -slope values presented here for mass intervals are shown in figure 7.9d.

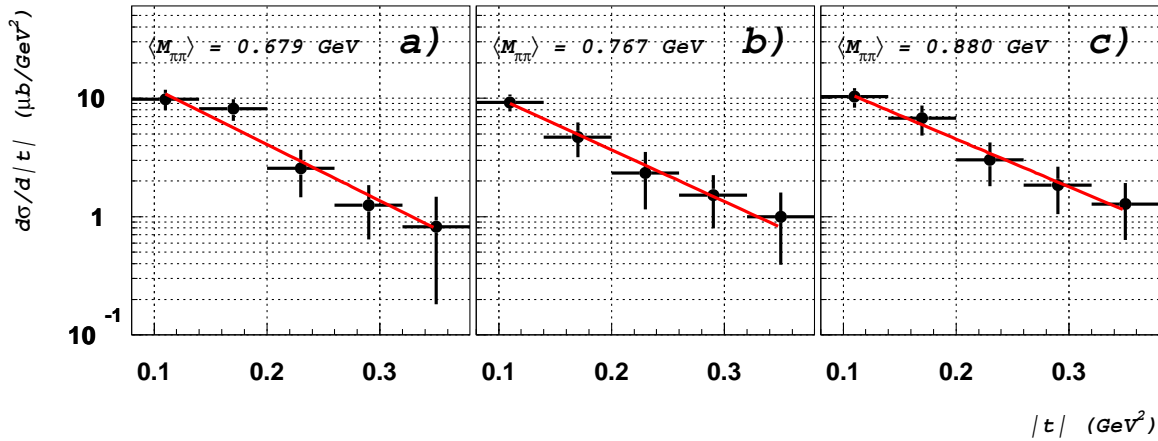


Figure 7.8: The differential cross section $d\sigma_{\gamma p \rightarrow \rho^0 p}/d|t|$ for three intervals of the ρ -meson decay pions invariant mass $M_{\pi\pi}$.

Extrapolation to the Full Kinematic Region

The integrated value of the measured cross section σ_{mea} is extrapolated to the full kinematic region. The fit parameters of the Söding parametrization are used to integrate the $d\sigma/dM_{\pi\pi}$ function and extrapolate the selected mass region to the full mass region. The extrapolation of $d\sigma/d|t|$ is performed by the actual b -slope value of the $d\sigma/d|t|$ distribution. For the spectrum of figure 7.9a the measured b -slope is given in expression 7.13. The extrapolation constants for the $M_{\pi\pi}$ and $|t|$ regions are: $\mathcal{C}_{M_{\pi\pi}} = 0.897$ and $\mathcal{C}_{|t|} = 0.424$. The extrapolated value of the $\gamma p \rightarrow \rho^0 p$ cross section in range of $20 < W < 78$ GeV is:

$$\sigma_{\gamma p \rightarrow \rho^0 p} = 9.88 \pm 0.93 \text{ (stat.)} \pm 1.30 \text{ (syst.) } \mu b \quad (7.16)$$

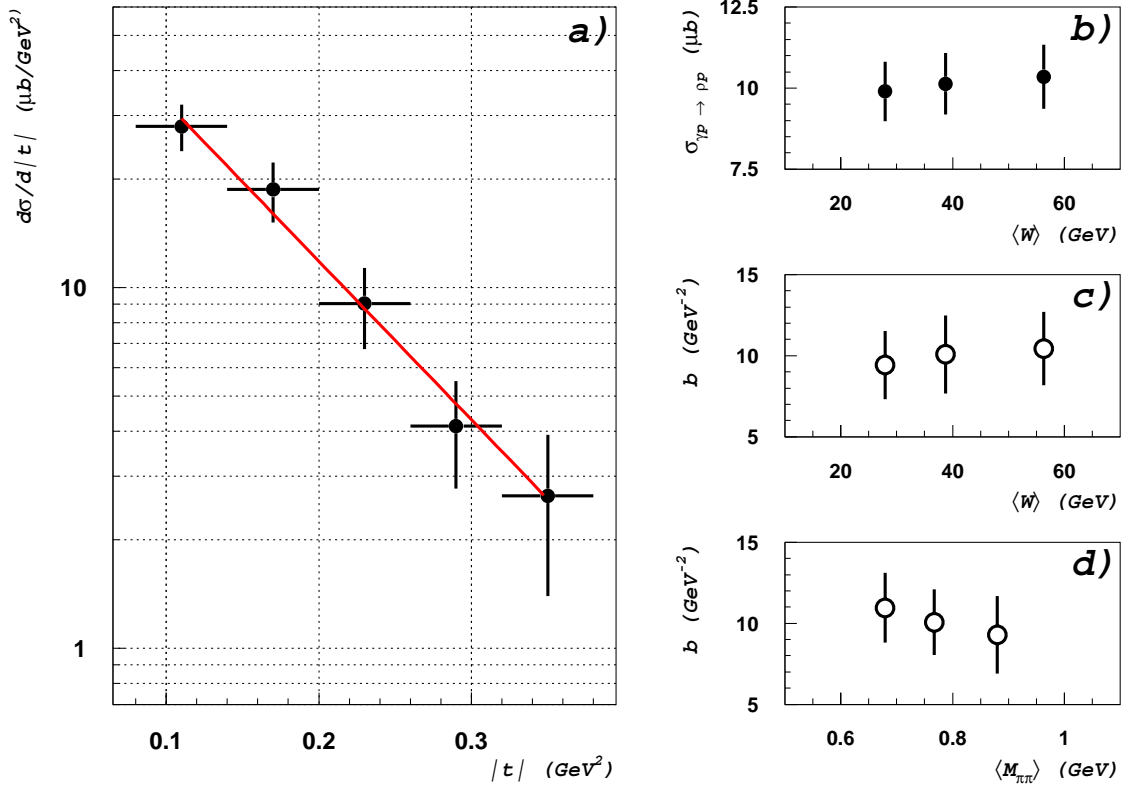


Figure 7.9: **a)** The differential cross section $d\sigma_{\gamma p \rightarrow \rho^0 p}/d|t|$ measured in the kinematic region $0.08 < |t| < 0.38 \text{ GeV}^2$, $0.5 < M_{\pi\pi} < 1.1 \text{ GeV}$ and $20 < W < 78 \text{ GeV}$. **b)** The integrated $\gamma p \rightarrow \rho^0 p$ cross section values calculated in three W intervals and extrapolated to the full kinematic region. **c)** The b -slope in W intervals. The predicted W dependence from the b -slope is logarithmic. **d)** The b -slope in $M_{\pi\pi}$ intervals. A decrease in b -slope while increasing $M_{\pi\pi}$ indicates the contribution of the interference term from the non-resonant $\pi^+\pi^-$ production.

W interval [GeV]	$\langle W \rangle$ [GeV]	$\mathcal{F}_{\gamma/e}$ —	\mathbf{b} [GeV $^{-2}$]	$\sigma_{\gamma p \rightarrow \rho^0 p}$ [μb]
$20 \leq W < 33$	27.9	0.05135	9.43 ± 2.11	9.90 ± 0.92
$33 \leq W < 46$	38.7	0.04072	10.08 ± 2.40	10.13 ± 0.95
$46 \leq W \leq 78$	56.3	0.04659	10.44 ± 2.27	10.35 ± 0.99
$20 \leq W \leq 78$	41.5	0.13866	10.11 ± 1.54	9.88 ± 0.93

Table 7.6: The measured cross section and b -slope values in three intervals of W are extrapolated to the full kinematic region of $M_{\pi\pi}$ and $|t|$. The extrapolation constants $\mathcal{C}_{M_{\pi\pi}} = 0.897$ and $\mathcal{C}_{|t|} = 0.424$ are applied for the kinematic region of $M_{\pi\pi}$ and $|t|$, respectively.

7.3 Evaluation of Statistical Errors

The statistical errors of the measured cross section are estimated taking into account the number of collected events, the measurement efficiency of the FPS and trigger and reconstruction efficiencies of the Central Tracker. The number of collected ρ -meson events in consideration with resonant and non-resonant background estimated by PHOJET is 943 events. The background estimation is described in section 5.3. The efficiency measurement is discussed in section 6.4. The statistical errors of the collected ρ -meson events and measurement efficiency are presented in table 7.7.

	Source of the statistical error	Value (in %)
δ_1	Number of collected events	3.2%
δ_2	$DCR\phi$ trigger efficiency $\varepsilon_{DCR\phi}^{trig}$	3.1%
δ_3	z -vertex trigger efficiency $\varepsilon_{zvtx}^{trig}$	3.0%
δ_4	Reconstruction efficiency $\varepsilon_{\rho CJC}^{rec}$	0.005%
δ_5	Reconstruction efficiency ε_{zvtx}^{rec}	0.003%
δ_6	FPS efficiency ε_{FPS}	7.6%
δ_Σ	Full statistical error of measured cross section	9.3%

Table 7.7: The sources of the statistical errors with corresponding values which are used during the estimation of the measured cross section.

The contribution of $DCR\phi$ and z -vertex trigger efficiencies are calculated using data sample 2. The sample 2 discussed in section 5.1 contains 30717 events. The reconstruction efficiencies $\varepsilon_{\rho CJC}^{rec}$ and ε_{zvtx}^{rec} are calculated using all simulated events without the FPS selection criteria application as discussed on page 85.

The largest contribution to the statistical error of the measured cross section is the full statistical error of the FPS efficiency $\delta_6(\varepsilon_{FPS})$. This value includes the single layer efficiency, reconstruction efficiency of the track and FPS acceptance (see Fig. 6.12 – 6.14).

The full statistical error δ_Σ in table 7.7 is used for the estimation of the statistical error in expression 7.15. This value is calculated as quadratic sum of the statistical errors δ_1 – δ_6 :

$$\delta_\Sigma^2 = \sum_{k=1}^6 \delta_k^2$$

The statistical error in expression 7.16 is extrapolated from the value of the statistical error in expression 7.15 by the extrapolation procedure described on page 99.

7.4 Comparison with Other Measurements

The total cross section $\sigma_{\gamma p \rightarrow \rho^0 p}$ and b -slope of the current analysis are fitted by the following functions of W :

$$\sigma_{\gamma p \rightarrow \rho^0 p}(W) = \eta W^{4\epsilon} \quad ; \quad b_\rho = b_0 + 2\alpha' \cdot \ln(W^2) \quad (7.17)$$

where $\epsilon = \alpha_P - 1$ – is the parameter of the Donnachie-Landshoff approach [88, 89] and α' the slope of the pomeron trajectory (see expression 2.29). The fit results of the expressions 7.17 in the current analysis are:

$$\boxed{\epsilon = 0.03 \pm 0.07} \quad , \quad \boxed{\alpha' = 0.36 \pm 0.58} \quad . \quad (7.18)$$

The fitting profiles are presented in figure 7.10.

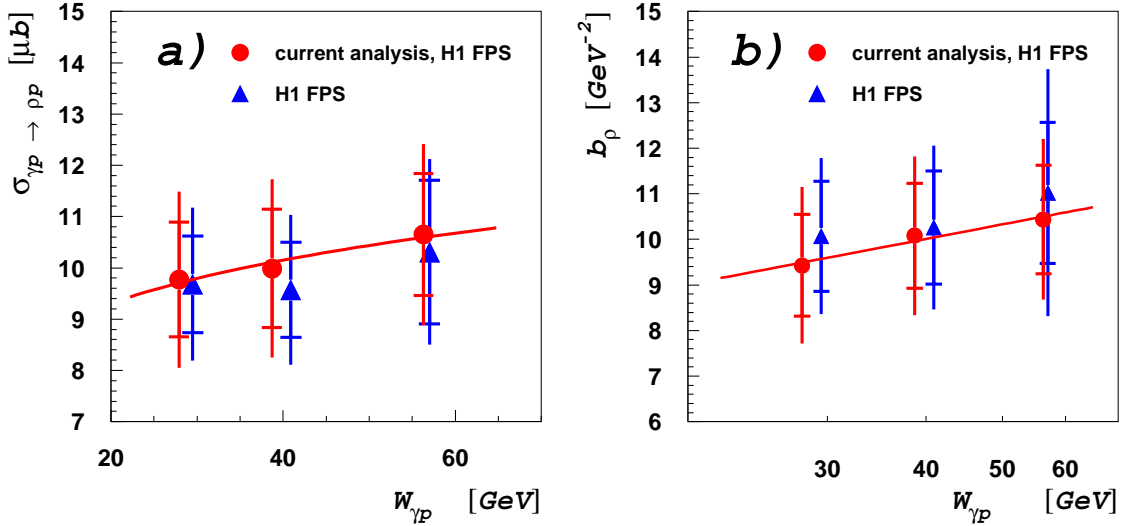


Figure 7.10: **a)** The total cross section of elastic ρ^0 -meson photoproduction measured in three W intervals. **b)** The b -slope of equation 7.9 in W intervals. The filled dots present results of the current analysis and filled rectangles present results of the analysis of Dr.O.Karschnik [81]. The inner bars denote the statistical errors and the outer bars contain statistical and systematic errors added in quadrature.

The current analysis results are compared with previous measurements [93, 94]. The total $\gamma p \rightarrow \rho^0 p$ cross sections measured in fixed target experiments [90, 91, 92], ZEUS [75] and H1 [95] are presented in figure 7.12. The cross section values of three W intervals measured in this work are shown by filled dots. The distribution of all measured $\gamma p \rightarrow \rho^0 p$ cross section values is fitted by the Donnachie-Landshoff (DL) [88] parametrization:

$$\sigma_{el} = X s^\epsilon + Y s^{-\delta} \quad (7.19)$$

Here s is the centre of mass energy of $e p$ interaction. The parameters ϵ and δ are the effective powers in the sum of multiple Pomeron and Reggeon exchanges. The parameters ϵ and δ are related to the Pomeron and Reggeon trajectories (see expressions 2.32).

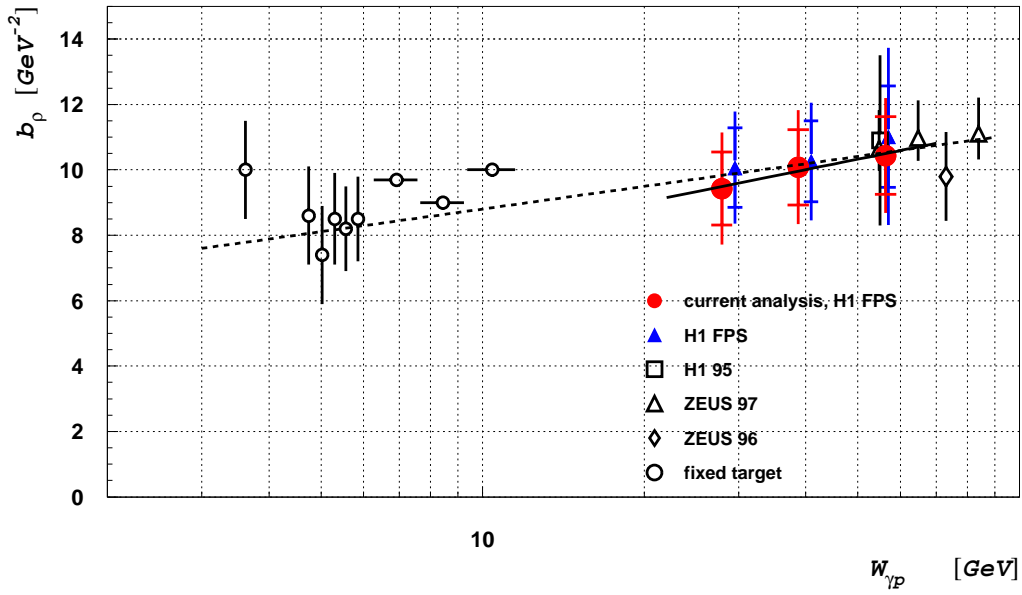


Figure 7.11: The b -slope of equation 7.9 in dependence on W . The solid line presents the fit of expression 7.17 for three W intervals of current analysis at $\alpha' = 0.36 \pm 0.58$. The dashed line presents the fit of all points at $\alpha' = 0.25$.

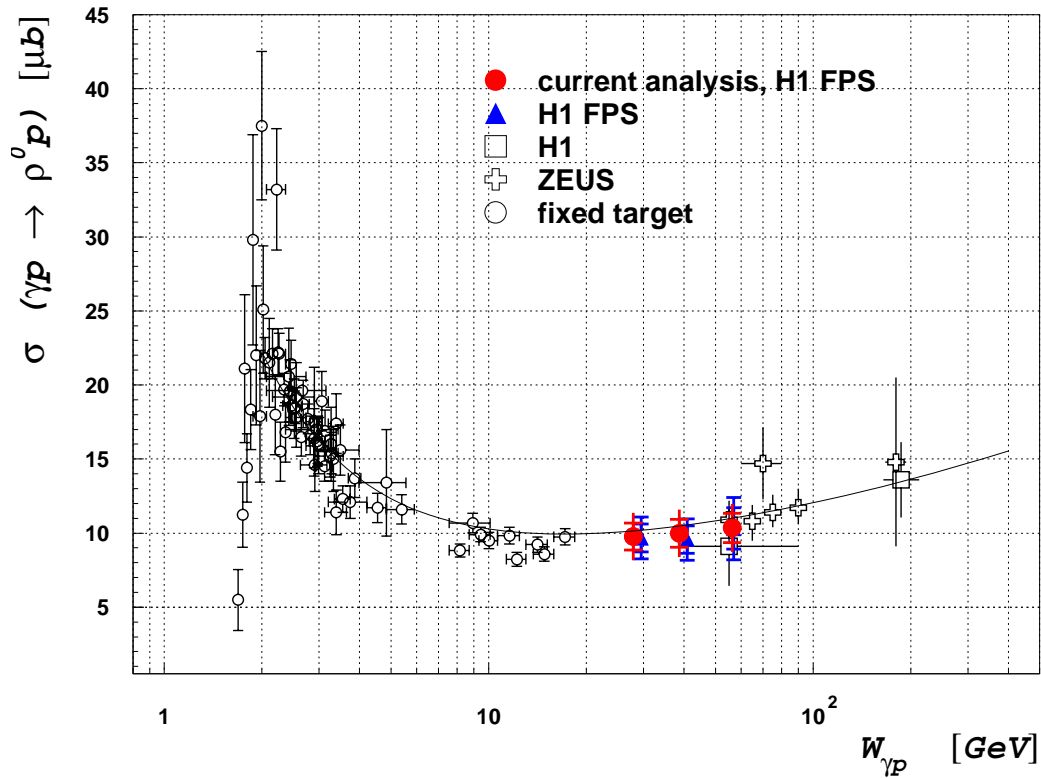


Figure 7.12: The integrated $\gamma p \rightarrow \rho^0 p$ cross section in dependence on W . The solid line presents the fit of the Donnachie-Landshoff approach.

A.Donnachie and P.V.Landshoff attempted a global fit to the total γp cross sections by the sum of Reggeon (\mathcal{R}) and Pomeron (\mathcal{P}) trajectories exchange. According to the optical theorem (see page 7) the elastic cross section σ_{el} is also fitted by the sum of \mathcal{R} and \mathcal{P} in the DL approach. The fit of the DL formula 7.19 results in the following values:

$$\begin{aligned}\epsilon &= \alpha_{\mathcal{P}}(0) - 1 = 0.0808 \\ \delta &= 1 - \alpha_{\mathcal{R}}(0) = 0.4525\end{aligned}\tag{7.20}$$

The current results are compared with the parallel analysis of Dr.O.Karschnik [81]. The measurements of the $\gamma p \rightarrow \rho^0 p$ cross section and b -slope for the current and Karschnik's analyses are presented in figure 7.10. The results are in a good agreement with each other.

The comparison to previous measurements is presented in figures 7.11 and 7.12.

Chapter 8

Conclusions

This thesis presents the ρ^0 -meson photoproduction cross section measured in the kinematic region of $0.5 < M_{\pi\pi} < 1.1$ GeV, $0.08 < |t| < 0.38$ GeV² and $20 \leq W < 78$ GeV. The data collected during January – April 1999 e^-p colliding period of HERA are used. For this period the Forward Proton Spectrometer (FPS) horizontal stations at H1, involved into operation, have been used for the first time in analyses of photoproduction and deep inelastic processes. The results presented in this thesis have been compared with results of the parallel work of Dr.O.Karschnik [81]. The measured cross section, extrapolated to the full kinematic region, has been compared with previous measurements.

The distribution of the differential cross section $d\sigma/dM_{\pi\pi}$ is calculated using events with ρ^0 -meson decay pion tracks measured in the central region of the H1 detector (see chapter 3). The distribution of the differential cross section $d\sigma/dt$ is calculated using the direct measurement of the proton momentum transfer in the FPS horizontal stations (see chapter 4).

The elastic cross section of $\gamma p \rightarrow \rho^0 p$ process is measured in the current analysis in three intervals of the γp centre of mass energy W . The mean value of the γp centre of mass energy $\langle W \rangle = 41.5$ GeV results in the current work with $\gamma p \rightarrow \rho^0 p$ cross section of $\sigma_{\gamma p \rightarrow \rho^0 p} = 9.88 \pm 0.93$ (*stat.*) ± 1.30 (*syst.*) μb which is consistent with other results. The measured logarithmic slope value of the differential cross section $d\sigma/dt$ is in agreement with shrinkage phenomena which was found in experiments at lower energies and checked at HERA energies by previous measurements of the H1 and ZEUS experiments. The value $b = 10.11 \pm 1.54$ (*stat.*) ± 1.25 (*syst.*) GeV⁻² was obtained in the fit of $d\sigma/d|t|$ in the whole W range.

A slow rise of the elastic ρ^0 cross section with increasing W is consistent with the Donnachie-Landshoff approach (DL) [88, 89]. A.Donnachie and P.V.Landshoff introduce a sum of Reggeon and Pomeron trajectories exchange. As one can see from formula 7.19 at high energies only the Pomeron term remains.

The γp interactions were modeled in the current work by single and multiple Pomeron exchanges. The single Pomeron exchange is realized by the DIFFVM generator and the multiple Pomeron exchange by the PHOJET generator.

The measured cross section is in agreement with the theoretical models inside the measurement errors. The statistics of the measurement presented in this work is significantly rejected by the acceptance of the FPS horizontal stations and remains small, till an analysis of the next to 1999 colliding period will be performed.

Bibliography

- [1] L.Stodolsky, Phys. Rev. Lett. **18** (1967) 135.
- [2] H.Joos, Phys. Lett. **B24** (1967) 103.
- [3] K.Kajantie and J.S.Trefl, Phys. Lett. **B24** (1967) 106.
- [4] P.D.B. Collins, A.D.Martin, *Hadron Interactions*, Adam Hilger,(1984)
- [5] ZEUS Collaboration, M.Derrick et al., Z. Phys. **C69** (1995) 39.
- [6] ZEUS Collaboration, M.Derrick et al., Phys. Lett. **B350** (1995) 120.
- [7] ZEUS Collaboration, M.Derrick et al., Phys. Lett. **B356** (1995) 601.
- [8] H1 Collaboration, S.Aid et al., Nucl. Phys. **B463** (1996) 3.
- [9] H1 Collaboration, S.Aid et al., Nucl. Phys. **B468** (1996) 3.
- [10] H1 Collaboration, S.Aid et al., Nucl. Phys. **B472** (1996) 3.
- [11] J.J.Sakurai, Ann. Phys., **11** (1960) 1.
- [12] J.J.Sakurai, Phys. Rev. Lett, **22** (1969) 981.
- [13] L.D. Landau and E.M. Lifshitz, *Volume 4 of Course of Theoretical Physics*, Pergamon Press, (1958).
- [14] T.Regge, Nuovo Cimento **14** (1959) 951.
- [15] T.Regge, Nuovo Cimento **18** (1960) 947.
- [16] P.D.B. Collins, *Introduction to Regge Theory and High Energy Physics*, Cambridge University Press, (1997).
- [17] I.Ya.Pomeranchuk and I.M.Shmushkevich, Nucl. Phys. **23** (1961) 1295.
- [18] K. Schilling et al., Nucl. Phys. **B15** (1970) 397.
- [19] K. Schilling and G. Wolf, Nucl. Phys. **B61** (1973) 381.

- [20] F.Jacquet, A.Blondel, in Proceedings of the study of an *ep* facility for Europe, Hamburg (1979) 391.
- [21] E.Fermi, F. Phys., **29** (1924) 315.
- [22] E.J.Williams, Phys. Rev. **45** (1934) 729.
- [23] C.F.Weizsäcker, Z. Phys. **88** (1934) 612.
- [24] G.Nordheim et al., Phys. Rev. **51** (1937) 1037.
- [25] R.B.Curtis, Phys. Rev. **104** (1956) 211.
- [26] R.H Dalitz and D.R.Yennie, Phys. Rev. **105** (1957) 1598.
- [27] I.Ya.Pomeranchuk, Sov. Phys. JETP **7** (1958) 499.
- [28] V.N.Gribov, Sov. Phys. JETP **14** (1962) 478.
- [29] V.M.Budnev, I.F.Ginzburg, G.V.Meledin and V.G.Serbo, Phys. Rep. **C15** (1975) 181.
- [30] I.F.Ginzburg and V.G.Serbo, Phys. Lett. **B109** (1982) 231.
- [31] B.L.Ioffe, V.A.Khoze and L.N.Lipatov, *Hard Processes, Volume 1: Phenomenology Quark-Parton Model* (North-Holland Physics Publishing, Amsterdam, 1984)
- [32] M.Gell-Mann and F.Zachariasen, Phys. Rev. **124** (1961) 953.
- [33] N.M.Kroll, T.D. Lee and B.Zumino, Phys. Rev. **157** (1967) 1376.
- [34] T.H.Bauer, Nucl. Phys. **B57** (1973) 109.
- [35] P.Söding, Phys. Lett. **19** (1966) 702.
- [36] J.Pumplin and L.Stodolsky, Phys. Rev. Lett. **25** (1970) 970.
- [37] A.C.Irving, R.P.Worden, Phys. Rep. **C34** (1977) 118.
- [38] R.Blankenbecler and M.L.Goldberger, Phys. Rev. **126** (1962) 766.
- [39] V.N.Gribov et al., Zh. Eksp. Teor. Fiz. **41** (1961) 1834.
- [40] G.F.Chew, S.C.Frautschi, Phys. Rev. Lett. **7** (1961) 394.
- [41] G.F.Chew, S.C.Frautschi, Phys. Rev. Lett. **8** (1962) 41.
- [42] A.B.Kaidalov, V.A.Khoze, Yu.F.Pirogov and N.L.Ter-Isaakyan, Phys. Lett. **B45** (1973) 493.
- [43] K.A.Ter-Martirosyan, Sov. Phys. JETP **17** (1963) 233. K.A.Ter-Martirosyan, Nucl. Phys. **68** (1964) 591.

- [44] I.A.Verdiev et al., Sov. Phys. JETP **19** (1964) 1148.
- [45] V.N.Gribov, Sov. Phys. JETP **26** (1968) 414.
- [46] V.N.Gribov and A.A.Migdal, Sov. J. Nucl. Phys. **8** (1969) 583.
- [47] M.Froissart, Phys. Rev. **123** (1961) 1053.
- [48] A.Martin, Phys. Rev. **129** (1963) 1462.
- [49] N.N.Bogoliubov, D.V.Shirkov, *Quantum Fields*, The Benjamin/Cummings Publ. Co. Inc., (1985) originally published:
N.N.Bogoliubov, D.V.Shirkov, *Introduction to the theory of quantized fields*, Moscow, Nauka, (1973, in Russian)
- [50] V.A.Petrov, Nucl. Phys. Proc. Suppl. **A54** (1997) 160. V.A.Petrov and A.V.Prokudin, in Proceedings of the International Conference on Elastic and Diffractive Scattering, Protvino, Russia (1999) 95.
- [51] S.M.Troshin and N.E.Tyurin, hep-ph/0109047
- [52] A.B.Kaidalov, Phys. Rep. **50** (1979) 157.
- [53] M.S.Dubovikov and K.A.Ter-Martirosyan, Preprint ITEP-37, Moscow (1976)
B.Z.Kopeliovich and L.I.Lapidus, Preprint JINR, E2-9537, Dubna (1976)
M.S.Dubovikov, L.I.Lapidus, B.Z.Kopeliovich and K.A.Ter-Martirosyan, Nucl. Phys. **B123** (1977) 147.
- [54] M.S.Dubovikov and K.A.Ter-Martirosyan, Nucl. Phys.**124** (1977) 163.
- [55] E.M.Levin and M.G.Ryskin, Yad. Fiz. **25** (1977) 849.
- [56] S.Mandelstam, Nuovo Cimento **30** (1963) 1127.
- [57] V.A.Abramovskii, V.N.Gribov and O.V.Kancheli, Sov. J. Nucl. Phys. **18** (1974) 308.
- [58] G.Schuler and T.Sjöstrand, Nucl. Phys. **B 407** (1993) 539.
- [59] J.D.Jackson, Nuovo Cimento **34** (1964) 1644.
- [60] R.A.Morrow, Nuovo Cimento **61A** (1969) 215.
- [61] B.List and A.Mastroberardino, *DIFFVM – A Monte Carlo Generator for Diffractive Processes in ep Scattering* (1998)
- [62] R.Engel, *PHOJET manual* University Siegen preprint 95-05 (1995)
R. Engel and J. Ranft, Phys. Rev. D **54** (1996) 4244
- [63] A.Capella, U.Sukhatme, C.I.Tan and J.Trân Thanh Vân, Phys. Rep. **236** (1994) 227.

- [64] R.Engel, Ph.D. Thesis, Siegen, Universität-Gesamthochschule-Siegen, 1997.
- [65] V.N.Gribov, *Yad. Fiz.* **17** (1973) 603.
- [66] I.Ya.Azimov, E.M.Levin, M.G.Ryskin and V.A.Khoze, *Nucl. Phys.* **B89** (1975) 508.
- [67] B.H.Wiik, in *Proceedings of the Workshop Physics at HERA, Hamburg, Germany* (1991) 1.
- [68] I.Abt et al., *Nucl. Instr. and Meth.* **A386** (1997) 310. I.Abt et al., *Nucl. Instr. and Meth.* **A386** (1997) 348.
- [69] ZEUS Collaboration, M.Derrick et al., *DESY 1993* (1993)
- [70] HERMES Collaboration, K.Coulter et al., *DESY-PRC 90/01* (1990)
- [71] HERA-B Collaboration, T.Lohse et al., *DESY-PRC 94/02* (1994)
- [72] B.H.Wiik, *Proc. of the XXIV Int. Conf. on High Energy Physics, Berlin* (1989) 404.
- [73] H.Bethe and W.Heitler, *Proc. Roy. Soc.* **A146** (1934) 83.
- [74] P.van Esch et al., *Nucl. Inst. and Meth.* **A446** (2000) 409.
- [75] ZEUS Collaboration, M.Derrick et al., *Z. Phys.* **C73** (1997) 253.
- [76] H1 Collaboration, C. Adloff et al., *Eur. Phys. J.* **C6** (1999) 587.
- [77] H1 Collaboration, C. Adloff et al., *Nucl. Phys.* **B619** (2001) 3.
- [78] Appl. software group, GEANT, CERN programm library, GERN, Geneva
- [79] B.List, Ph.D. Thesis, Hamburg, Hamburg-University, 1997, *DESY F11/F12-97-03*.
- [80] H.Wollnik *Optics of Charged Particles*, Academic Press, 1987
- [81] O.Karschnik, Ph.D. Thesis, Hamburg, Hamburg-University, 2001, *DESY-THESIS-2001-026*.
- [82] ZEUS Collaboration, M.Derrick et al., *Z. Phys.* **C73** (1996) 73.
- [83] ZEUS Collaboration, M.Derrick et al., *Phys. Lett.* **B377** (1996) 259.
- [84] S.D.Drell, *Phys. Rev. Lett.* **5** (1960) 278.
- [85] S.D.Drell, *Rev. Mod. Phys.* **33** (1961) 458.
- [86] M.Ross and L.Stodolsky, *Phys. Rev.* **149** (1966) 1172.
- [87] ZEUS Collaboration, J.Breitweg, et al., *DESY 97-237, hep-ex/9712020* (1997)

- [88] A. Donnachie, P.V. Landshoff, Phys. Lett. **B296** (1992) 227.
- [89] A. Donnachie, P.V. Landshoff, Phys. Lett. **B348** (1995) 213.
- [90] EMC collaboration, J.Ashman et al., Z. Phys. **C39** (1988) 169.
- [91] M.Arneodo et al., Nucl. Phys. **B429** (1994) 503.
- [92] M.R.Adams et al., Z. Phys. **C74** (1997) 237.
- [93] T.H.Bauer et al., Rev. Mod. Phys. **50** (1978) 261.
- [94] K.Goulianos, Phys. Rep. **C101** (1983) 169.
- [95] H1 Collaboration, *Measurement of Semi-Inclusive Diffractive Deep-Inelastic Scattering with a Leading Proton at HERA*, H1 collaboration, Contribution to the International Europhysics Conference on High-Energy Physics EPS-2001, Budapest, Hungary, July 2001.

Acknowledgments

First of all I would like to thank director of LPP JINR Dr. V.D.Kekelidze who supported my visit to IfH DESY-Zeuthen and former director of IfH DESY-Zeuthen Prof. Dr. P.Söding for the giving opportunity to work in IfH DESY-Zeuthen. I thank my referees Prof. Dr. P.Söding and Prof. Dr. H.Kolanoski for useful advices concerning this thesis.

My deep gratefulness I express to the leader of H1-Zeuthen group and chosen spokesman of H1 experiment Dr. M.Klein for his invaluable help and support to this work.

I am very grateful to the former leader of FPS group Prof. Dr. W.Bartel and Dr. O.Karschnik for many useful discussions concerning analysis and physics detail. Prof. Dr. W.Bartel and Dr. O.Karschnik helped me with many crucial questions of the current work.

I express my very deep thanks to Dr. M.N.Kapishin. During my stay in IfH DESY-Zeuthen and especially in the beginning of my work Dr. M.N.Kapishin has provided very important assistance in almost all analysis questions. I wish to thank my colleagues from JINR department A.N.Koutov, V.N.Spaskov and especially the leader of my JINR group Dr. Yu.K.Potrebeynikov. I am glad to be a member of this JINR group.

I liked very much to work in IfH DESY-Zeuthen with Dr. A.S.Somov, Dr. R.Shanidze and I.P.Tsurin. Separately i would like to acknowledge Dr. V.V.Arkadov who has introduced me to IfH DESY-Zeuthen.

I would like to acknowledge Prof. Dr. O.V.Tarasov, Dr. M.Yu.Kalmykov, Dr. A.Tkabaladze and Dr. O.L.Veretin who worked in theory group of IfH DESY-Zeuthen and help me in many theory questions.

I am grateful to Dr. A.Buniatian for his interest to my work and useful remarks concerning the details of H1 detector, H1 software and HERA physics.

In conclusion i wish to express my deepest love and gratefulness to my wife Svetlana and to my sister Karine. Their support and faith made the most large contribution in this work.

Lebenslauf

Angaben zur Person

Name: Anatoli Astvatsatourov
Geburt: 16.01.1970 in Yerevan (UdSSR)
Nationalität: Russisch
Familienstand: Verheiratet
Ehegattin: Svetlana Balk
Name des Vaters: Raffi G. Astvatsatourov
Name der Mutter: Elfrida W. Astvatsatourova, geb. Dokhikian

Ausbildungsweg

Sep 1987 - Jul 1993 Studium an der Physikalische Fakultät von Yerevaner Staatsuniversität in der Fachrichtung Experimentelle Physik.
Oct 1992 - May 1993 Pre-diplom und Diplom Thesis im Vereinten Institut für Kernphysik, Dubna, Russland.
Jul 1993 Staatsexamen und Diplom an der Universität
Dec 1993 Wissenschaftlicher Mitarbeiter an der Vereinten Institut für Kernphysik, Dubna, Russland.
Feb 1998 Beginn der Dissertation bei Prof. Dr. H. Kolanoski an der Humboldt-Universität zu Berlin unter Betreuung von Dr. M. Klein, DESY-Zeuthen.

Publikationsliste

1. *The H1 Forward Proton Spectrometer at HERA.*
P. Van Esch et al., Nucl. Instr. and Meth. **A446** (2000) 409.
2. *Spectrometric characteristics of polystyrene scintillation films.*
A.R. Astvatsaturov, et al., Nucl. Instr. and Meth. **A425** (1999) 516.
3. *Results from a Combined Test of an Electromagnetic Liquid Argon Calorimeter with a Hadronic Scintillating Tile Calorimeter.*
ATLAS Collaboration, Nucl. Instr. and Meth. **A387** (1997) 333.
4. *Response of the ATLAS Tile Calorimeter Prototype to Muons.*
Z. Ajaltouni, et al. Nucl. Instr. and Meth. **A388** (1997) 64.
5. *Separation of Gluon Jets and B-Jets with a Low $p(t)$ Muon using ATLAS Tile Calorimeter. Simulation Data and Artificial Neural Networks Technique.*
A. Astvatsaturov et al., Nucl. Instr. and Meth. **A389** (1997) 199.
6. *A Measurement of the Energy Loss Spectrum of 150-GeV Muons in Iron.*
RD34 Collaboration, E. Berger et al., Z.Phys. **C73** (1997) 455.
7. *Identification of B-Jets with a Low $P(T)$ Muon using ATLAS Tile Calorimeter Simulation Data and Artificial Neural Networks Technique.*
A. Astvatsaturov et al., Preprint JINR, JINR-E10-96-288, Dubna, (1996)
8. *Improvement in Separation of Isolated Muons and Pions at Low $p(t)$ in ATLAS Hadron Calorimeter using Artificial Neural Networks Technique.*
A. Astvatsaturov et al., Preprint JINR, JINR-E10-95-476, Dubna, (1995)
9. *ATLAS Calorimeters Energy Calibration for Jets.*
A.R. Astvatsaturov et al., Preprint JINR, JINR-E13-94-522, Dubna, (1994)

Selbständigkeitserklärung

Hiermit erkläre ich, die vorliegende Arbeit selbständig ohne fremde Hilfe verfasst zu haben und nur die angegebene Literatur und Hilfsmittel verwendet zu haben.

Anatoli Astvatsatourov
22.11.01